Charles University in Prague
Faculty of Mathematics and Physics

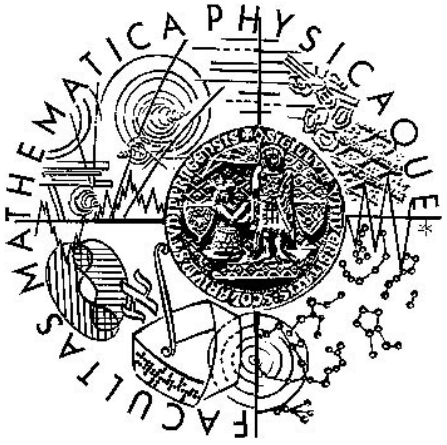

Diploma Thesis

The Character of Excess of Cosmic Rays above the GZK Cutoff

Michael Prouza

Supervisor of the Thesis RNDr. Jiří Grygar, CSc.

Study Program: Physics — Specialization: Astronomy & Astrophysics

Prague — April 2001

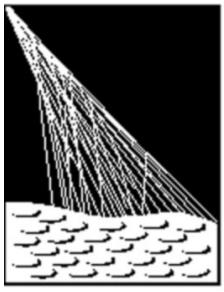

PIERRE
AUGER
OBSERVATORY

I declare that I have worked out this diploma thesis myself using only the literature stated. I agree with being it used for educational purposes.

Prague, April 20th, 2001

Acknowledgement

It is a pleasure to acknowledge the inestimable help I have received in writing of this thesis from my supervisor RNDr. Jiří Grygar, CSc. His leading, friendly advices and his patience with my delays have made good use in the final form of the text.

I was very excited by the inspiring atmosphere between all my colleagues within the Czech Group of Auger Collaboration. My first springlets of cosmic-ray physics interest were awakened by my astronomy and astrophysics lecturers at the Charles University. I owe them all a special debt of gratitude.

My thanks go out also to my friends and colleagues, who helped me in many different ways. Especially, I would like to thank to Karel Výborný for valuable discussions, to David Ondřich and to Martin Jelínek for help in obtaining of necessary literature, and to Petra Štípská and Jan Laš for moral and technical support.

Finally, I'm deeply obliged to my family for peaceful background and for the respect with my specific caprices.

Contents

Chapter 1

Introduction

As was pointed out by David Schramm, there are two great astrophysical mysteries remaining for the 21^{st} century — the first one is something, what are we looking for, but what are we still missing and the second one is something, what are we observing, but what according to our expectations shouldn't exist at all. The first great questionmark is the problem of the dark matter in the universe and the second one is the problem of ultra-high energy cosmic rays (UHECRs)[1]. This diploma thesis is treating the second puzzle.

The study of cosmic rays is the main subject of interest of the new science branch, which is standing between particle physics and astrophysics — astroparticle physics. Astroparticle physics follows the very perspective trend of last decades, when co-operating and joining of different science branches is quickly bringing many interesting new results.

The research of ultra-high energy cosmic rays is now in a similar situation, in which was the research of gamma ray bursts five years ago, before discovery of radio and optical afterglows. The whole branch is going through very quick theoretical development, but is starving for bigger volume of observational data. We have now many theories which are more or less successfully (and exotically) explaining some problems of UHECRs, but we are unable to decide which one is correct, because parameters of all these theories are still almost without experimental constraints. Each such hypothesis is speculative — up to date we know only about 100 UHECR events and about 20 EHECR events[2].

We can simply say, that "final" solution can't be found without new and bigger datasets from dedicated experiments. But the time of great changes is coming...

Maybe the most important near-future project is Project Auger. The southern site of the so called Pierre Auger Observatory (PAO) is already being built in

[1] In this thesis we define UHECRs as the cosmic rays with energy $\geq 4 \times 10^{19}$ eV. More detailed discussion about classification of cosmic rays (CRs) is done in section 1.2.

[2] EHECR — Extremely High Energetic Cosmic Ray — is in this work defined as a particle with the energy above 10^{20} eV. For the detailed statistics see chapter 4.

Argentina and it is expected that PAO should get first calibration data in this year and first scientifically useful data in 2003. Project Auger is international project and nineteen countries (one of them is Czech Republic) is participating in it. This hybrid detector is described in section 3.8.1, but here we can state, that southern PAO will be approximately thirty times larger than contemporary largest detector and it is expected that it will detect several tens of EHECRs per one year, so most probably Auger will in one year overcome the total number of EHECRs known today.

The author of this diploma thesis is a member of the Czech Auger workgroup and this work was done in the frame of the Center for Particle Physics, research project No. LN00A006 of Ministry of Education of the Czech Republic.

In accordance with statements introduced above, the diploma thesis follows two main goals. First, it has to provide an actual overview of existing and prepared experiments[3], to collect available experimental data from these projects[4] and to describe the current theoretical status of the field[5], especially for the employment by the members of the Czech Auger group and other interested persons. Its second goal is the detailed analysis of the influence of existing magnetic fields on the propagation of UHECRs. The chapter No. 6 constitutes the main part of my original contribution to the progress of the project. The created models of magnetic fields are ready to use on future data produced within Auger project.

1.1 History of Cosmic Ray Research

The research of cosmic rays started several years after the beginning of the 20^{th} century. The physicists were detecting some strange new type of penetrating radiation even with shielded electroscopes. Some measurements were done also out on sea, far away from any radioactive material. First man, who was speculating about cosmic origin of this radiation, was Theodor Wulf in 1910 — he realized several experiments on Eiffel Tower and found much slower decrease of ray flux with the increasing height above the ground level than was expected. After him came more widely cited Victor Hess in 1912 [49] with his balloon experiments — he proved the Wulf's conclusions and furthermore — he found that the radiation level actually rose with height. After that it was quite clear that radiation was coming from outer space.

Quite shortly after discovery of cosmic rays were formulated first hypothesis about its origin. For example, famous physicist Robert Millikan [72] in 1928 thought that cosmic ray are originating as energetic gamma photons during creations of heavier nuclei from primary protons and electrons[6]. His theory was

[3] See chapter 3

[4] See chapter 4.

[5] See chapter 5 and following.

[6] Neutron wasn't discovered yet.

overcome by Arthur Compton [28] in 1933, who discovered the dependence of cosmic ray intensity on the magnetic latitude and concluded that cosmic rays are made predominantly from charged particles.

This first very important experimental result was followed by another one in five years. In 1938 Pierre Auger and Roland Maze [5] showed that cosmic rays separated by distance around 20 meters are still coming in time coincidence. Subsequent experiments found time coincidences even at distances around 200 meters. Their proposed explanation is still valid — detected particles are only secondaries from common sources. Particles on the ground are only products from cascading process, when from one primary cosmic ray particle are originating the so called extensive air showers (EAS). Auger and his colleagues used newly developed theory and were fascinated by computed results — according to them the observed initiating primary cosmic ray particles had energies up to 10^{15} eV — in time, when products of natural radioactivity or artificial acceleration were reaching energies only several MeV.

Like Auger and collaborators several other groups were continuing their experiments with Geiger-Müller counters used in continually growing arrays. The energy of detected events rose up to 10^{17} eV, but the handicap of unability of the direction detection was again and again more evident. This limitation was overcome by MIT group in 1953 [11], which developed a technique of reconstructing the arrival direction by measuring of arrival times of signals in scintillation counters separated by a few tens of meters. The MIT group also operated 15-counter array, called Harvard Agassiz Station, between 1954 and 1957. This array was used to derive energy spectrum of cosmic rays from 10^{15} eV to 10^{18}.

From this array was the only step to the first giant array — Volcano Ranch[7] array located in New Mexico. With this array John Linsley [64] observed first EHECR — extremely energetic particle with energy above 10^{20} eV in 1962.

Alternative methods of detection were searched from early sixties. Suga and Chudakov in 1962 pointed out the possibility of using the Earth's atmosphere as a huge scintillator. In 1968 Tanahashi and his group [46] finally succeeded in detecting fluorescence light from 10^{19} eV shower at Mt. Dodaira in Japan. This new technique was further tested in climatically more suitable Volcano Ranch and after that in Utah, where the very successful experiment Fly's Eye was developed[8].

[7] More details will be given in section 3.1.

[8] As in foregoing case, the more detailed description will be given — in 3.6.

1.2 Spectrum of Cosmic Rays

We know today we that the energy range of cosmic rays extends from 10^8 eV to 10^{20} eV[9]. Two basic types of cosmic rays introduced above are still distinguished — primary and secondary cosmic rays. Generally, primary cosmic rays consist mainly from protons ($\sim$ 90 %) and He nuclei ($\sim$ 9 %). The remaining 1 % is composed of heavier nuclei with proton numbers up to 92. Only very small fraction of primaries should be ascribed to electrons, photons and neutrinos.[10]

The energy flux of cosmic rays is rapidly decreasing with their growing energy. We observe one particle per m^2 per second with the energy of about 10^{11} eV, but only one particle per m^2 per year at the energies of about 10^{16} eV and in the EHECR range (around 10^{20} eV it is just one particle per km^2 per century (see Fig. 1.1). In this region ($10^{11} \div 10^{20}$ eV) the energy spectrum approximately fulfils simple power law:

$$F(E)\mathrm{d}E = CE^{-x}\mathrm{d}E, \tag{1.1}$$

where F is the energy flux, E the energy, C is the constant of proportionality and x is characterizing the slope of the curve and in the first approximation is equal to 2.7. In the detailed view we can see that x isn't a constant, but it varies slightly — the two most important regions of change were named knee (about $10^{15.5}$ eV; spectrum becomes steeper) and ankle (about $10^{18.8}$ eV; spectrum becomes flatter) in the analogy with features of human leg. The basic form of the spectrum curve is associated with the effectivity of the most common acceleration mechanism in the variable magnetic fields[11], but these slope changes are very puzzling. The existence of the knee was in the last years somehow acceptably explained, but the question about the ankle remains unanswered. Of course, some hypotheses were presented and we will discuss them in later chapters.

Observations of primary cosmic rays are carried above the Earth atmosphere and orbital probes, rockets and high-altitude balloons are used for the detection. For the "knee" energies and above are detector surfaces at these devices too small for any valuable particle detection rate and the use of ground arrays of detectors is necessary. This group of detectors analyses the properties of secondary cosmic ray particle showers and reconstructs from it the parameters of primaries using of Monte Carlo computer models of hadronic interactions. Actual methods of detection of CRs using ground detectors will be analysed in the next chapter.

The spatial distribution of CRs is almost isotropic. Only in the lowest energy region ($10^8 \div 10^{11}$ eV) we observe an excess in the direction of the Sun. This part of spectrum shows also the 11-year variability in flux and is clearly associated with solar activity. The energetic part of cosmic ray spectrum owes its isotropy

[9] The 10^{20} eV limit is not rigid at all. May be there are also particles with energies 10^{21} eV or 10^{22} eV, but were not detected yet. See discussion namely in chapter 5.

[10] We have to emphasize that in the region of UHECRs and EHECRs the composition is unknown and probably very different from this general view, see chapter 5.

[11] The so-called Fermi acceleration will be discussed in the paragraph 5.1.1.

to influence of magnetic fields. The well known Lorentz force is acting on every charged particle moving in any magnetic field and its influence is often characterized by the so called Larmor radius, what is the radius of the trajectory of particle with given energy in the given magnetic field:

$$r_L[kpc] \approx \frac{E[10^{18}eV]}{ZB[\mu G]}, \tag{1.2}$$

where r_L is the Larmor radius in kiloparsecs, E is the energy of the particle in 10^{18} eV, Z is the proton number and B is the intensity of magnetic field, expressed in microgausses[12].

The typical magnetic field strength in the Galaxy is in the order of μG and so the Larmor radius e.g. for proton with energy 10^{15} eV is only about 0.5 pc. This leads to simple deduction that particles are moving through the variable magnetic field in the Galaxy along very complicated trajectories and it is impossible to trace the point of their origin. The only exception is in the highest energy ranges (above 10^{19} eV) — for these particles is the Larmor radius reaches an order of kiloparsecs. But no anisotropy (with respect to Galactic plane) is observed even at these energies and so it is generally assumed that particles at highest energies have extragalactic origin. Some recent theories are challenging this statement and we will discuss it in detail in chapter 5. Sources of CRs with Galactic origin (so mainly in the range $10^{11} - 10^{18}$ eV) should be searched near supernovae and their relics. Potential sources of UHECRs and EHECRs are much rarer and will be discussed in next section.

[12]The unit gauss (G) or microgauss (μG; $1\mu G = 10^{-6}G$) is generally used in the astroparticle physics. So, we follow this convention and use this unit in the whole work instead of tesla (T) from SI system ($1T = 10^4 G$).

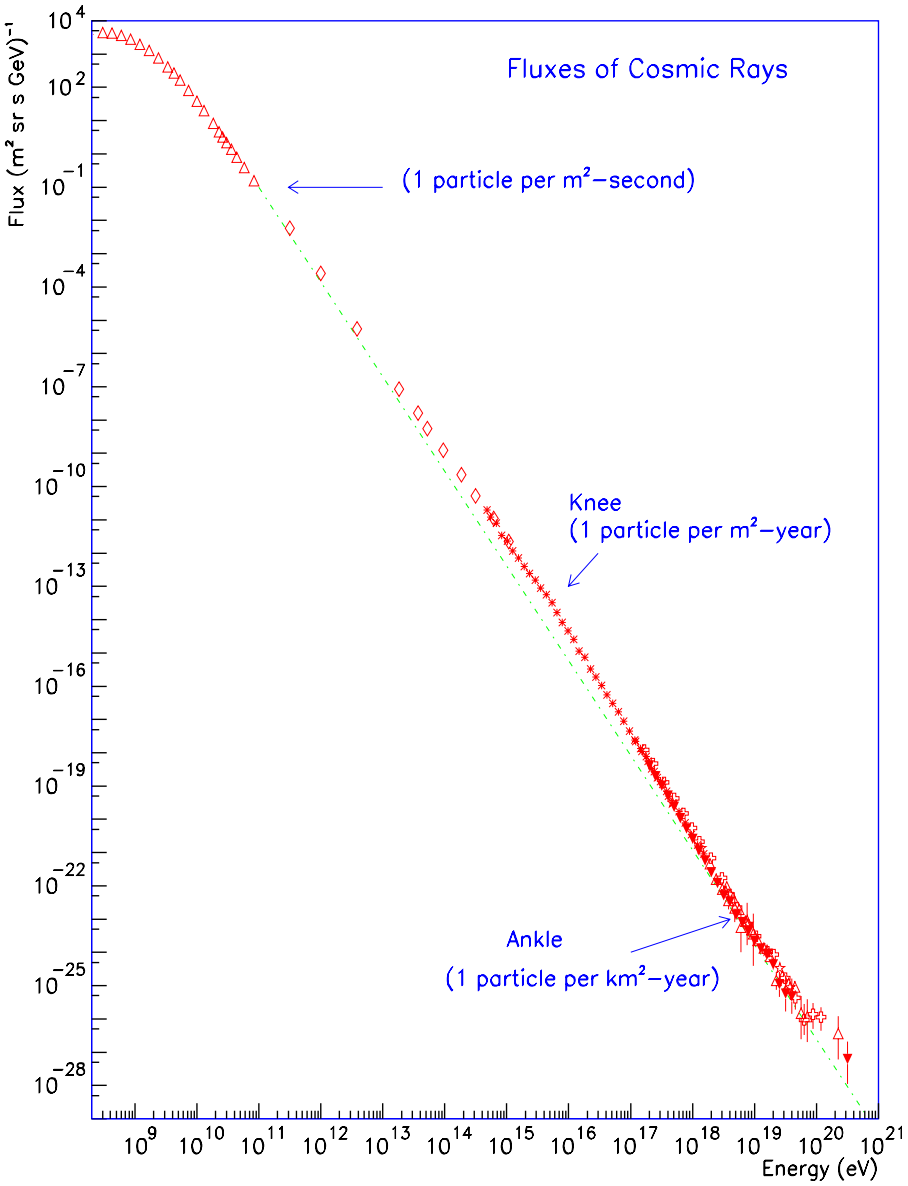

Figure 1.1: *Observed energy spectrum of cosmic rays with energies greater than 100 MeV. The spectrum should be expressed in the form of a power law from* 10^{11} *eV to* 10^{20} *eV. There are slight changes of slope about* $10^{15.5}$ *(called knee), about* $10^{17.8}$ *eV (called second knee) and finally about* $10^{18.8}$ *eV (called ankle). The dotted line shows* E^{-3} *power-law for comparison. Details for "ankle region", interesting for UHECRs, will be given in following figures. This figure was created by S. Swordy, University of Chicago (unpublished), and it is a compilation of the published results from LEAP, Proton, Akeno, AGASA, Fly's Eye, Haverah Park and Yakutsk experiments.*

1.3 Ultrahigh Energy Cosmic Rays (UHECRs)

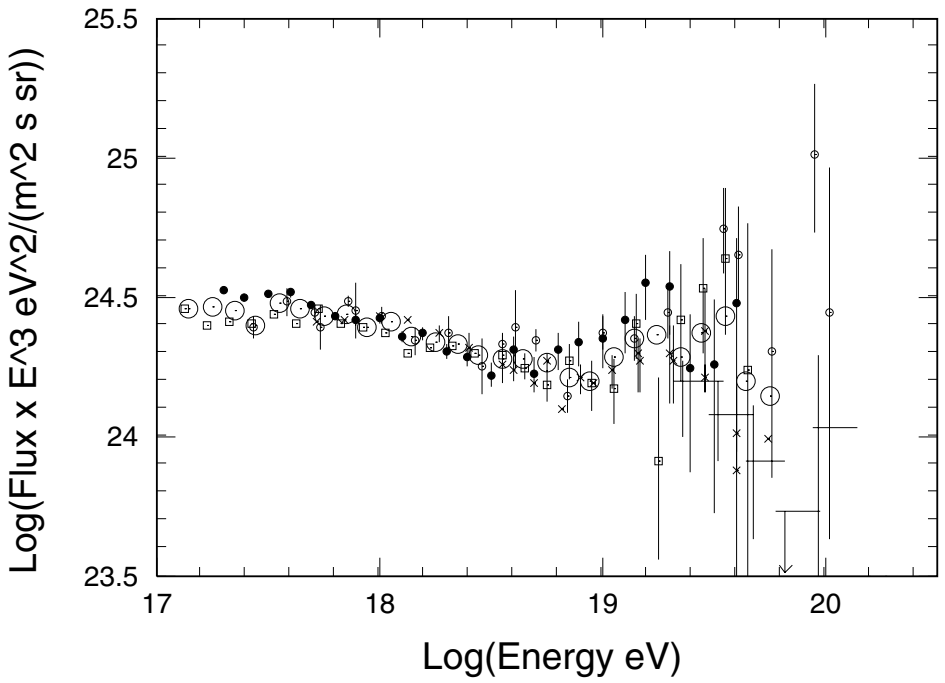

Figure 1.2: *Most energetic part (> 100 PeV) of cosmic ray spectrum. On the vertical scale is the product of energy flux of CRs and of the third power of energy (Flux* $\times$ *E^3; this or similar scales are commonly being used). The ankle around* $10^{18.8}$ *eV is clearly visible, a growing uncertainty in the measurements around* 10^{20} *is also easily recognizable. Taken from [16], compiled by M. Nagano.*

The cosmic ray particles with energies (approximately) above 4×10^{19} eV have unique position. As we have introduced in the previous section, they are obviously taken as having an extragalactic origin, because of their isotropical spatial distribution and because of non-existence of suitable sources inside our Galaxy. Furthermore, these extreme energies, about eight orders above man-made accelerators, require for known methods of acceleration extreme intensities of magnetic fields or extreme sizes of this acceleration regions. Such conditions are hardly available at any places in the universe; maybe the most favourable are large radio lobes in active radio galaxies. But even these need to have all conditions finely tuned and only in such a case the theoretically derived maximum attainable energy is achieving 10^{21} eV.

But there is another hitch. The suitable sources are relatively far from Earth and relatively rare. The nearest one is the active radio galaxy M87, which is about 20 Mpc from Earth and the next one is radio galaxy NGC 315, which is

separated by 50 Mpc from Earth. Farther galaxies are not so interesting because of the existence of Greisen - Zatsepin - Kuzmin (GZK) cutoff. In 1966, very shortly after discovery of cosmic microwave background radiation (CMBR) [78], Greisen [43] and independently Zatsepin and Kuzmin [108] published short articles, where they evaluate the effects of interactions with CMBR. They concluded, that CMBR quite effectively degrades the energy of most energetic CRs — protons are undergoing the photopion production, nuclei are photodisintegrated and photons are creating pairs. The critical threshold for effectivity of these processes is different for individual types of cosmic rays, but in this introduction we can summarize, that it is positioned around the energy of photopion resonance, around 4×10^{19} eV and so around energy, which defines the membership in UHECRs. For probably most important component, protons, the attenuation length is about 6 Mpc and the mean energy loss is about 20 % per interaction. The nuclei and photons are generally lossing energy on shorter distance and more effectively. So, the critical distance for particles with energies above 10^{20} eV lies around 50 Mpc (or 100 Mpc when we use less strict criteria for acceleration sites conditions). Furthermore, observed UHECRs and EHECRs are rather isotropical (but the statistics is very poor) and so e.g. the M87 as the single point source is very improbable[13].

The solution of this puzzle is still unknown. Many hypotheses were proposed, but we are now waiting for further data, mainly from builded Project Auger. These hypotheses are ranging from simple solutions in which the M87 is a single source indeed, and the trajectories are isotropised by the strong magnetic field in the Galactic halo, to fundamental ones, which are introducing Lorentz-transformation violation or decay of GUT particles originated shortly after the Big Bang.

We can conclude, that all these fascinating problems and themes, which were only shortly touched in this section, will be subsequently worked through in the rest of this work.

[13]But not completely excluded — due to influence of different magnetic fields. See mainly chapter 6.

Chapter 2

Methods of Detection of UHECR

As was already mentioned in 1.1, there are two basic methods of detection of ultra-high energy cosmic rays — or more generally of detection of extensive air showers.

Earth atmosphere is acting as a large calorimeter on an incident cosmic ray and it has a vertical thickness of 26 radiation lengths and about 11 interaction lengths, which are acting in the development of extensive air shower. Auger's original idea was to distribute a sufficient number of particle counters across a large area and detect the densities of particles which are arriving to a detection level.

Second method exploits the excitation of nitrogen molecules by particles during evolution of the shower and uses the observation of fluorescence light in the $300 \div 400$ nm band. The light is detected by photomultipliers and the profile of the shower in the atmosphere is observed rather directly.

2.1 Ground Arrays of Detectors

Pioneering research of Auger and his team showed that there is a relation between energy of primary particle and between the size of surface, where we are able to detect secondary particles. Quite in accordance with out intuition, the surface is larger when the primary energy is bigger. So also the separation distance d of individual detectors is proportional to energy of particles, what will be in the focus of our interest. For UHECRs d is generally in range of hundreds of meters. The detectors are deployed often in regular grid, total surface covered by detectors for UHECR detection should be at least several square kilometers (see e.g. Figs. 1.1 & 3.1.) The density of at least one charged particle type or/and muons or/and air Čerenkov photons, is measured at each detector location. Sizes of individual detector is ranging from 1 to 20 m^2 with the exception of muon detectors, which should be optimally much larger. As individual detectors scintillation and water Čerenkov detectors are used.

2.1.1 Extensive Air Showers

The properties of extensive air showers (EAS) are simulated using of Monte Carlo programs as AIRES [86], CORSIKA [25] or MOCCA [54]. At energy ranges of UHECRs simulation is a bit delicate, because the interaction energies are several orders higher, than those attainable in man-made accelerators. Generally, the models are cross-checked at lower energies and then extrapolated only to higher ranges. The most commonly used models for high energy hadronic interactions are SIBYLL, VENUS, QGSJet and DPMJet. These models were recently analyzed by KASCADE group [58] and this study indicates that QGSJet is reproducing the measured data in the best way. However, when simulating a shower, these models are used only for the first few interactions and therefore the main shower parameters don't depend strongly on the used model[1].

So, we are able to introduce [16] typical parameters of EAS, which are obtained form simulations, e.g. for vertical EAS initiated by 10 EeV proton: At sea level, where the atmospheric thickness is 1033 g/cm^2, the number of secondaries (with energies above 200 keV) is about 3×10^{10}. 99 % of these are photons and electrons or positrons in a ratio 6:1. Their energies are mostly in the range from 1 to 10 MeV and they transport 85 % of the total shower energy. The remaining 1 % of total number is shared between muons with an average energy 1 GeV (muons are carrying about 10 % of energy), pions with a few GeV energies (carrying 4 % of total energy), and, in smaller proportions, contains also some neutrinos and baryons. The lateral development of the shower is represented by Molière radius (or the distance within which 90 % of the total energy of the shower is contained), that in the average is about 70 meters. Actual extension of the whole shower is, of course, much larger, e.g. at a distance 1 km from shower core the average densities of photons/electrons/muons are 30/2/1 per m^2. The maximum size of shower is reached at an atmospheric depth of about 830 g/cm^2 (or at an altitude of 1800 meters), where it contains about 7×10^9 electrons and emits fluorescence light detected with fluorescence detectors.

Showers initiated by heavier nuclei with mass number A and energy E should be approximated as a superposition of A showers initiated by nucleons with energy E/A. Therefore these showers are less penetrating, e.g. iron is reaching its maximum size at depths roughly 100 g/cm^2 higher than proton. This criterion is generally used in the analysis of fluorescence detector events (See section 2.2 & Fig. 2.1.)

Nuclei are distinguished from nucleons (or from ultra-high energy photons) on the ground detector arrays using two basic criteria: the proportion of muons compared to the electromagnetic component of the shower and the rise time of the detected signal. The muons in shower are coming form the decay of charged pions when they reach energy low enough that their interaction length becomes smaller than their interaction length. This happens earlier for heavier nuclei and

[1] However, the identification of the type of the primary particle is much more problematic.

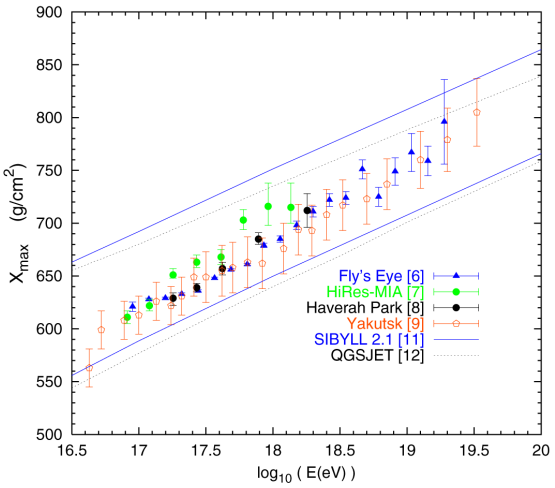

Figure 2.1: *Average depth of shower maximum (X_{max}) vs. energy compared to the calculated values for protons (upper curves) and Fe primaries (lower curves)). From [41].*

thus the resulting shower is richer in muons than a proton shower. And, since muons are produced earlier in the shower development, they reach ground also earlier, in comparison to the electromagnetic component, that exhibits a greater delay generated in many interactions.

2.1.2 Detector Signal Analysis

First basic information, which is necessary to be obtained from raw data, is the arrival direction of the primary ray, and hence the direction of the shower axis. This parameter is computed from the relative arrival times from at least three individual noncollinear detectors. As a first approximation, the front shower disc is assumed to be planar and sweeping across the array with the velocity of light. Two factors are limiting the accuracy of positioning — the accuracy of timing and synchronization of time measurements at individual detectors and the range of the whole giant array. The shower disc has generally the thickness of about several nanoseconds close to the shower core and this thickness is growing to a several microseconds at separations in order of kilometers from the core. So the large detectors the have advantage in the determination of front reconstruction. The accuracy of giant arrays around the world are spread from 1° to 5°.

Second key parameter of the primary particle is its energy, but here its determination is much more difficult. First step in its evaluation is the determination of core position at the ground. For this reason the lateral distribution function is used, e.g. for scintillation detectors the so called Nishimura-Kamata-Greisen

function proposed in [42]:

$$S(r) = k \left(\frac{r}{r_0}\right)^{-\alpha} \left(1 + \frac{r}{r_0}\right)^{-(\eta-\alpha)}, \tag{2.1}$$

where $S(r)$ is the density of particles hitting a scintillator at distance r, r_0 is the Molière unit (the product of one radiation length and the rms deflection of a particle of critical energy traversing one radiation length), and α and η are determined empirically from the data; k is proportional to the shower size.

The trial core position is set and then the algorithms based on chi-square minimization or maximum-likelihood procedure are processed; the goal is to find the best fit for a new core position between computed and measured data. After the core position is found, planar description of UHECR shower is modified to more realistic spherical one, with curvature in order of kilometers [67]. In principle, the shower size and energy, should be determined using the lateral distribution function. However, especially, for large arrays $d \gg r_0$, and it is extremely unlikely that any density will be measured at $r < r_0$. Furthermore, as was early recognized, shower sizes for particular energy are stochastically fluctuating, depending on the individual shower development. So, these considerations led Hillas [52] to conclusion, that the more appropriate quantity is the density of the shower at large distances from the core.

In the Haverah Park experiment (see section 3.3) the first conversion from $\rho(600)$ (density in the distance 600 meters from the shower core per m^2) to primary energy E_0 was evaluated [53]:

$$E_0[eV] = 7.04 \times 10^{17} \times \rho(600)^{1.018} \tag{2.2}$$

For the purposes of Pierre Auger Observatory this equation was recently reevaluated [7] using MOCCA code with SIBYLL hadronic model:

$$E_0[eV] = 5.25 \times 10^{17} \times \rho(600)^{1.023}, \tag{2.3}$$

so the Haverah Park energies are probably overestimated by 25%.

Another important equation comes from AGASA [76], where instead of $\rho(600)$ factor $S(600)$ is used. Parameter $S(600)$ is determined by energy losses in a scintillator of 50-mm thickness at 600 meters, in units of vertically penetrating particles:

$$E_0[eV] = 2.15 \times 10^{17} \times S(600)^{1.015} \tag{2.4}$$

The comparison between these two last equations is quite good — within 15 %, what was experimentally tested at AGASA [85]. For the extremely situated detectors as in Yakutsk, it is also quite important to follow specific factors as temperature, which also influences the sensitivity of the detector.

2.1.3 Scintillation Detectors

Scintillation detectors are historic devices, e.g. already Rutherford used a scintillating zinc sulphide screen to count α-particles in his famous experiment, in which he discovered the existence of atomic nucleus. Nowadays there is only one modification — a photomultiplier is used to produce large number of secondary electrons, instead of the observations by the naked eye.

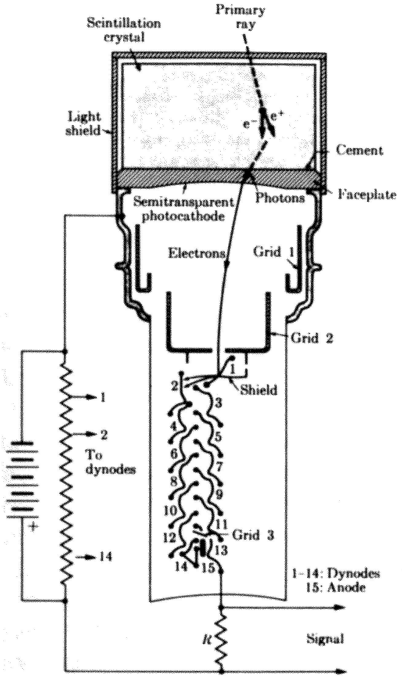

Figure 2.2: *A scintillation detector showing the large scintillation crystal and the photomultiplier tube (type RCA 7046). From [37].*

The scheme, illustrated on 2.2 is the following: electrons, liberated by cosmic ray particle, produce photons inside the crystal and these photons hit the semitransparent photocathode which again liberates photoelectrons. These are accelerated and focused onto multiplier arrangement. The result is a large pulse arriving at the anode, which size is proportional to the total energy dE liberated in the scintillation crystal. There are two main disadvantages of this system — first, the scintillation material converts only about 3 % of the liberated electron energy into useable optical photons; second, the cathode efficiency is only about $10 \div 20$ %, so only one of $5 \div 10$ photons arriving at the photocathode initiate the cascade in dynodes.

The materials used in scintillation detectors are sodium iodide, which has maximum photon emission at -188 °C. Sodium iodide is doped with thallium,

which has higher efficiency at the room temperature, or replaced by caesium iodide. Organic scintillators as liquid p-terphenyl or anthracene and trans-stiblene are also used.

2.1.4 Water Čerenkov Detectors

When a fast particle moves through a medium at velocity v, greater than the velocity of light in that medium (so $v > c/n$; c is speed of light, n is a refractive index of given medium), it emits the so-called Čerenkov radiation.

The physical principle of this effect rests in a polarization of medium by the relativistically moving particle. A charged particle moving slowly through a transparent material will polarize the medium along its trajectory. The atoms around the particle are transformed into a little dipoles. When the particle moves to another point, they relax to their normal state. Owing to complete symmetry of this effect no resulting field reaching larger distances is produced. However, the situation differs qualitatively, when particle is moving relativistically. The field is no longer symmetrical along the path of flight and each element of the track is radiating. However, the elementary waves generally interfere destructively and there is then no visible effect at large distances. Only when the velocity of the particle is higher than the phase velocity of the light in that medium it will produce field detectable at distant point. Waves from the different points of the track combine to form a plane wavefront.

The wavefronts only add up to produce coherent radiation in a particular direction θ with respect to the velocity vector of the particle, so the radiation should be observed only in a narrow cone along the track. The apex angle of this cone θ is given by formula $\cos\theta = c/vn$. The intensity of radiation is given by [69]:

$$I(\nu) = \frac{\nu Q^2 v}{4\pi\varepsilon_0 c^3}\left(1 - \frac{c^2}{n^2 v^2}\right), \tag{2.5}$$

where ν is the frequency of the emitted radiation, Q is the charge of a particle in coulombs and ε_0 is the permitivity of vacuum. It should be noticed, that refractive index n depends on the frequency of emitted radiation ν.

In practice, no measurements of the wavefront are realized in detectors, although this can be achieved in laboratory experiments. In common detectors we measure only the total emitted light. The medium determines threshold velocity for detection, in UHECR experiments pure water is mainly used. The principal problem of this detectors is very low light yield and photomultipliers should be used to produce any measurable signal.

2.2 Fluorescence Detectors

Fluorescence detectors are detecting mainly the UV light ($300 \div 400$ nm) emitted by nitrogen molecules in the air. Instead of sampling a shower with many detectors on a ground grid, the fluorescence detector follows the trajectory of the shower. For this reason, the whole observed sky is segmented, and each segment (typically $\sim 1°$) is observed by its own photomultiplier. The emission efficiency (ratio of emitted energy in fluorescence light to the deposited one) of the emission is poor (about 1%), the detector sees the shower as a variable light bulb moving at the speed of light along the shower axis. A rough estimate of the equivalent radiated power is $3 \times E[10^{18}\text{eV}]$ watts at shower maximum. For this reason, observation should be made only during clear moonless nights, so the duty cycle is only about 10% and under favorable conditions EHECR showers should be detected at distances as large as 20 km — at Fly's Eye or HiRes detectors (see sections 3.6 & 3.7). The fluorescence yield [16] is 4 photons per electron per meter at ground level.

A fit on the pattern of the hit photomultiplier tubes determines with precision better than 1° the plane containing detector and the shower axis (see Fig. 2.2). In the so-called stereo mode, when the EAS is observed by at least two fluorescence detectors separated at least by few kilometers, two planes are reconstructed and their intersection gives incident direction with quite good precision. In mono mode, when only one detectors observes EAS, it is necessary to reconstruct the angle ψ (see Fig. 2.2) using of arrival times on individual photomultipliers. Most precise will be the proposed hybrid measurement (for first time it should be realized at PAO), when the information from ground array will be combined with information about detection plane from fluorescence measurement; the expected angular precision is around 0.2°.

The fluorescence technique is the most appropriate for energy measurements — atmosphere acts like large calorimeter and thus the emitted energy is proportional to a number of charged particles in the shower. The longitudinal development of the shower is parameterized by the analytical Gaisser-Hillas function [16] giving the size of shower N_e (the number of electrons in the shower) as the function of atmospheric depth x (in g/cm^2):

$$N_e(x) = N_{max} \left(\frac{x - x_0}{X_max - x_0} \right)^{(X_max - x_0)/\lambda} e^{(X_max - x)/\lambda}, \tag{2.6}$$

where λ is a constant equal to 70 g/cm^2, x_0 is the depth at which the first interaction occurs, and X_max is the position of the shower maximum. The total energy of the shower (or the energy of the primary, E_0) is then proportional to the integral of this function, knowing that the average energy of one created particle is 2.2 MeV/(g.cm^{-2}) and that the energy fraction of this electromagnetic

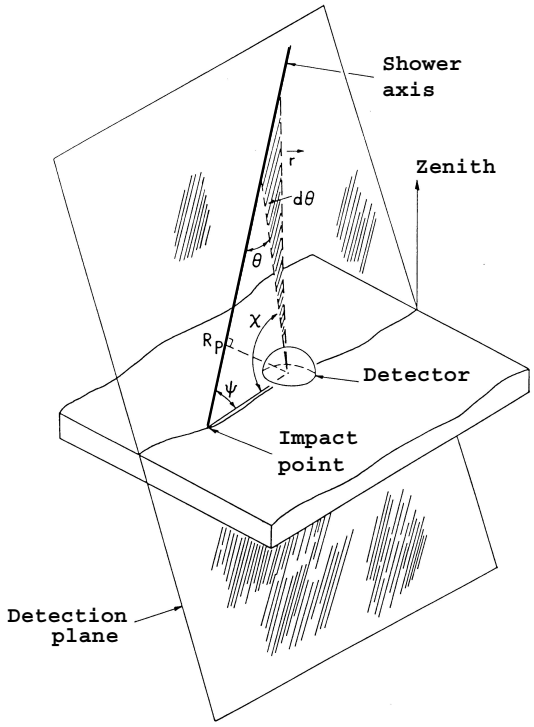

Figure 2.3: *Schematic drawing of fluorescence detector. On the figure the geometry of extensive air shower is visible as seen with any ground fluorescence detector, this scheme was created particularly for Fly's Eye detector. The detection plane is specified by the air shower (approximated as a line) and by the center of detector (point). This plane should be reconstructed using of fits to the spatial patterns of hit photomultiplier tubes, which must lie along a great circle on the celestial sphere. The angle ψ and impact parameter R_p are obtained by fits to observation angles χ_i vs time of observation. Figure taken from [10].*

component is $80 \div 90$ % [75]:

$$E_0[eV] = 2.65 \times 10^6 \times \int_0^\infty N_e dx \tag{2.7}$$

In practice also several effects should be taken in account, which are complicating the evaluation and raising the uncertainty of the result. These are subtraction of the direct and diffused Čerenkov light, the wavelength-dependent Rayleigh and Mie scatterings and the dependence of the attenuation on the altitude. The systematic error is dependent on the mode (mono,stereo, hybrid) of the fluorescence detector, and for HiRes it should be about 25% in mono mode and 3% in stereo mode. The latter value around 3% it will be probably true also for the planned hybrid detectors.

Chapter 3

Existing Experiments and Future Projects

Up to now five ground giant arrays successfully measured (or are still measuring) the flux of UHECRs — in chronological order of its start date of operation it was Volcano Ranch, SUGAR, Haverah Park, Yakutsk and AGASA. Furthermore, two fluorescence detectors functioned for detection of UHECRs — pioneering detector Fly's Eye and its successor HiRes. The properties and specialties of these projects will be discussed in following sections. The most important future projects in preparation will be mentioned too — namely there are sections about Project Auger and its contemporary status, about Telescope Array and about orbital OWL project.

Experiment	Detector Types	Surface Size	Number of detectors	Covered area [km^2]	Notes
Volcano Ranch	scintillators	3.3 m^2	19	8	
	muon detectors (>220 MeV)	3.3 m^2	19		
SUGAR	muon detectors (>0.75 GeV)	2 × 6 m^2	54	60	
Haverah Park	water Čerenkov	34 m^2	4	12	
	water Čerenkov	2.25 ∼ 54 m^2	28		
	water Čerenkov	1 m^2	30	0.3	by the array center
Yakutsk	scintillators	2 ∼ 4 m^2	58	18	up to 1995
	muon detectors (>1 GeV)	20 m^2	5	10	from 1996
	muon detector (>0.5 GeV)	192 m^2	1		
	air Čerenkov phototube	5" ∼ 15"	45		
AGASA	scintillators	2.2 m^2	111	100	
	muon detectors (>0.5 GeV)	2.4 ∼ 10 m^2	29	50	
	scintillators	1 m^2	159	1	1-km^2 array
	muon detectors	25 m^2	9	1	

Table 3.1: Parameters of detectors at existing surface arrays, adapted from [75].

3.1 Volcano Ranch

As first giant ground array for detection of cosmic rays was constructed at Volcano Ranch site in New Mexico, USA [68]. It has been located at 35°09' northern latitude and 106°47' western longitude, 1770 meters above sea level (atmospheric depth 834 g/cm^2). The array consisted of 19 3.3-m^2 plastic scintillators, each viewed with a 5-inch photomultiplier. The regular pattern of the detector is visible on Fig. 3.1, the array spacing d was 884 m during approx. 650 days of operation between years 1959 and 1963. Furthermore, there was added one more scintillation detector, shielded with 10 cm lead plate, for muon detection $E_\mu > 220$ MeV.

From Volcano Ranch came our first information about cosmic ray spectrum above 10^{18} eV and also the first about the spectrum flattening in this region, in other words about the existence of an ankle. The project leader, Linsley made also the first rough analysis of the direction distribution and wrote an article about first EHECR particle [64] ever detected. This particle was detected in February 1962 and after corrections in the following years it has the assigned energy of about 1.4×10^{20} eV [64]. This event is actually (and a bit surprisingly) fifth largest event ever detected and was reported two years before discovery of the CMBR and three years before the forecast of the GZK cutoff.

3.2 SUGAR

The Sydney University Giant ARray (SUGAR) was the only one which until now operated in the southern hemisphere at Narrabri, New South Wales, Australia [104]. It was located at 30°32' southern latitude and 149°36' eastern longitude, just 250 meters above sea level (atmospheric depth 1015 g/cm^2). This array consisted of 54 detector stations spread on the surface about 54 km^2 and was functioning from 1968 to 1979. Stations were autonomous, with local power sources. Detectors were deployed in pairs — each two 6-m^2 scintillation detectors were buried about 1.7 m below ground and thus responding to penetrating muons ($E_\mu > 0.75 \sec\theta$ GeV, where θ is zenith angle).

The spacing between detectors d was generally about one mile (1610 m) and proved to be too great. Detected densities were generally very small and the number of hit individual stations too. Even at largest detected events this situation sustained. For the ten largest events the mean number of stations struck was only 4.7 and the position of core has an error in excess of 100 m.

Each detector had 7-inch photomultiplier, timing was driven by radio signal across the array, data were logged onto audio tapes — these tapes were collected once a week and taken to Sydney for analysis. Another serious problem connected with photomultipliers was theirs after-pulsing, because logarithmic time to height converters were used. So the accuracy of energy estimation was very poor, in

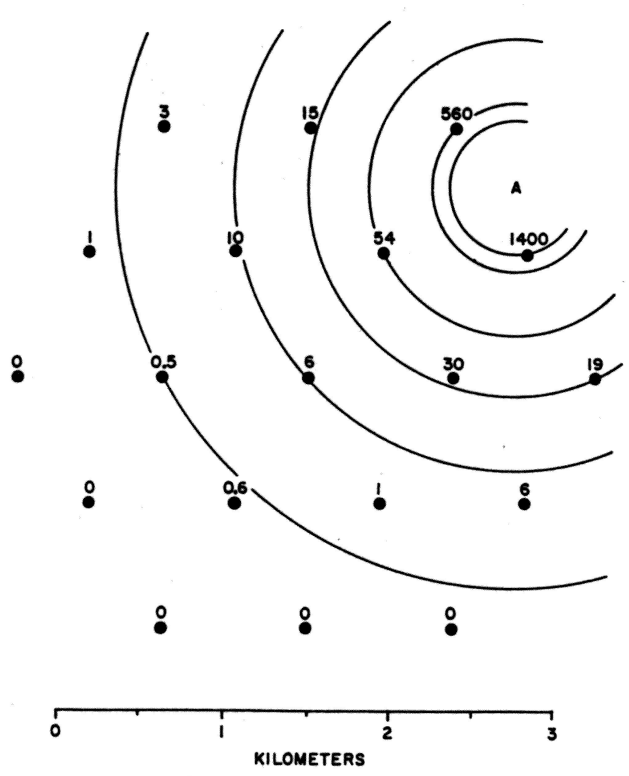

Figure 3.1: *Plan of Volcano Ranch array in February 1962. The circles represents 3.3 m^2 scintillation detectors. The numbers near the circles are the shower densities (particles/m^2) registered in this event (No. 2-4834). Point A is the estimated location of the shower core. The circular contours about that point aid in verifying the core location by inspection. Adapted from [64].*

dependence on the used model of evaluation the estimates vary with a factor of $2 \div 3$[1]. So the SUGAR events reported as above 4×10^{19} eV should be further analyzed[2] with great awareness of discussed error.

More useful are arrival directions of detected particles (used e.g. in [57]) and the novel method of data recording, which is used similarly also in its successor on the southern hemisphere — in southern PAO in Argentina, accounting, of course, for the 30 years of progress in technology.

[1]Two models were used for energy estimates — so called Hillas E model (from [51]) and SUGAR researchers' own model — so called Sydney model. From Hillas E model follows formula for primary energy E_0: $E_0[eV] = 1.64 \times 10^{18}(N_\nu \times 10^{-7})^{1.075}$, where N_ν is the showers' equivalent verical muon number. For Sydney model similar equation is valid: $E_0[eV] = 6.75 \times 10^{17}(N_\nu \times 10^{-7})^{1.11}$. From comparison analysis it seems that more suitable and precise is Hillas E model, which attains the greater accordance [104] namely with Haverah Park data. So for these reasons we use the energy data from Hillas E model in the following chapter.

[2]See also chapter 4.

3.3 Haverah Park

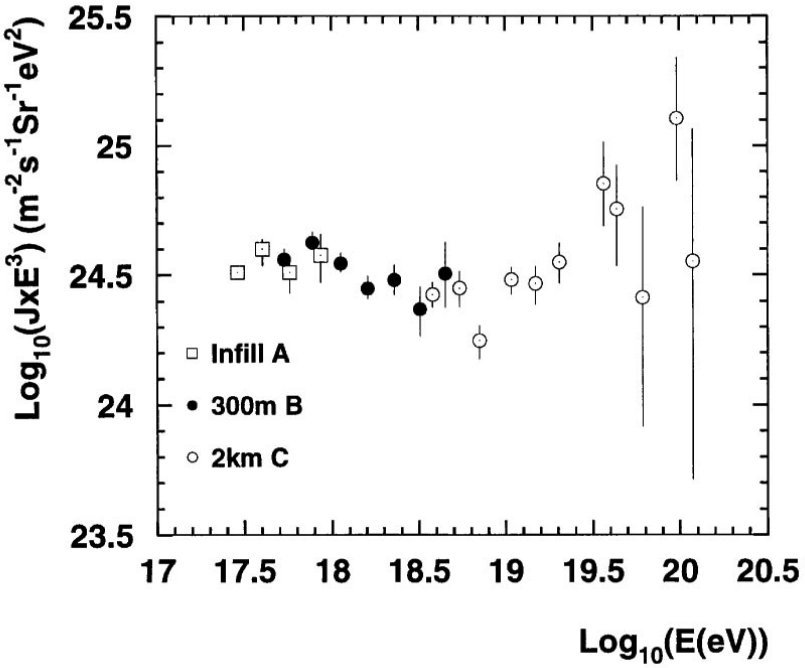

Figure 3.2: *Energy spectrum above 100 PeV from Haverah Park. Taken from [107].*

First use of more effective water Čerenkov detector arrays was realized at Haverah Park, UK from 1968 to 1987 [60]. Haverah park is located at 53°58' northern latitude and 1°38' western longitude, 200 meters above sea level (atmospheric depth 1016 g/cm^2). Detectors weren't positioned on a uniform grid. Four detectors with 500-m spacing and $34m^2$ surface created the core of the array, which was extended with six 50-m and 150-m spaced subarrays in distances of about 2 km from the array core.

Water Čerenkov detectors respond to photons in a very efficient way (not like scintillators[3]). The low energy photons (10 MeV) are almost totally absorbed and similarly at the distances > 100 m, which is most important for large showers, also electrons are almost completely absorbed. So, the detectors measured the flow of energy in the shower rather well. For comparison with e.g. SUGAR array there was up to 50 measured nonzero densities in the largest events (ranging form 100 m to 2500 m).

[3]See paragraph 2.1.3.

During the last years of the project an array of eight scintillators was also operated within 150 m of the array center for the cross-calibration with other giant arrays.

3.4 Yakutsk

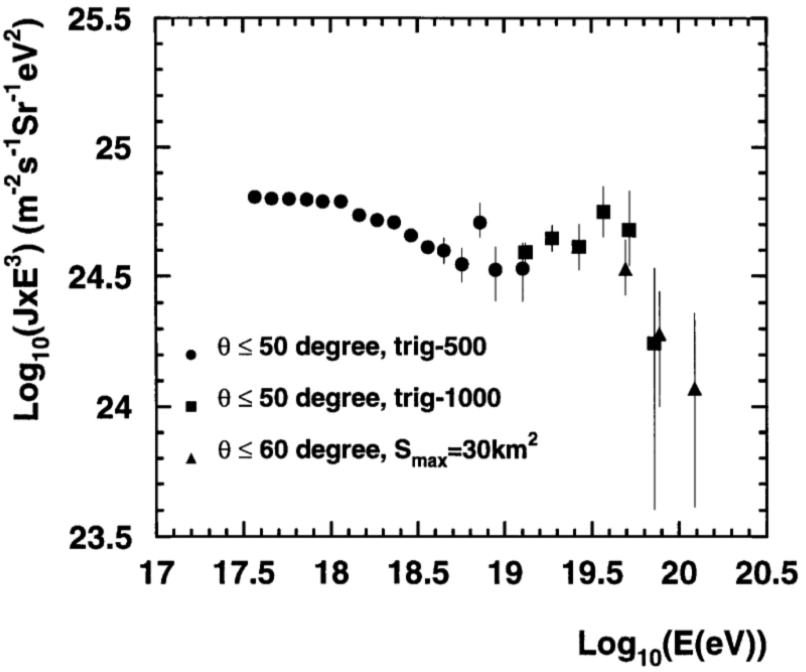

Figure 3.3: *The Yakutsk energy spectrum above 100 PeV. From [107].*

The very sophisticated scheme of scintillator and muon detector array was developed in Yakutsk, Siberia, Russia [2]. Yakutsk is situated at 61°36' northern latitude and 129°24' western longitude, only 105 meters above sea level (atmospheric depth 1020 g/cm^2), began taking data in 1970, from 1974 is covering an area of 18 km^2 and is still in operation[4]. There are three nested arrays. The inner-most is covering area about 0.0026 km^2 and consisting from 19 0.25-m^2 scintillation detectors. The next is surrounding the first one, composed form 43 2.0-m^2 scintillation detectors on the 500-m grid, covering totally 10 km^2, replenished with further 17 2.0-m^2 scintillation detectors around them with spacing 1 km. Muon detectors are situated within 1 km around array center. Seven muon

[4]But from 1995 in contracted area about 10 km^2, which is more suitable for study of air showers around 10^{19} eV, where they reported the qualitative change of shower characteristics.

20-m^2 detectors have energy threshold about 1 GeV, one 192-m^2 detector have threshold about 0.5 GeV.

Data from individual stations are collected via coaxial cable, timing signal is distributed via microwave broadcasting and the time resolution $\sim 10^{-7}$s is achieved. Other important feature of this array is the presence of 35 air Čerenkov radiation phototubes, which allows an indirect information about longitudinal development of shower and about energy evaluations (the precision of energy measurement for vertical showers is about 20 % using Čerenkov detectors' information).

3.5 AGASA

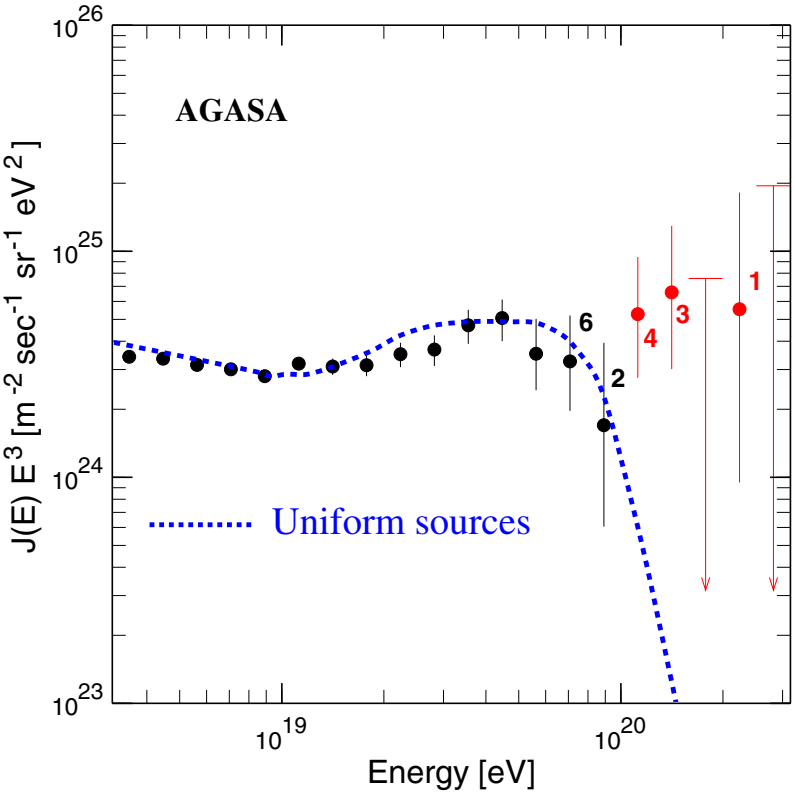

Figure 3.4: *High energy part of spectrum from AGASA experiment. The dashed curve represents the spectrum expected for extragalactic sources distributed uniformly in the universe. The arrows show 90% confidence level upper limits. The numbers attached to the data points are the number of events observed in the corresponding energy bins. From [95].*

The largest ground array constructed so far — Akeno Giant Air Shower Array — is located at Akeno, Japan, at 35°47' northern latitude and 138°30' eastern longitude, 900 meters above sea level (atmospheric depth 920 g/cm^2) [74]. The site is equipped with 111 scintillation detectors, covers 100 km^2 and is in operation from 1990 up to now. 2.2-m^2 scintillation detectors have spacing about 1 km. Each detector has its detector control unit (DCU), which records the arrival time and density of every incident signals. Several DCUs are connected in series to a common communication string consisting of two optical fibres. One fibre is used for signal sending, the another one for data acquisition. There exists also the dense array (at the southeast corner of array) covering 1 km^2 with spacing 3, 15, 30, 60 and 120 meters, which has been operated since 1979. The whole array has 27 added muon detectors, which were installed on chosen scintillator sites and their sizes are ranging from 2.4 m^2 to 10 m^2. Furthermore, as tests for the prepared experiments, there are also two scintillators with a sandwiching 1-cm lead plate[5] and two prototype water Čerenkov detectors for the Auger Project. For events above 10^{19} eV the energy resolution error is estimated as $\sim 25\%$ and the largest uncertainty of energy assignment comes from still poorly known dependence of the $S(600)$ parameter on the zenith angle.

3.6 Fly's Eye

The first realized fluorescence detector (or detectors) was situated at Dugway, Utah, USA at 40° northern latitude and 113° western longitude, about 1400 meters above sea level (atmospheric depth 869 g/cm^2) [19]. The detector was in operation from 1981 to 1992 and has two stations — Fly's Eye I and Fly's Eye II. Fly's Eye I began full operation in 1981, consisted from 67 spherical mirrors of 1.5-m diameter, each with 12 or 14 photomultipliers at the focus. Each tube viewed a 5.5°-diameter hexagonal area of the sky, in total 880 photomultipliers covered the whole sky. Fly's Eye II was completed 3.4 km from first station and began operation in 1986. Fly's Eye II consisted of 36 mirrors of the same design as No. I and its 464 photomultipliers was covering the half of sky in the direction of Fly's Eye I. Both stations should operate in stand alone mode or in stereo mode. The integrated monocular exposition time is about seven times larger than the stereo exposition [10].

Nitrogen lasers were used for the calibration of the system and for checking of the light scattering around station, vertical flashers for monitoring of atmospheric conditions and pulsing diodes in each mirror system for the determination of relative efficiency of whole detector.

The only one EHECR event was ascribed to this detector, but it was the largest cosmic ray event ever detected. It was on October 15th 1991, when Fly's Eye measured the profile of this giant event with energy 3.2×10^{20} eV (51 J).

[5] For the investigation of relative proportions of electrons and muons in the same shower.

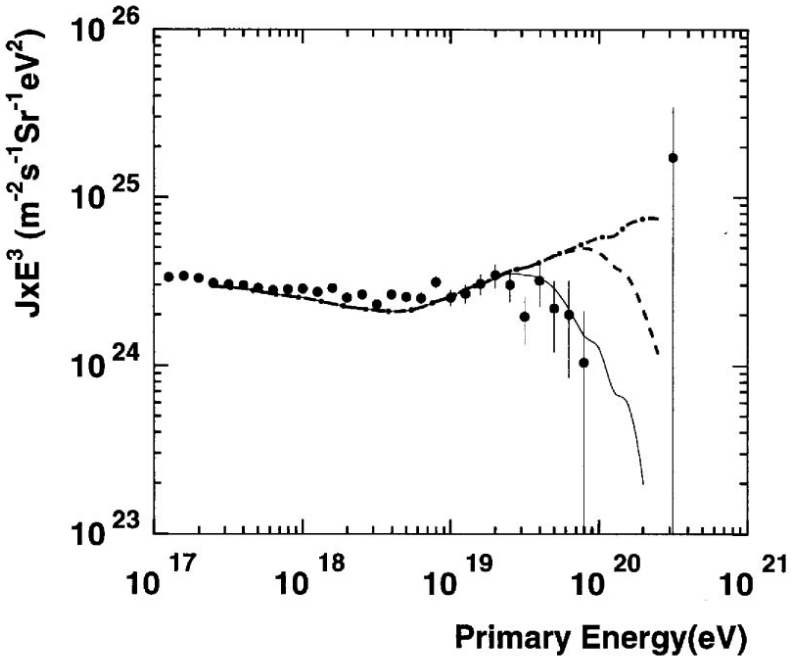

Figure 3.5: *Spectrum of CR events above 100 PeV from monocular Fly's Eye. Big dots are representing data and lines are showing predicted spectra for source energy cutoff at different energies. Solid line is for cutoff at* $10^{19.6}$ *eV, dashed line is for cutoff at* 10^{20} *eV and chain line is for cutoff at* 10^{21} *eV. From [107].*

3.7 HiRes

Because of the great success of the Fly's Eye, the next generation detector is starting its career at the same place — the so called HiRes. HiRes is taking data from 1998, but is still in its calibration phase [1]. However, several events above $6 \times 10^{19} eV$ were already announced and some analysis of events with lower energies was already done, too.

The detector is again displaced in the two sites, which are separated by 12.5 km. At one site we can find 42 mirrors while 22 mirrors are located at the other site. The diameter of each mirror is 2 m, and 256 photomultipliers attached to each mirror are observing only $1° \times 1°$ segment of the sky.

In the stereo mode the HiRes has to measure the shower maximum with a precision of about 30 g/cm^2, expected time averaged aperture (10% duty cycle) is of about 340 km^{2}sr at 10^{19} eV or 1000 km^{2}sr at 10^{20} eV. Generally, this described increase of sensitivity of detector will enable to observe showers up to a distance of about 30 km.

3.8 Prepared Experiments

3.8.1 Auger

The Pierre Auger Observatory [7] should consist of two sites — each on the one hemisphere and should enlarge existing UHECR and EHECR datasets by at least one order of magnitude. This project is prepared in the large collaboration of 19 countries, when also the Czech Republic is participating, especially in the development of fluorescence detectors.

Each site has to be a hybrid detector, where advantages of ground arrays and fluorescence detectors will be combined. The both sites should cover the whole sky and will enable to do serious statistical analysis of the distribution of UHECRs and EHECRs. Northern site is expected to be in the Millard County, Utah, USA and its realization was delayed for financial reasons, but the southern site is already being built in Argentina, province Mendoza, near city Malargüe [8].

Each site should contain 1600 ground particle detectors and three or four fluorescence detectors. Ground detectors will be spread over the enormous area of 3 000 km^2 arranged in the regular hexagonal grid with separation distance $d = 1.5$ km[6]. The exact scheme of southern PAO ground detector distribution is seen on the Fig. 3.6. Water Čerenkov detectors will be used as these ground detectors, because of their great sensitivity to low-energy photons and electrons, which are indicated at distances of about 1 km from shower center[7]. Estimated threshold of the detector with a such large separation distance will be around 4 $\times 10^{19}$ eV. The simulations are showing that for the 4×10^{19} eV shower about 11 detectors will be struck, the energy resolution will be around 10 % and direction reconstruction will be made with precision of about 1 %.

[6] A single PAO will have an aperture 7000 km^{2}sr and so it will be about ten times more efficient than the finished HiRes.

[7] See the problems with scintillation detectors at SUGAR and success of water Cherenkov detectors at Haverah Park.

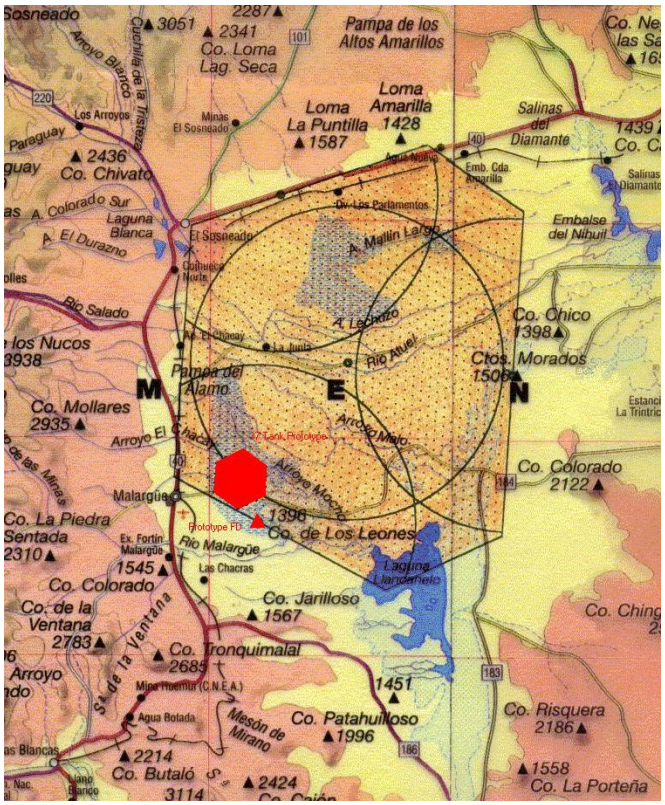

Figure 3.6: *Currently valid variant of future PAO configuration. Small dots are future positions of Čerenkov detectors; positions of four fluorescence detectors are then in the centers of depicted circles. Near the lower left corner (in the vicinity of the city Malargüe) is also drawn regular hexagon of Experimental Array and Prototype fluorescence detector (see also text).*

Each 10 m^2 water Čerenkov station will be independent, equipped with the solar cells and connected with the central station via radio link at 915 MHz, which will be used for data and command transfers. The timing will be coordinated through the GPS signal.

During clear moonless nights this ground array information will be enriched with the measurements by the fluorescence detectors. It is expected that about 10 % events will be recorded in the hybrid mode.

The central station building in Argentina is ready and the Experimental Array consisting of 37 water Čerenkov detectors is shortly before the start of operation. The current situation is depicted at the Fig. 3.7. The first test data have to be ready from the Experimental Array already late in this year. The completion of the whole instrument should be finished in four years.

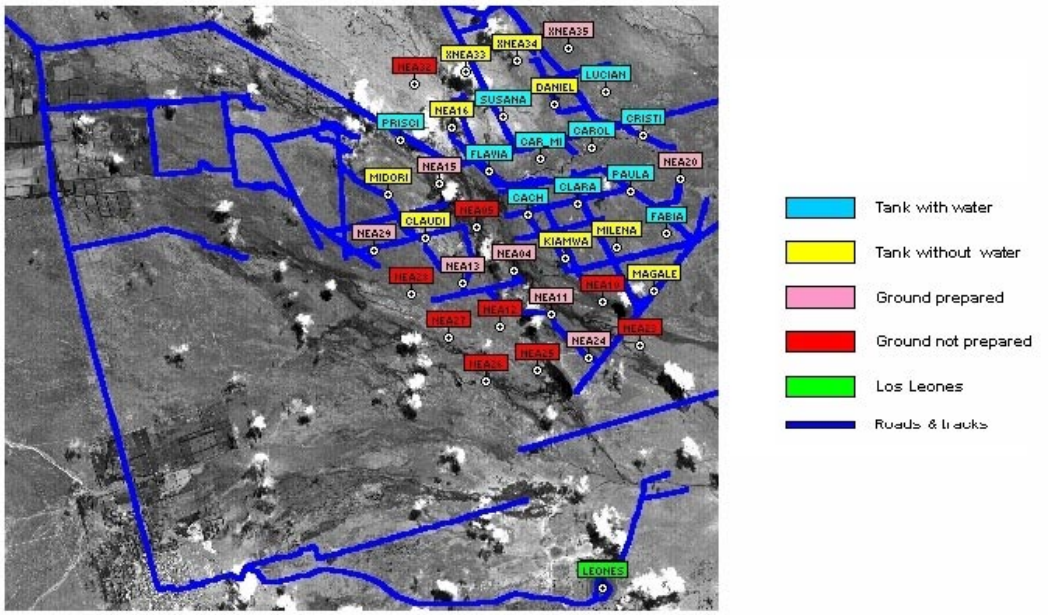

Figure 3.7: *Status of construction progress on building of Experimental Array of water Čerenkov detectors — March 2001.*

3.8.2 Telescope Array/Snake Array

The co-operative project of 21 institutions mainly from Japan, but also from the United States and Australia will greatly increase the power of fluorescence detectors. The planned telescope array consists of eight stations with a separation of 30 km. Each station consists of 42 mirrors of 3-m diameter, each mirror is equipped with 256 multipliers at focus. Tube apertures are 1°, each station is viewing the whole horizon up to elevation angle 32°, the every event is observed stereoscopically.

The Telescope Array Design Report is already available [98], but only in Japanese. This project will be incorporated with the second-stage of the HiRes project; in total ten stations will form the huge Snake Array, covering the ground from the Dugway (HiRes site) to the east of Millard County, where the northern PAO site should be built. The expected aperture should be 80 000 km^{2}sr or 8 000 km^2 with 10% duty cycle taken in account.

3.8.3 Airwatch/OWL

The challenge of overcoming of capabilities of Auger and of Telescope Array is very inspiring, but quite difficult to fulfill. The array, covering significantly greater surface or air volume, will be too expensive for realization in the following decades. Already Linsley [65] in 1979 pointed out that the solution should be in space observation of fluorescence emissions. Clear advantages are big observable area and reduced need for corrections of light extinctions, complications should be hidden in lightnings, lights from cities, oceanic biofluorescence or in high altitude clouds.

Preliminary studies of space project were carried out in Italy and in the United States and finally, both research groups are presenting a combined project called Airwatch/OWL — Orbiting Wide angle Light concentrators. Two satellites should observe the fluorescence emission, orbiting at the height 640 km, each with field of view about 30°. The covered area should be $\sim 10^6$ km^2, the expected duty cycle is around 8%. The technical requirements are very high and essential components are still not developed. Optical system e.g. utilizes two 2.5-m diameter Fresnel lenses or arrays of multianode microchannels composed in a mosaic arrangement. For the required 0.1° resolution it is necessary to have about 430 000 microdetectors for each OWL eye. The minimal time resolution is 3 μs for the readout of cascade signal going across one pixel. For recent status of this project see e.g [92] or [33].

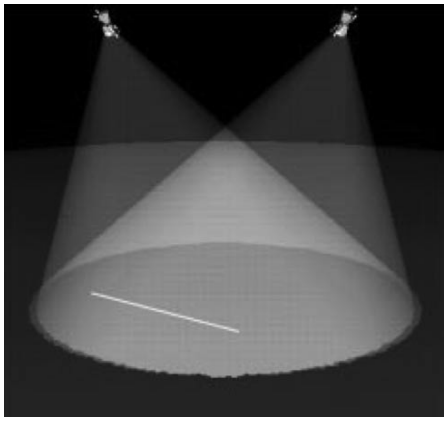

Figure 3.8: *Scheme of two OWL satellites orbiting around Earth and observing the fluorescent tracks of giant air shower. The shaded cones are illustrating the field of view of individual satellites. From [91].*

Chapter 4

Catalogues of EHECR and UHECR events

In this chapter is presented the catalogue of measured properties of UHECRs and EHECRs.

Up to now, 23 EHECRs were detected, eight of them is from AGASA, eight suspicious events is from SUGAR, one is from Volcano Ranch, one is from Yakutsk and the last one is from Fly's Eye. The presented table of EHECRs is complete and was compiled using of [104], [48], [88], [75] and [100].

Up to now, ~ 200 UHECR events is known. SUGAR have reported 80 particles above 4×10^{19} eV [104] and AGASA has 58 particles in the catalogue from the last year [48]. From other experiments the individual catalogues were not published, but we know from [88], [75] and [100], that in Haverah Park 27 UHECR particles were detected, ~ 20 UHECR particles in Fly's Eye, 5 in Yakutsk and 3 in Volcano Ranch.

Further information about the properties of UHECR particles (especially from experiments Fly's Eye, Haverah Park, Yakutsk and Volcano Ranch) is available in publications [99] and [26].[1]

[1] However, these works are neither accessible on the internet nor in the libraries in the Czech Republic. Up to now, the author didn't succed in obtaining these articles from abroad, but some negotiations are conducted and hopefully the presented catalague of UHECRs will be completed soon.

Table 4.1: Complete catalogue of the parameters of the particles above 10^{20} eV (EHECRs) detected up to the second half of the year 2000. Detected EHECRs are sorted in compliance with decreasing energy. *No.* is a number of EHECR particle that is used in maps in appendix A. Date is in format *dd.mm.yy*, α is right ascension in degrees, δ is declination in degrees, l is galactic longitude in degrees, b is galactic latitude in degrees, Z is zenith angle in degrees, *Reference number* is the reference number of each experiment from individual catalogues. We stress once more that the validity of the data from SUGAR array is a bit controversial and theirs events' values in the table were derived using of the Hillas E model. This table was compiled using the data from [75], [104], [100], [64] and [20].

No.	Experiment	Energy [10^{18} eV]	Date	α [deg]	δ [deg]	l [deg]	b [deg]	Z [deg]	Reference number
1	Fly's Eye	320^{+36}_{-54}	15.10.91	85.2	48.0	163.4	9.6	43.9	
2	AGASA	213 ± 50	03.12.93	18.8	21.1	130.5	-41.4	22.9	25400-0296
3	SUGAR	197		187.5	31.8	166.6	83.4	70	14842
4	SUGAR	155		333	-56.6	335.6	-49.2	27	1705
5	AGASA	150 ± 45	30.03.97	294.5	-5.8	33.1	-13.1	44.2	01606-0578
6	SUGAR	147		354	-75.2	309.2	-41	72	12077
7	AGASA	144 ± 43	11.01.96	241.5	23.0	38.9	45.8	14.1	00123-3997
8	Volcano	140	??.02.62	306.7	46.8	84.3	4.8	11.7	2-4834
9	AGASA	134 ± 32	06.07.94	281.3	48.3	77.6	20.9	35.4	25790-0886
10	SUGAR	132		117	-3.3	222.5	11	28	4537
11	SUGAR	126		231	-31	337.6	21.4	54	14596
12	Haverah	120 ± 10	18.04.75	179	27	212	78	29	12701723
13	AGASA	120 ± 36	12.06.98	349.0	12.3	89.5	-44.3	27.3	03876-9311
14	SUGAR	116		357	-57.4	318.9	-57.7	43	13487
15	Yakutsk	110 ± 40	07.05.89	75.2	45.5	162.2	2.6	58.9	
16	SUGAR	106		147	-43.6	271.3	7.7	43	12420
17	SUGAR	106		130.5	-27.4	250.2	9	34	14427
18	Haverah	105 ± 30	05.12.71	199	44	107	73	30	9160073
19	Haverah	105 ± 5	12.01.80	201	71	119	46	37	17684312
20	AGASA	105 ± 32	22.10.96	298.5	18.7	56.8	-4.8	33.2	00120-4976
21	AGASA	104	22.09.99	345.8	33.9	98.5	-23.8		
22	Haverah	102 ± 3	31.12.70	353	19	99	-40	35	8185175
23	AGASA	101 ± 30	12.01.93	124.3	16.8	206.7	26.4	33.2	20957-0382

Table 4.2: Catalogue of the published parameters (assembled after [104]) of the particles above 4×10^{19} eV (UHECRs) detected by the SUGAR array. Detected UHECRs are sorted by the decreasing energy; the value of energy derived from the Hillas E model is used. α is right ascension in degrees, δ is declination in degrees, l is galactic longitude in degrees, b is galactic latitude in degrees, Z is zenith angle in degrees, *Reference number* is the reference number from appropriate catalogue. Dates for individual events weren't available in published articles.

Energy [10^{18} eV]	α [deg]	δ [deg]	l [deg]	b [deg]	Z [deg]	Reference number
197	187.5	31.8	166.6	83.4	70	14842
155	333	-56.6	335.6	-49.2	27	1705
147	354	-75.2	309.2	-41	72	12077
132	117	-3.3	222.5	11	28	4537
126	231	-31	337.6	21.4	54	14596
116	357	-57.4	318.9	-57.7	43	13487
106	147	-43.6	271.3	7.7	43	12420
106	130.5	-27.4	250.2	9	34	14427
98	121.5	-32	249.5	0	24	6179
86	105	-38.7	249.1	-15	31	10628
84	288	-51.4	345.8	-24	23	14691
83	204	24	18.1	79.5	64	11270
80	231	-13.5	350.1	35	29	14585
76	57	-3.7	191.8	-41.8	28	14796
76	261	-32.8	354.2	1.8	35	13294
74	135	4.3	224.7	30.4	38	7329
72	340.5	-43.2	352.8	-59.3	60	10848
70	300	-41.9	358.1	-30	51	6402
69	238.5	-9.5	359.7	32.6	32	1807
68	16.5	-68.5	300.9	-48.6	38	15219
68	181.5	20.1	244.6	77.5	68	14560
68	247.5	-0.7	14.3	30.6	31	1704
67	331.5	-32.2	14.7	-53.9	33	1696
67	69	-49.1	255.9	-42	23	14455
66	280.5	-55.6	340.1	-20.8	40	6239
65	303	13.6	54.6	-11	64	14409
65	126	-39.9	258	-1.4	62	14481
65	226.5	-31.1	334.1	23.5	55	14706
64	316.5	-65.1	329.5	-38.4	42	2207
64	189	-15.5	297.5	47.2	45	14511
62	114	-25.8	240.8	-2.5	6	14598
61	145.5	-38.1	266.8	11.1	14	14729
60	154.5	-27.7	266	23.9	48	14508
59	268.5	-81.7	311.8	-24.8	53	15055
57	216	18.6	16	67.1	69	11531
56	76.5	10	191.1	-18.1	46	14574
56	315	0.7	49.6	-27.9	69	4558
56	154.5	3.1	239.4	46.2	67	3592

Table 4.2 (contd.)

Energy [10^{18} eV]	α [deg]	δ [deg]	l [deg]	b [deg]	Z [deg]	Reference number
54	123	-38	255.2	-2.2	67	9225
54	277.5	-8.5	22.9	0.8	23	14496
53	160.5	1.5	247	49.8	38	2993
53	1.5	-27.1	30.5	-79.9	53	1830
52	337.5	-42.2	356	-57.6	54	5739
52	85.5	20.5	186.8	-5.1	57	14590
52	88.5	-64.6	274.1	-30.4	70	14473
51	303	-47.2	352.4	-32.9	64	187
50	142.5	-24.6	255.1	19.1	44	671
50	172.5	-30.8	283	28.9	52	14520
50	99	-24.7	233.7	-14.2	15	848
49	30	15.9	146.1	-43.9	49	11913
49	73.5	0.2	198.4	-25.8	49	15154
49	355.5	-0.5	88	-58.6	58	14420
48	283.5	-50.6	345.8	-21	65	439
48	19.5	-62.8	297.8	-54.1	42	14471
48	331.5	-15.5	41.2	-50	27	14586
47	144	-33.1	262.4	14	15	1810
46	12	-14.1	119.2	-76.9	41	70
46	163.5	-5.9	257.9	46.4	68	3459
46	27	3.1	149.4	-56.8	63	14431
46	315	-26.6	19.4	-38.9	46	7470
45	234	1.2	6.7	42.8	56	14605
45	94.5	-41	248.5	-23.4	43	14575
45	229.5	-78.7	310	-17.9	57	11691
45	117	-35.9	250.9	-5.2	72	2533
44	262.5	28.2	51.7	29.2	62	4331
43	93	-45.6	253.1	-25.6	22	4508
42	223.5	-88.3	303.9	-25.7	59	14493
42	3	-2.9	100	-64	40	4890
42	195	-44.7	304.5	18.1	33	13617
42	30	-78.5	298.7	-38.1	59	14950
42	327	-24.7	25.6	-48.9	38	13655
41	231	-46.6	8.6	328.3	23	14494
41	340.5	-42.8	353.6	-59.5	52	14487
41	87	6.1	200.1	-11.1	41	15232
41	183	4.5	278.6	65.5	58	4566
41	22.5	22.2	134.6	-39.8	57	14595
41	244.5	14.3	40.4	28.8	61	14548
41	255	-83	309.7	-23.7	65	14499
40	88.5	-47.8	254.8	-29.1	57	14438
40	180	-22.7	287.7	38.6	57	15067

Table 4.3: Catalogue of the published parameters of the particles above 4×10^{19} eV (UHECRs) detected by AGASA. Detected UHECRs are sorted by the decreasing energy. Date is in format $dd.mm.yy$, α is right ascension in degrees, δ is declination in degrees, l is galactic longitude in degrees, b is galactic latitude in degrees. Data are taken from [100]. Zenith angles and identification numbers weren't published yet.

Energy $[10^{18}$ eV]	Date	α [deg]	δ [deg]	l [deg]	b [deg]
213	03.12.93	18.8	21.1	130.5	-41.4
150	30.03.97	294.5	-5.8	33.1	-13.1
144	11.01.96	241.5	23.0	38.9	45.8
134	06.07.94	281.3	48.3	77.6	20.9
120	12.06.98	349.0	12.3	89.5	-44.3
105	22.10.96	298.5	18.7	56.8	-4.8
104	22.09.99	345.8	33.9	98.5	-23.8
101	12.01.93	124.3	16.8	206.7	26.4
97.9	17.12.84	277.3	35.3	63.5	19.4
92.5	13.09.92	101.0	34.9	180.5	13.9
91	29.11.91	286.5	77.2	108.8	25.6
77.6	26.01.95	168.5	57.6	145.5	55.1
75.3	22.01.99	287.8	5.3	39.9	-2.1
74.6	12.11.96	324.3	8.1	62.7	-31.3
72.1	20.11.97	167.3	41.8	171.2	64.6
71.6	28.07.99	56.5	49.5	149.8	-4.0
69.3	30.03.98	259.0	56.3	84.5	35.3
68.1	12.12.84	335.3	38.4	93.3	-15.7
64.9	12.06.93	19.0	50.0	127.0	-12.7
62.2	23.10.86	210.5	49.9	96.8	63.4
61.9	20.10.99	69.3	5.1	191.3	-26.5
61.1	27.10.98	56.3	44.9	152.4	-7.8
57.9	04.04.95	193.0	30.6	117.5	86.5
56.8	06.10.96	199.5	52.9	113.8	63.7
55.3	31.05.91	54.3	69.5	136.6	11.2
55.3	01.02.92	8.5	17.7	117.2	-45.0
55	01.08.92	172.3	57.1	143.2	56.6
54.7	05.01.86	69.5	30.1	170.4	-11.2
53.5	04.04.98	168.3	56.0	147.5	56.2
52.7	14.03.89	207.0	34.7	68.3	75.6
50.9	03.04.91	236.8	41.0	65.7	51.5
50.7	29.10.95	18.5	20.0	130.2	-42.5
49.8	26.05.00	212.0	37.1	69.3	71.0
49.7	24.12.96	214.3	37.7	68.5	69.1
49.5	25.09.99	340.0	42.6	98.8	-14.0
48.9	15.11.95	70.3	29.9	171.1	-10.8
48.8	24.01.92	268.0	47.9	74.8	29.4
48.2	26.11.87	329.3	27.6	82.1	-21.1

Table 4.3 (contd.)

Energy [10^{18} eV]	Date	α [deg]	δ [deg]	l [deg]	b [deg]
48	19.01.96	58.0	27.1	165.4	-20.4
47.8	13.05.96	269.0	74.1	105.1	29.8
46.9	03.09.98	294.0	50.7	83.1	14.0
45.1	25.11.90	244.3	-7.2	6.1	29.6
45.1	07.01.92	144.0	38.6	184.3	48.0
44.7	30.03.92	255.8	31.4	53.6	35.6
44.6	21.01.93	208.8	59.8	108.8	55.5
44.2	22.04.93	29.0	29.0	139.8	-31.7
43.9	03.03.97	294.3	71.1	103.0	21.9
43.5	20.04.91	284.8	47.8	77.9	18.4
43	08.12.96	247.8	34.6	56.2	42.8
42.9	20.10.99	60.5	51.7	150.3	-0.7
42.7	29.03.95	264.3	-1.6	22.8	15.7
42.4	10.12.91	3.0	78.6	121.0	15.9
42	28.04.97	34.5	13.8	152.9	-43.9
41.1	06.02.98	146.8	23.7	207.2	48.6
40.9	22.07.99	114.8	32.2	187.5	23.6
40.8	28.07.94	74.0	18.0	182.8	-15.5
40.7	16.08.89	87.8	58.5	154.5	15.6

Chapter 5

Origin and Propagation of UHECRs

5.1 Possible Sources & Mechanisms of UHECR Generation

5.1.1 Fermi Acceleration

The basic mechanism of the very high energy particle acceleration was first proposed by Fermi [40] in 1949. He obtained that for stochastic particle acceleration by electric fields induced by the motion of magnetic fields B, the rate of energy gain by relativistic particles of charge Ze can be written:

$$\left(\frac{\mathrm{d}E}{\mathrm{d}t}\right)_{acc} = \xi Z\ ec^2 B, \tag{5.1}$$

where $\xi < 1$ and depends on the acceleration mechanism. This was equation used by Hillas [51] in 1968 for the construction of his already classical diagram, where the suitable acceleration sites are shown and the maximum achievable energy for given proton number Z could be derived (see Fig. 5.1). On one axis is the characteristic size of the object (proportional to the mean total acceleration time) and on the other is its characteristic magnetic field strength. Generally, this diagram is still valid and suitable for first orientation at the field of possible acceleration sites.

Today two modifications of Fermi acceleration are distinguished — Fermi's original theory (the so called second order Fermi acceleration) and a more efficient first-order Fermi acceleration, developed in late 70s [9]. In the text below simplified explanation of both theories given by Protheroe [81] in 1998 is followed.

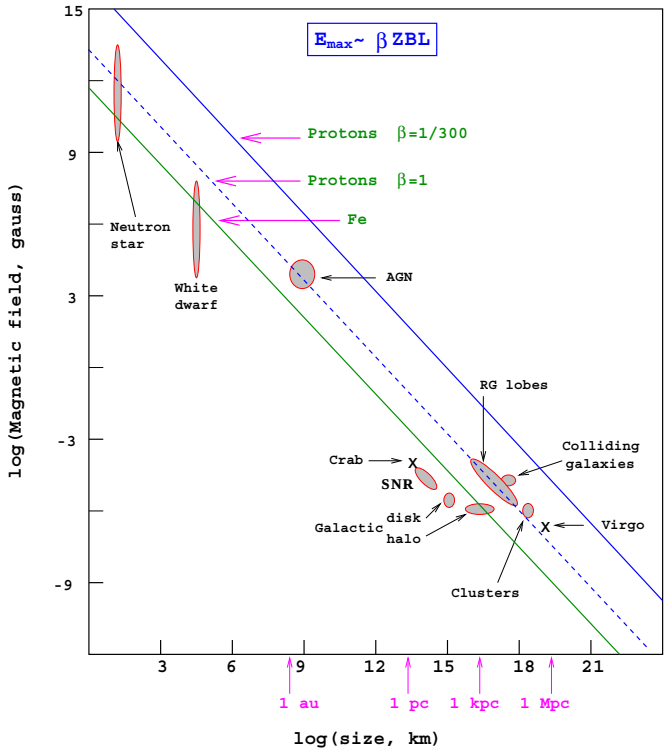

Figure 5.1: *Classical "Hillas Diagram". Size and magnetic field strength of some possible acceleration sites. Objects below the diagonal lines cannot accelerate the corresponding elements above* 10^{20} *eV or* 10^{21} *eV. SNR is abbreviation for supernovae remnants, RG lobes is for radiogalaxy lobes,* β *is the factor of efficiency of acceleration mechanism. Adapted from [51].*

Fermi's Original Theory

Gas clouds in the interstellar medium have random velocities of $\sim$ 15 km.s^{-1} superimposed on their regular motion in the galaxy. Cosmic rays gain energy on average when scattering on these magnetized clouds. A cosmic ray enters a cloud and scatters off irregularities in the magnetic field which is tied to the cloud because it is partly ionized.

In the frame of the cloud no change in energy occurs because the scattering is collisionless and so the elastic scattering between the ray and the cloud as a whole materialises, because the cloud is much more massive than the cosmic ray. Also, cosmic ray's direction is randomized by the described scatterings.

We can ascribe velocity V to the cloud, initial energy E_1 and initial momentum p_1, and also final energy E_2 and final momentum p_2 to the particle. The particle enters the cloud in the direction θ_1 with respect to the cloud's velocity V and leaves it in the direction θ_2. The energy is obtained by applying the Lorentz

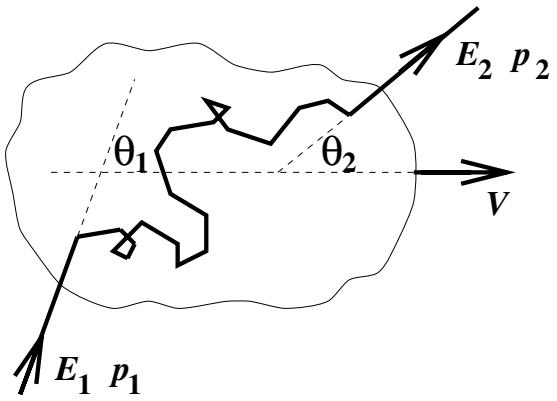

Figure 5.2: *Fermi acceleration — interaction of cosmic ray of energy E_1 with "cloud" moving with speed V. From [81].*

transformation between the laboratory frame and the cloud frame. Transforming to the cloud frame gives :

$$E_1' = \gamma E_1(1 - \beta \cos\theta_1), \tag{5.2}$$

where $\beta = V/c$ and $\gamma = 1/\sqrt{1-\beta^2}$. Returning back to the laboratory frame we get:

$$E_2 = \gamma E_2'(1 + \beta \cos\theta_2'), \tag{5.3}$$

Because the scattering is collisionless, the magnetic field is tied to the cloud and the cloud is very massive, in the cloud's rest frame there is no change of energy $E_2' = E_1'$ and hence we obtain the fractional change in the laboratory frame :

$$\frac{E_2 - E_1}{E_1} = \frac{\Delta E}{E} = \frac{1 - \beta\cos\theta_1 + \beta\cos\theta_2' - \beta^2\cos\theta_1\cos\theta_2'}{1-\beta^2} - 1. \tag{5.4}$$

For the evaluation of the mean value of the energy value we need to obtain average values of $\cos\theta_1$ and $\cos\theta_2'$ (we will denote them as $\langle\cos\theta_1\rangle$ or $\langle\cos\theta_2'\rangle$). Inside the cloud, the cosmic ray direction is randomized after many scatterings:

$$\langle\cos\theta_2'\rangle = 0 \tag{5.5}$$

The average value of $\cos\theta_1$ depends on the rate at which cosmic rate collide with clouds at different angles. The rate of collision is proportional to th relative velocity between the cloud and the particle so that the probability P per unit solid angle Ω_1 of having a collision at angle θ_1 is proportional to $(v - V\ \cos\theta_1)$, where v is the velocity of the particle, and for the ultrarelativistic particles $v \simeq c$. Thus we can write:

$$\frac{\mathrm{d}P}{\mathrm{d}\Omega_1} \propto (1 - \beta cos\theta_1) \tag{5.6}$$

By integration we obtain:

$$\langle \cos\theta_1 \rangle = \int \frac{\cos\theta_1 \frac{\mathrm{d}P}{\mathrm{d}\Omega_1}\mathrm{d}\Omega_1}{\int \frac{\mathrm{d}P}{\mathrm{d}\Omega_1}\mathrm{d}\Omega_1} = -\frac{\beta}{3} \tag{5.7}$$

And finally giving for the mean energy change $\langle \Delta E \rangle$:

$$\frac{\langle \Delta E \rangle}{E} = \frac{1+\beta^2/3}{1-\beta^2} - 1 \simeq \frac{4}{3}\beta^2 \tag{5.8}$$

because $\beta \ll 1$.

As $\langle \Delta E \rangle / E \propto \beta^2$ must be positive, this process leads to energy gain, but because $\beta \ll 1$ the average energy gain is very small.

First Order Fermi Acceleration

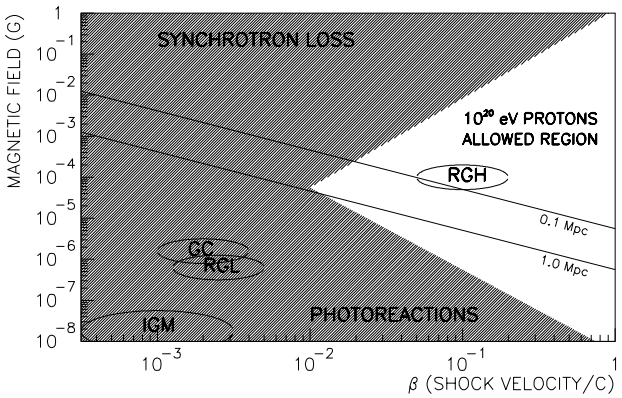

Figure 5.3: *Magnetic field strength and shock velocity of possible acceleration sites. GC refers to Galactic Cluster (accretion shocks), IGM to Inter Galactic medium, RGL to Radio Galaxy Lobes and RGH to Radio Galaxy Hot spots (subclass of RGL). From [7].*

Fermi's original theory modification was developed to the more effective acceleration (first order in β) taking place at supernova shocks but it is generally applicable to strong shocks in other astrophysical contexts. Our discussion of shock acceleration will be of necessity brief and omit a number of details. For simplicity we will consider the test particle approach, adopt a plane geometry and consider only non-relativistic shocks.

We will take the classic example of a SN shock, although the discussion applies equally to other shocks. During the supernova explosion several solar masses of

material is ejected at a speed of $\sim 10^4$ km.s^{-1} that is much faster than the speed of sound in the interstellar medium (ISM) which is ~ 10 km.s^{-1}. A strong shock wave propagates radially up in front of the supernova ejecta. The velocity of the shock V_S depends on the velocity of the ejecta V_P and on the ratio of specific heats κ through the compression ratio R:

$$\frac{V_S}{V_P} \simeq \frac{R}{R-1} \tag{5.9}$$

For SN shocks the SN will ionize the surrounding gas which will therefore be monoatomic ($\kappa = 5/3$) and the theory of the shock hydrodynamics than gives $R = 4$.

In order to work out the energy gain per shock crossing, we can imagine magnetic irregularities on both sides of the shock as clouds of magnetized plasma in Fermi's original theory. By considering the rate at which cosmic rays cross the shock from downstream to upstream, and upstream to downstream one finds that $\langle \cos\theta_1 \rangle = -2/3$ and $\langle \cos\theta_2' \rangle = 2/3$, giving:

$$\frac{\Delta}{E} \simeq \frac{4}{3}\beta \simeq \frac{4}{3}\frac{V_P}{c} \simeq \frac{4}{3}\frac{(R-1)}{R}\frac{V_S}{c} \tag{5.10}$$

Note that $\beta = V_P/c \propto \Delta E/E$, so basically β influences the resulting energy change in its first order, so the whole theory of Fermi shock acceleration and therefore is called the *first order* Fermi theory. We can conclude, that first order Fermi acceleration is much more efficient than previously discussed theory.

To obtain the energy spectrum we need to find out the probability of a cosmic ray encountering this shock once, twice, three times etc. We need to take into account the flow rate downstream and the flow rate upstream, and then to evaluate the probability of escape. From simple arguments which can be found e.g. in [81] we arrive to a power-law spectrum, where for the exponent Γ it holds:

$$\Gamma = 1 - \frac{\ln(1 - P_{escape})}{\ln(1 + \Delta E/E)} \approx \frac{R+2}{R-1}, \tag{5.11}$$

where P_{escape} is the probability of escaping from the shock. Hence we get for $R = 4$ to the differential spectrum Q of cosmic-ray acceleration:

$$Q(E) \propto E^{-\Gamma} = E^{-2} \tag{5.12}$$

The observed cosmic ray spectrum is generally steepened, what is in first approximation attributed to energy-dependent escape from the Galaxy.

5.1.2 Classical accelerators

Several surveys of possible accelerator sites were recently published, namely [75], [107], [31] and [77].

Origin in the vicinity of neutron stars in our Galaxy

The nearest suitable UHECR sources should be represented by neutron stars. These source type is not consistent with the assumption of extragalactic origin of UHECRs and have to explain the observed isotropic distribution[1] and no confinement with Galactic plane. One possible explanation will also be given in this work, actually in paragraph 6.2.3.

According to the presented "Hillas plot" the typical surface strength of magnetic field on young neutron stars is sufficient ($\sim 10^{13}G$) for the acceleration up to EHECR scale ($\approx 10^{20}eV$ for protons). However, the plasma that expands beyond the light cylinder is free from the main loss processes and may be accelerated to ultra-high energies. In particular, newly formed, rapidly rotating neutron stars may accelerate iron nuclei to ultra-high energies through relativistic magnetohydronamic (MHD) winds [21]. These Galactic sources need the enough efficient magnetic field to isotropize the directions of UHECRs, because no observable correlation with Galactic plane was found[2].

Origin in radio galaxy hot spots

The hot spots are interpreted as a gigantic shock waves emanating from from a central active galactic nucleus at relativistic speeds. Typical size of the hot spot is about few kiloparsec and the magnetic field within is several hundred μG. The maximum energy attainable is $(1-10)\times 10^{20}eV$, dependent on actual parameters of the spot. The acceleration is classically due to first order Fermi acceleration.

Origin in nearby galaxies

It is generally agreed that our Galaxy is producing cosmic rays up to 10^{18} eV, with a luminosity 10^{30} J.s^{-1}. for a confinement time 10^{11} s. It is possible that in more active galaxies [94], with higher rate of star formation, the magnetic field may be higher. The requirement for 10^{20} eV protons exceeds 3×10^{15} G.m (magnetic field $\times$ characteristic size). Acceleration to extremely high energies near the horizons of supermassive black holes in the galactic centers has also been suggested [24].

Origin in gamma ray bursts

According to some theories [102] gamma ray bursts (GRBs) may also be a source of ultra-high energy cosmic rays. Both phenomena have still unknown origins and also other similarities that may argue for a common source. UHECRs and GRBs are distributed isotropically, the average rate of γ-ray energy emitted by GRBs is comparable to the energy generation rate of UHECRs of energy $> 10^{19}$ eV

[1] See section 5.3.

[2] See section 5.3.

in a redshift independent cosmological distribution of sources, both have energy $\approx 10^{37}$ J.Mpc^{-3}.yr^{-1}.

But the recent observations of GRBs counterparts leads us to really cosmological distance of UHECRs and so the UHECR flux from the nearby GRBs (which are not so extremely losing initial energy during propagation[3]) is too low. Furthermore, this limitation to a "GZK sphere"[4] would change also the spatial distribution of the UHECRs, because such near GRB is expected to occur less than once over a period of 100 years. Extragalactic magnetic fields[5] are then generally expected to be too low to affect the trajectories of UHECRs significantly and so the final distribution will not be isotropic, but in a form of a "hot spot" (covering only a small fraction of the sky as a small spherical cap).

The general problem of all up to this point described processes is that the generated particles loss have the significant energy losses in the vicinity of all these discussed active environments. Maybe the most important loss channels are due to synchrotron radiation emissions and pair production in the dense surroundings of these objects.

5.1.3 "New physics" theories

Origin in interactions with neutrinos

The first "top-down" acceleration mechanism is represented by the neutrino — neutrino interactions. According to this scenario, the extreme energetic neutrino ($\sim 10^{22}$ eV) accelerated in any cosmologically distant source interacts with background relic neutrino (with temperature about 1.9 K) and produces Z^0 boson. The resonance energy for this energy is of about 4×10^{21} eV. This Z boson decays and produces ~ 2 nucleons, $\sim 20\gamma$-rays and ~ 50 neutrinos. "Z-bursts" are taking place in the relative vicinity ($\sim$ Mpc) to the Earth and we observe the arriving nucleons, which are products of Z decay.

Other possibility is that the cross-section of neutrino-nucleon interaction rises rapidly in the investigated energy region and this extreme energy neutrinos from the unknown cosmological sources are interacting directly with nucleons in the Earth's atmosphere [91].

Decay of relic superheavy particles

According to this theory cold dark matter in the galactic halo is supposed to contain a small admixture of long-lived superheavy particles with mass $> 10^{21}$ eV with a lifetime greater than the age of universe [15]. Such particles have to be created during reheating following the inflation or through the decay of hybrid

[3] See next section.

[4] Sphere with the 50 Mpc radius around the Earth.

[5] See next chapter.

topological defects[6]. The decay products are nucleons, electrons and photons, which are arriving to the Earth and initiating showers with common properties.

Origin in topological defects

Topological defects as monopoles, cosmic strings, superconducting strings should be also the sources of UHECRs [15]. These defects has to left from the phase transitions in the early universe. The UHECRs are originated during the collapse, the annihilation or the crossings of such formations.

New hadrons

The suggestion has also been made that new neutral particles containing gluino could be producing the trans-GZK events [38]. This particle have to be stable and with lower cross-sections for the interactions during propagation. Such a particles are called "uhecrons". Similarly vortons, superconducting cosmic strings stabilized by a current present a solution that is limited to the very highest energies.

Magnetic monopoles

The accelerated monopoles with mass $< 10^{10}$ GeV should be the sources of UHECRs too [79]. These monopoles should be accelerated in the Galactic magnetic field and then hit the Earth's atmosphere. But according to the simulations the produced showers then have to have special properties, which are not observed. Also the correlation with Galactic plane is not observed.

Violation of Lorentz symmetry

Last here presented idea is the possible departure from the strict Lorentz invariance [27]. The proposed departure is too small to be detected by the man-made accelerators, but large enough to affect the particle kinematics in ultra-high energy region and so to suppress or completely forbid the interactions of UHECRs with CMBR. Therefore the predicted cutoff in the spectrum is at least shifted by one order to higher energies and the origin of particles is possible also in the cosmological distances.

5.2 Propagation and Interactions

As we have noticed in section 1.3, during the search for the suitable source is very important also the distance of the investigated object. This fact is very important, because the UHECRs are efficiently lossing significant fraction of theirs

[6] See the next topic.

energy during propagation. For the range of ultra-high energies, the most important processes are pion photoproduction (affecting nucleons), Bethe-Heitler pair production and photodisentegration of nuclei.

The mean interaction length $x_{p\gamma}$ of a proton of energy E is given by [81]:

$$\frac{1}{x_{p\gamma}} = \frac{1}{8\beta E^2} \int_{\varepsilon_{min}(E)}^{\infty} \frac{n(\varepsilon)}{\varepsilon^2} \int_{s_{min}}^{s_{max}(\varepsilon,E)} \sigma(s)(s - m_p^2 c^4) \mathrm{d}s \mathrm{d}\varepsilon, \tag{5.13}$$

where $n(\varepsilon)$ is the differential photon number density of photons of energy ε, and $\sigma(s)$ is the appropriate total cross section for the process in question, for a centre of momentum (CM) frame energy squared s, which is given by:

$$s \ = m_p^2 c^4 + 2\varepsilon E(1 - \beta \cos\theta), \tag{5.14}$$

where θ is the angle between the directions of the proton and photon and βc is the proton's velocity.

For pion photoproduction (index π is for pion) we get:

$$s_{min} = (m_p c^2 + m_\pi c^2) \approx 1.16 \mathrm{GeV}^2 \tag{5.15}$$

and

$$\varepsilon_{min} = \frac{m_\pi c^2 (m_\pi c^2 + 2 m_p c^2)}{2E(1+\beta)} \approx \frac{m_\pi c^2 (m_\pi c^2 + 2 m_p c^2)}{4E} \tag{5.16}$$

For photon-pion pair-production the threshold is somewhat lower:

$$s_{min} = (m_p c^2 + 2 m_e c^2)^2 \approx 0.882 \mathrm{GeV}^2 \tag{5.17}$$

and

$$\varepsilon_{min} \approx \frac{m_e c^2 (m_e c^2 + m_p c^2)}{E} \tag{5.18}$$

For both processes is valid:

$$s_{max}(\varepsilon, E) = m_p^2 c^4 + 2\varepsilon E(1+\beta) \approx m_p^2 c^4 + 4\varepsilon E. \tag{5.19}$$

$s_{max(\varepsilon,E)}$ corresponds to a head-on collision of a proton of energy E and a photon of energy ε.

Examination of the integrand in equation 5.13 shows that the energy of the soft photon interacting with a proton of energy E is distributed as:

$$p(\varepsilon) = \frac{x_{p\gamma}(E) n(\varepsilon)}{8\beta E^2 \varepsilon^2} \Phi(s_{max}(\varepsilon, E)), \tag{5.20}$$

where in the range $\varepsilon_{min} \leq \varepsilon \leq \infty$ is valid:

$$\Phi(s_{max}) = \int_{s_{min}}^{s_{max}} \sigma(s)(s - m_p^2 c^4) \mathrm{d}s \tag{5.21}$$

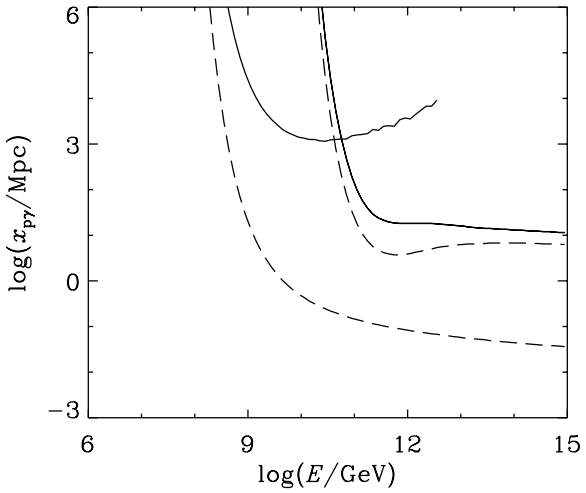

Figure 5.4: *Mean interaction length (dashed lines) and energy-loss distance (solid lines; $E/(dE/dx)$) for proton-photon pair-production (lower curves) and pion-production (higher curves) in the microwave background. From [81].*

Now we are able to derive the mean interaction length from equation (5.13). Dividing by the inelasticity $\kappa(E) = \Delta E/E$, one obtains the energy-loss distances for the two discussed processes:

$$\frac{E}{\mathrm{d}E/\mathrm{d}x} = \frac{x_{p\gamma}(E)}{\kappa(E)} \tag{5.22}$$

Numeric values for the mean interaction lengths and energy losses are shown on Fig. 5.4. Very illustrative is also the resulting dependence of the energy of proton on the travelled distance, which is showed in Fig. 5.5.

In the case of nuclei the situation is a little more complicated. The threshold condition for Bethe-Heitler pair production can be expressed as (γ is here given by $\gamma = E/A\ m_p c^2$):

$$\gamma > \frac{m_e c^2}{\varepsilon}\left(1 + \frac{m_e}{A m_p}\right), \tag{5.23}$$

and the threshold condition for pion photoproduction can be expressed as:

$$\gamma > \frac{m_\pi c^2}{2\varepsilon}\left(1 + \frac{m_\pi}{A m_p}\right), \tag{5.24}$$

where A is the atomic mass number. Because the gamma factor γ is divided by A in the case of nuclei against the case of proton, the pair production starts for nuclei in lower energy region.

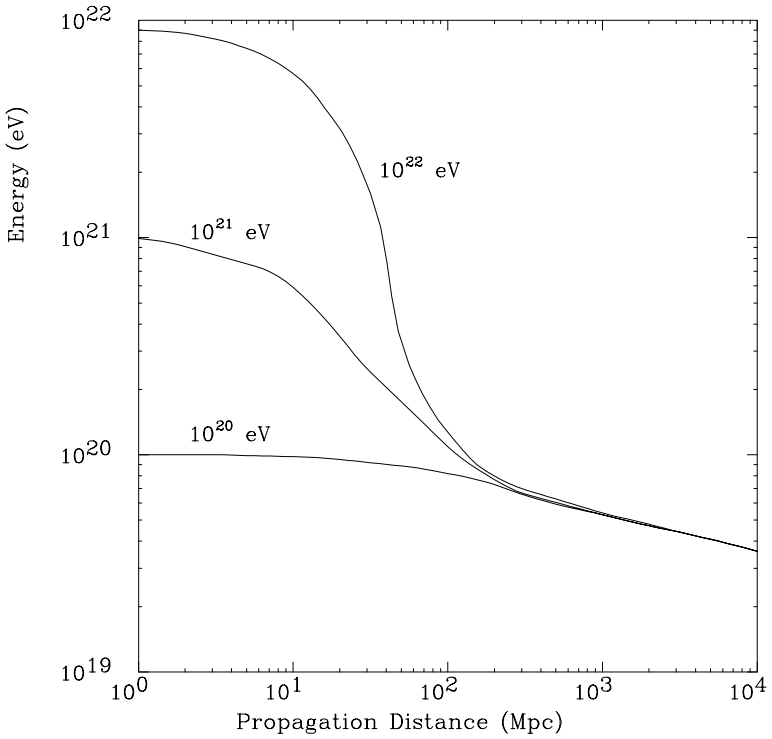

Figure 5.5: *Energy of a proton as a function of the propagation distance through the 2.7 K cosmic background radiation for various initial energies. The energy loss is computed only due to photopion production. From [7].*

The energy loss for the pair production by a nucleus in each collision near threshold is approximately $\Delta E \approx \gamma 2 m_e c^2$. Hence the inelasticity is

$$\kappa = \frac{\Delta E}{E} \approx \frac{2m_e}{Am_p}, \tag{5.25}$$

what is a factor of A lower than for protons. On the other hand, the cross section of each interaction rises by a factor Z^2, so the overall energy loss distance is for pair production reduced by a factor Z^2/A, e.g. for iron $26^2/56 \approx 12.1$.

For pion production the energy loss by a nucleus in each collision is given by $\Delta E \approx \gamma m_\pi c^2$, so the inelasticity is also lower by a factor A. However, the cross section in this case rises only as $A^{0.9}$ and the overall energy loss distance increases by a factor 1.5 for iron nuclei.

In the case of heavy nuclei (mass number A) we have to take into account also other important process — the photodisintegration (first evaluated in 1976 by [82]): $A+\gamma \to (A-1)+N$ or $\to (A-2)+2N$, where A is here for nuclei with mass number A and N for nucleon. The energy loss from photodisintegration is not

only due to CMBR photons but also due to photons from the IR background flux[7] The energy loss due to IR photons is only effective below 5×10^{19} eV, while the energy loss in interactions with microwave background dominates above 2×10^{20} eV [90].

The gamma photons are starving mainly through the pair creation in interactions with the CMBR. It takes place in the wide energy region above the threshold at 4×10^{14} eV: $\gamma + \gamma_{CMBR} \rightarrow e^+ + e^-$. Also in this case the attenuation due to IR background radiation is important, and becomes dominating above 2×10^{19} eV.

The last non-negligible effect arises from the omnipresent cosmological redshift. All particles lose energy due to the general expansion of the universe. The time scale over which a particle would suffer complete energy loss due to this effect is of the order

$$\tau_H = \left(\frac{1}{E} \frac{\mathrm{d}E}{dt} \right)^{-1} \approx H^{-1}, \tag{5.26}$$

where H is the Hubble constant. Then the constant $c\tau_H$ is representing the absolute upper limit on the distance a particle can travel before expiring. This limit and also the net effects for the attenuation lengths of protons, iron nuclei and photons is plotted in Fig. 5.6.

[7] Estimated empirically from the observations of 3000 galaxies in the IRAS catalogue.

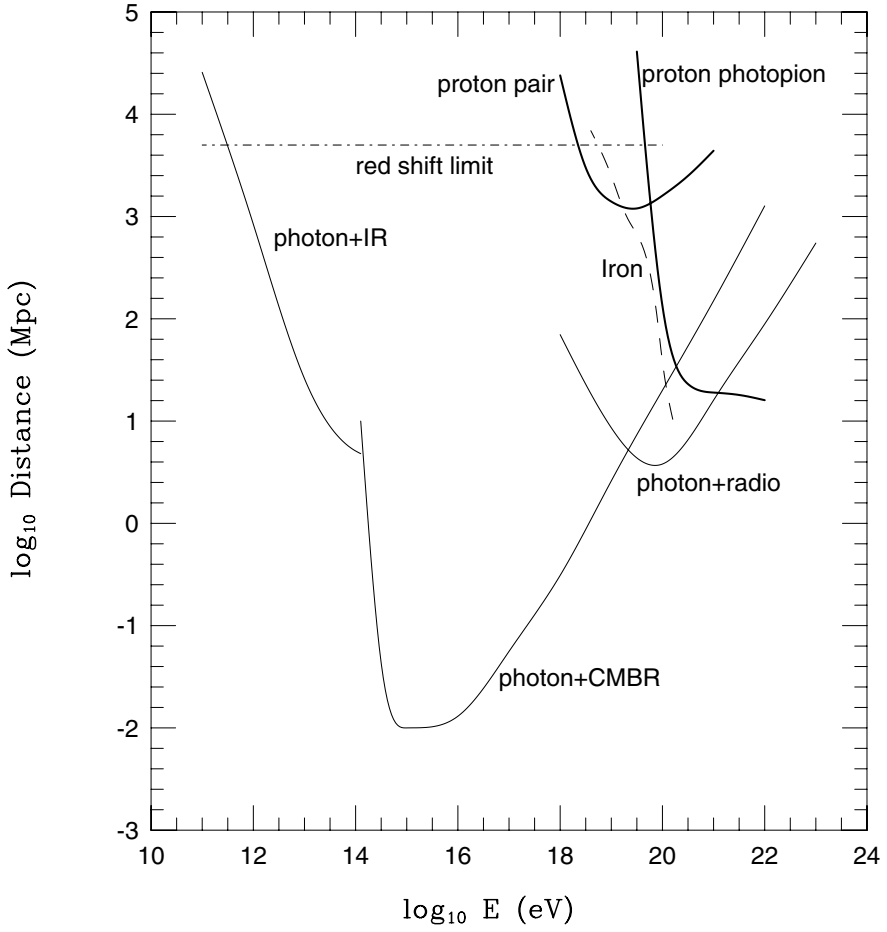

Figure 5.6: *Attenuation length of photons, protons and iron in various background radiations as a function of energy. Double pair production, which is not shown, limits the photon attenuation length to about 100 Mpc above* 10^{22} *eV. The dot-dashed line represents the absolute upper limit represents the absolute upper limit on the distance a particle can travel toward Earth, regardless of its initial energy. From [7].*

5.2.1 The GZK Cutoff

Different authors propose slightly different definitions of GZK cutoff. We will follow the classical definition described by [14] and its expansion by [107]:

The position of the GZK cutoff in CR spectrum is given by the decrease to one half of the expected flux. This expected flux is evaluated without accounting of all attenuation processes during the propagation of cosmic ray particle.

From this statement it is clear that position of the GZK cutoff is dependent on the type of CR and on our expectations about the not attenuated flux. Furthermore, our expectations about flux are up to now just hypothetical, because, as was discussed above, we still don't know the real source(s) of UHECRs. For example, for the Galactic source of UHECRs there is almost no cutoff at all, but for the different cosmological distributions of radio galaxies is the resulting GZK cutoff for protons is varying in the range $(5 \div 6) \times 10^{19}$ eV. The cutoffs for nuclei and photons are generally orderly lower, only neutrinos have this cutoff around 10^{22} eV.

So, the knowledge of actual cutoff value is not so necessary; more important is the knowledge of the energy losses and interaction lengths or cross-sections for the given acceleration process. Generally, under the statement "GZK cutoff" is understood the energy about $(5 \div 6) \times 10^{19}$ eV, the energy of proton cutoff with cosmologically distributed sources. As particles with energies provably above the GZK cutoff are obviously considered the particles with energies above 10^{20} eV (EHECRs).

5.3 Spatial Distribution of UHECRs

The essential importance for the discrimination of the real source(s) of UHECRs has their observed spatial distribution. Many analysis were done in the lower energy regions and are summarized in [101]. Because of the existence of the magnetic field, which effects will be discussed in detail in next chapter, the arrival directions are very accurately isotropic. The individual experiments are unable to observe the whole sky and so the analysis in the declination is rather without sense and so is the harmonic analysis in the right ascension applied. The method is to fit the observed distribution to a sine wave with period $2\pi/m$ (mth harmonic) and to derive the maximum amplitude and the phase of anisotropy.

Some signs of slight anisotropy were observed in the energy region, where the Larmor radius (equation 1.2) is growing above the kiloparsec order, above 10^{17} eV. In the data from Haverah Park was found the amplitude with an excess of about 2 % at right ascension $212° \pm 17°$ in energy region about 10^{17} eV. 1.4 % excess at the very different right ascension 123° in the energy region $3 \times 10^{16} - 3 \times 10^{17}$ eV in Yakutsk data. So, even in this regions, where the data volumes are very large (about millions of detected events around 10^{17} eV), the anisotropic analysis

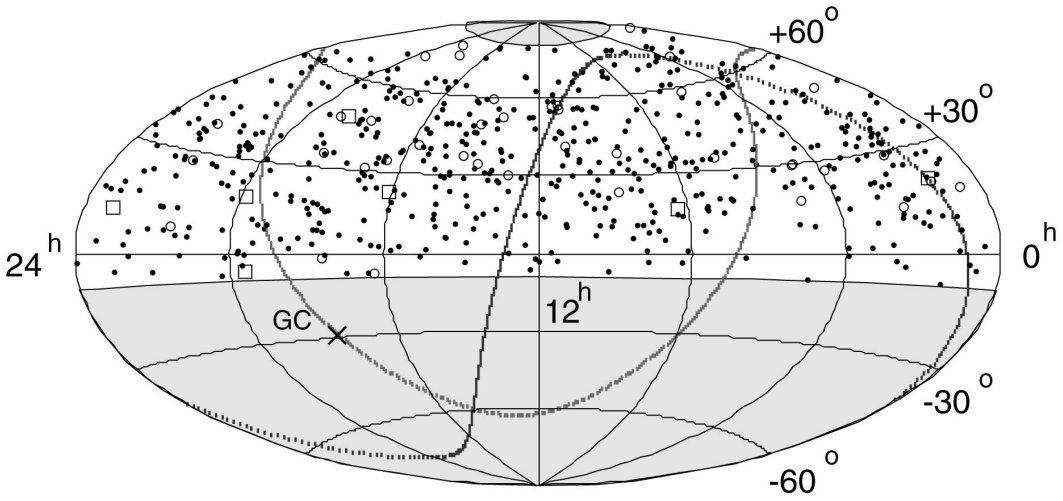

Figure 5.7: *AGASA arrival directions of cosmic rays with energies above* $10^{19.0}$ *in equatorial coordinates. Dots, open circles, and open squares represent cosmic rays with energies* $(1--4)\times 10^{19}eV$, $(4--10)\times 10^{19}$ eV *and* $\geq 10^{20}$ eV, *respectively. The Galactic and supergalactic planes are shown by the dotted curves, "GC" designates Galactic center — on the Galactic plane. From [96].*

is not very significant.

Other interesting sign of anisotropy was found in the AGASA data between $8\times 10^{17}-2\times 10^{18}$ eV (4.3×10^4 events), where the first harmonic amplitude of 4 % was found in the direction to the Galactic center and to anticenter.

As we have seen in chapter 4, the statistics in the UHECR region is very poor. Only about 200 detected particles should be analyzed. This analysis was done for several times. The first one [88] found the slight correlation with the direction of the supergalactic plane[8], the observed excess is $\sim 2.5-2.8\sigma$ in terms of Gaussian probabilities. This claim was challenged indirectly by [70], who found no correlation with the distribution of nearby galaxies with EGMF[9] taken into account. Also the very recent special analysis of the data from AGASA [96] found no correlation with supergalactic plane and no large-scale anisotropy at all. However, the small-angle clustering was found. Actually, one triplet and three doublets int the energy region above 4×10^{19} eV were found. This analysis was further expanded by [100], who used UHECR data from Volcano Ranch, Haverah Park, Yakutsk and AGASA (total number is 92 events). [100] found two triplets

[8]Defined by the higher concentration of bright galaxies in our local supercluster.

[9]Extragalactic magnetic field; see section 6.1.

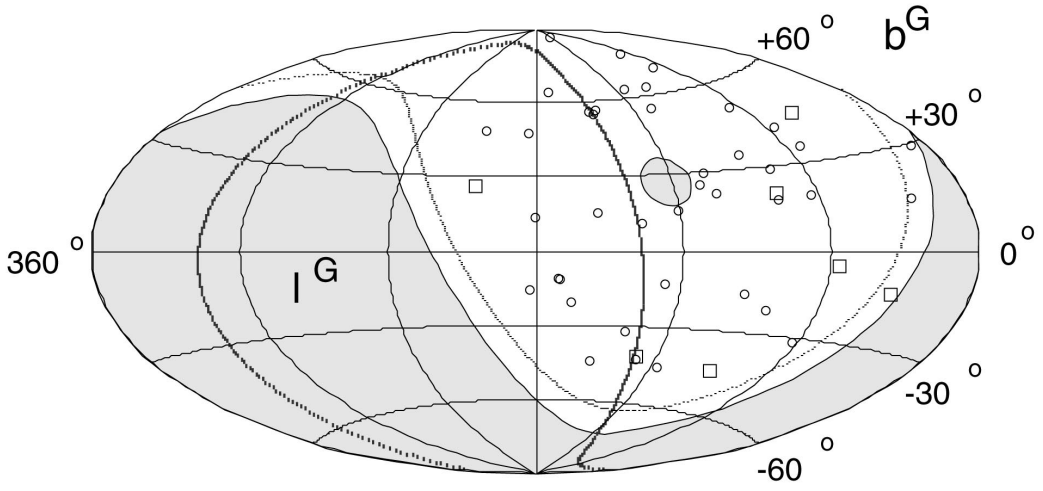

Figure 5.8: *The same as on Fig. 5.7, but in galactic coordinates and only for AGASA particles above* $4 \times 10^{19} eV$. *Also from [96].*

and twelve doublets (with space angle separation $< 3.0°$). Both triplets and eight doublets are within $\pm 10°$ from the supergalactic plane. The probability that this effect will be observed by chance is less than 1 %. However, the correlation with supergalactic plane should be not significant and the small angle clustering should be accounted to other set of point sources of UHECRs.

Generally, we are not able to discriminate between several point sources (in the extreme possibility one point sources) and isotropic distribution of many sources, mainly because of the influence of the magnetic fields onto trajectories of UHECRs, which should have the essential effect and is discussed in next chapter.

Chapter 6

Influence of Magnetic Fields

In this chapter the influence of the magnetic fields on the propagation of UHECRs will be discussed, especially with respect to the goal of backtracking their generation sites. The survey of contemporary knowledge about extragalactic and galactic fields will be put first and then the changes in some simulated and real UHECR distribution will be examined.

6.1 Extragalactic Magnetic Fields

While the first measurements of interstellar magnetic fields are older than a half of the century[1], the large-scale structures are still known very poorly. From the Faraday rotation measures of the extragalactic objects we are able to derive only the upper limits ([59] or [63]) for the field strengths. Actually, Faraday rotation measures from the distant powerful radio sources give $B\sqrt{l_c} < 10^{-9}$ G Mpc$^{1/2}$ for the intensity of magnetic field, where the l_c denotes the reversal length of the field. So any modelling of this field is just very speculative.

This pure experimental approach is quite often challenged by ambitious theoreticians, who expect some magnetic field anomalies in the form of (primordial) large-scale curved strings or planes [84], in which the magnetic field is reasonably stronger than the above mentioned upper limits — ranging from 10^{-6} G up to 10^{-3} G or the intensive magnetic field ($\sim 10^{-6}$ G) in very extensive galactic halo (reaching several Mpc) [47] or in the local galactic cluster [39] (with the same strength $\sim 10^{-6}$ G). These claims are further challenged by [32], giving a basic argument that the presence of such a strong magnetic field in the surroundings of our Galaxy would confine the bulk of cosmic rays for a time comparable to a Hubble time and turn the ratios of observed radioactive nuclei (Al^{26}/Al^{27} or Be^{10}/Be^{9}) in cosmic radiation into contradiction with observations. The case of intensive field in the large galactic halo will be also discussed in the next section.

[1] See next section for short survey of used methods of magnetic fields measurements in the Galaxy.

Generally, the magnetic field simulations are also limited by the fact that the mechanism of the origin of extragalactic field is still unknown. Up to now is not possible to decide whether these fields are generated by the local fields of the galaxies or whether they are primordial and were originated in some phase transitions shortly after big bang.

6.2 Galactic Magnetic Field (GMF)

The first evidence of the existence of a Galactic magnetic field was derived from the observation of linear polarization of starlight in 1949 [55]. Many new measurements were done since then using the Zeeman spectral-line splitting (gas clouds, central regions of the Galaxy), optical polarization data (large scale structures of the magnetic field in the local spiral arm) and Faraday rotation measurements in the radio continuum emission of pulsars and of extragalactic sources (maybe the most reliable method for the large scale structure, this method is used also for the determination of the global structure of the magnetic fields in the external galaxies). From these measurements it follows that the Galactic magnetic field has two components — regular and turbulent [83]. Random field appears to have a length scale $50 \div 150$ pc and so for the propagation of the UHECRs (with kiloparsec scale of the Larmor's radii) doesn't play the key role, but for the second generation models of the GMF it should be taken in account; one possibility of its implementation is showed in [61].

According to Beck [13] we are able to summarize our direct experimental knowledge about Galactic magnetic field into several statements:

- The strength of the total magnetic field in the Galaxy is $(6 \pm 2)\mu$G and about $(10 \pm 3)\mu$G at the 3 kpc from the Galactic center.
- The strength of the local regular field is $(4 \pm 1)\mu$G. This value is based on optical and synchrotron polarization measurements. Pulsar rotation measures give more conservative and approximately twice lower value. These rotation measures are probably underestimated due to anticorrelated fluctuations in regular field strength and in thermal electron intensity. On the other hand, optical and synchrotron polarization observations could be overestimated due to presence of anisotropic fields.
- The local regular field may be a part of a Galactic magnetic spiral arm, which lies between optical arms.
- The global structure of the Galactic field remains unknown.
- Existence of two reversals in the direction towards Galactic center was recently confirmed. The first reversal is lying between the local and Sagittarius arm, at ~ 0.6 kpc from the Sun, the second one is lying at ~ 3 kpc

from the Sun. Some of the Galactic reversals may be due to large-scale anisotropic field loops.

- As was expected from the beginning of the 90s and as it was recently confirmed too, the Galactic center region contains highly regular magnetic fields with strengths up to 1 mG. This extremely intensive field is concentrated in narrow bundles oriented perpendicularly to the Galactic plane. The characteristic length of this filament is about 450 pc.

- The local Galactic field is oriented mainly parallel to the plane, with a vertical component of only $B_z \simeq (0.2 \div 0.3)\mu$G, what agrees well with the results for other galaxies.

- The Galaxy is surrounded by a thick radio disk with a scale height of about 1.5 kpc, similar to that of edge-on spiral galaxies. The field strength in this thick disk is not known, but the global dipole field in the thick disk is also possible.

- The local Galactic field in the standard thin disk has an even symmetry with respect to the plane (it is a quadrupole). This is in the agreement with the galactic dynamo model, which is briefly discussed in the next paragraph.

Other facts, used in modelling of GMF, have indirect character — they are usually derived from observations of other spiral galaxies and of the structure of their magnetic fields or from existing proposals of the mechanisms of magnetic field generation. Generally it is expected, that the Galactic magnetic field encompasses the entire Galactic disk and shows some spiral structure. Further research and measurements have the vital importance not only for the observations of UHECRs, but for the whole cosmic-ray physics.

6.2.1 Global Models of GMF

The global models omit the presence of turbulent fields and are trying to model just its regular component. A basic, conservative model of global Galactic plane was established by Han & Qiao [44] in 1994, based on the Faraday-rotation measurements of 134 pulsars. Model consists of a two-arm logarithmic spiral model with the constant pitch angle[2] p and shows π symmetry, so it is bisymmetric

[2]The pitch angle determines the orientation of local regular magnetic field. Its sense is clear from Fig. 6.1. Precise definitions of pitch angle is not unique, in this work is used the definition proposed by [45]: The galactic azimuthal angle Θ is defined to be increasing in the direction of galactic rotation. Lograithmic spirals are then defined by:

$$R = R_0 e^{k\Theta}, \tag{6.1}$$

where R is the radial distance and R_0 is scale radius. The pitch angle is then $p = \arctan(k)$. This angle is negative for trailing spirals such as our Galaxy, where R increases with decreasing

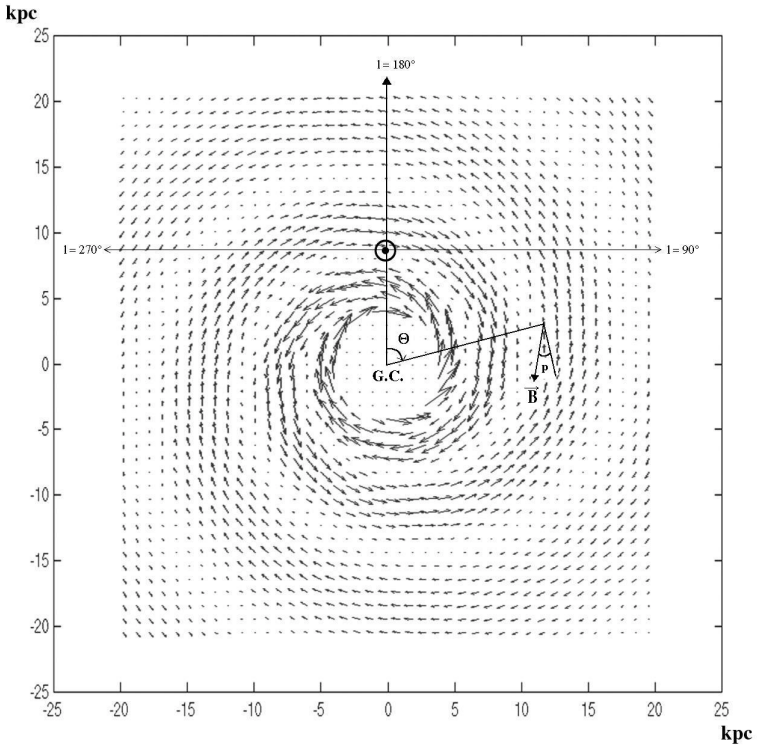

Figure 6.1: *Direction and strength of the regular magnetic field in the Galactic plane is represented by the length and direction of the arrows. The field inside the Galactocentric circle of radius 4 kpc is taken as constant, 6.4 μG. The model was constructed using parameters from [89] & [44] and is in detail described in text. From the figure the sense and orientation of the field and of the angles Θ & p is clear, too. G.C. denotes the Galactic centre (at $l = 0°$).*

(BSS) magnetic field model. More exactly, it has also a dipole character (it has field reversals and odd parity with respect to the Galactic plane), so it is assigned as the BSS-A model.

Discussed model employs cylindrical coordinates — the radial distance r, the position angle Θ and the vertical height z. The radial B_r and azimuthal B_Θ components at the plane position (r, θ) can be given by the following equations:

$$B_\Theta = B_0(r) \cos\left(\Theta - \beta \ln \frac{r}{r_0}\right), \cos p \tag{6.2}$$

$$B_r = B_0(r) \cos\left(\Theta - \beta \ln \frac{r}{r_0}\right), \sin p \tag{6.3}$$

azimuthal angle Θ. For our Galaxy, the Galactic angular momentum vector points toward the south Galactic pole, and Θ increases in a clockwise direction when viewed from the north Galactic pole.

where p denotes pitch angle and according to [89] is about $-10°$, $\beta = 1/\tan p \doteq -5.67$, r_0 is the Galactocentric distance of the maximum field strength at $l = 0°$ (in presented model it has a value $r_0 = 10.55$ kpc) and for $B_0(r)$ it holds:

$$B_0(r) = 3\frac{R}{r}, \tag{6.4}$$

where R is the Galactocentric distance of the Sun, taken as 8.5 kpc.

The vertical (z) component of the field is taken as zero in approximate agreement with observations. Results of this model are depicted on Fig. 6.1 and the orientation of the whole system is also clear from the figure.

The size and field strength in the Galactic halo is extremely important for the cosmic ray trajectories, but very poorly known, as we stated above. Recent approach to this problem is represented by the work of Stanev [89], where the field above and under the Galactic plane is taken as exponentially decaying:

$$|B(r, \Theta, z)| = |B(r, \Theta)|e^{(-z/z_0)}, \tag{6.5}$$

where $|B(r, \Theta)|$ is the vector sum of magnitudes of B_r B_Θ, with the $z_0 = 1$ kpc for $|z| < 0.5$ kpc and $z_0 = 4$ kpc for $|z| > 0.5$ kpc.

This model in its exact configuration was further used also in my computer simulation of the propagation of UHECRs in the GMF.

Alternative models with another field configurations were also proposed. The another possible but according to recent observations a bit less probable configuration is the so called ASS-S configuration, axisymmetric configuration without reversals and with even parity [89]. However, this configuration has one advantage — it could be much easier modeled using of the very popular dynamo model of magnetic field generation [36]. The bisymmetric mode is also realizable from dynamo model, but in sucha case the use of strong non-axisymmetric perturbations is necessary. The other two possibilities of magnetic field configurations — bisymmetric dipole type (BSS-S) and axisymmetric quadrupole type (ASS-A) are also not completely observationally excluded yet [12]. Furthermore, some models ([83]) employ third basically different type — magnetic field arranged in concentric rings, hence with pitch angle $p = 0°$. This model seems to be rather unprobable according to recent observations [13].

The dynamo model has one very interesting consequence for the propagation of CRs, that except of relatively flat field in the galactic disc it contains also quite strong toroidal fields above and under plane, which motions and their superpositions generates the net field in the Galaxy. The existence of a such field is indirectly supported by the existence of radio thick disc mentioned above in the review of observation results. Such a field has to change the CR trajectories quite essentially, but this type of models wasn't used for these purposes yet.

6.2.2 Propagation of UHECRs in Magnetic Fields

The propagation of the main part of UHECR candidates (nucleons, nuclei, electrons) is of course influenced by the magnetic fields. This influence is given simply by the well-known Lorentz force. For the acceleration $\vec{a}$ we then get:

$$\vec{a} = \frac{q}{m}(\vec{v} \times \vec{B}), \tag{6.6}$$

where q is the charge of particle, m is its relativistic mass, v its velocity[3] and B is the magnetic field strength.

Taking $\vec{B}$ as constant in suitable small volumes the trajectory of a particle could be followed and the resulting deflection should be examined. Some computer simulations also in the UHECR range were treated for this purposes recently and the effects especially on the changes in spatial distribution were studied.

The method of "antiparticle tracing" is used in all these models. The particle with opposite charge is injected to the model on the Earth position. Its initial velocity vector has spherical coordinates $\sim c, b, l$, where c is the velocity of the light and b and l are the galactic coordinates of the detected particle arrival. Because of the opposite charge such a particle traces back the trajectory of original detected particle. When such a particle leaves from the sphere of influence of Galactic magnetic field, we are able to evaluate its new galactic coordinates and so its initial direction before the entrance to GMF.

The first work is by Stanev [89] was published in 1997. It analyzes the motion of UHECRs in conservative models of BSS-A and ASS-S GMF with similar parameters as were given above in the paragraph 6.2. He examines the shifts for protons with energies ranging from 2 to 10×10^{19} eV. The second article is by Medina Tanco et al. [71] and was published in 1998. The particles with energy equal to 4×10^{19} eV are analyzed in this paper. The changes in regular distributions are followed for the ASS-S model of GMF and for the particles considered as protons or as Fe nuclei. The basic results of both models (magnitudes of deflections) are in the good agreement with the author's model discussed in the next section.

Other two works propose the large Galactic magnetic halo with very intensive fields.

First article was published by Ahn et al. in 1999 [4] and speculates about a large and intensive purely azimuthal magnetic field in the Galactic halo. This field should exist as a analogy to a solar wind and should extent to about 1.5 Mpc. In spherical coordinates r, θ, ϕ then holds

$$B_\phi = B_S R \frac{\sin\theta}{r}, \tag{6.7}$$

[3] Almost equal to velocity of light c; UHECRs are reaching the highest known relativistic γ-factors, about 10^{11}.

where $B_S R$ is the normalization factor derived from the values in the solar surroundings, which is equal to 70 μG.kpc. If such field is introduced, the positions of 11 of 13 EHECRs from Haverah Park, Volcano Ranch, Fly's Eye and AGASA should fall within 20° spherical cap around M87 position. This hypothesis was challenged shortly after its publication by Billoir & Letessier-Selvon [18]. They proved, that this (on the first sight) exciting fact, that M87 could be a single source of UHECRs is simply based on the fundamental property of used magnetic field model in halo. Used model of an azimuthal field is simply focusing all positions into the direction of Galactic north pole and M87 is lying near to this pole, and so the small angular distance between computed EHECR positions and between M87 is probably just an interesting consequence without fundamental physical importance.

The second work is [47] and proposes the Galactic magnetic wind extending to 1.5 Mpc and examines its focusing abilities.

Model of the magnetic wind used in this work gives is purely azimuthal:

$$B = B_7 \frac{r_0}{r} \sin\theta \tanh\left(\frac{r}{r_s}\right), \tag{6.8}$$

as a function of the radial spherical coordinate r and the angle to the north galactic pole θ. The distance from the Earth to the Galactic center is 8.5 kpc, factor r/r_s was introduced to smooth out the field at small radii (r_s was taken as 5 kpc). B_7 is the normalization factor (the strength of the field in [7μG]) and so in conservative models of GMF should be of about 0.3. As it is shown on the author's own combined Fig. 6.2, such a magnetic field has to clear out some fraction of the southern galactic hemisphere. But with the use of data from SUGAR, which are also plotted into this figure, we are able to show that a such model could not be completely correct, beacuse we are able to find several particles in the regions with proposed zero density.

Several works simulated also the influence of the extragalactic magnetic fields on the propagation of UHECRs. Some works (e.g. [63]) propose the possibility of study of EGMF using the analysis of arrival directions od UHECRs. [63] further treates the differences between burst and continous source models and the analyzes the resulting delay times after propagation in EGMF. [70] followed the trajectories of UHECRs from the known galaxy distribution between 20 and 200 Mpc, assuming that the luminous matter in the nearby universe is similar to the source distribution of UHECRs and intergalactic field is proportional to the the luminous matter density ($B_{IGMF} \propto \rho_{lum}^{0.3}$). The resulting spatial distribution should be tested by existing experiments in future.

6.2.3 Computer Model Results

The author of this work has created also its own model of the Galactic magnetic field. This model is very adaptive and was programmed in MATLAB en-

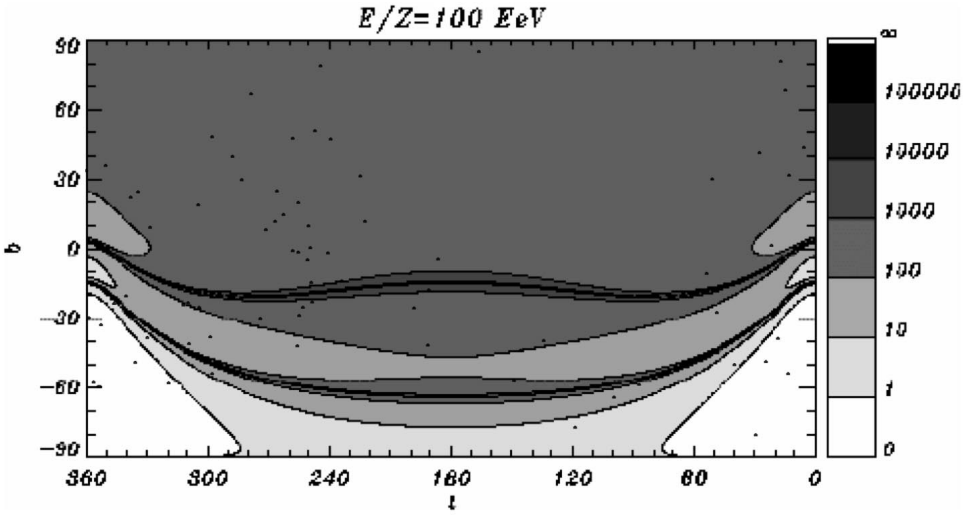

Figure 6.2: *Contour plots from [47] of the magnification by the galactic wind of the CR flux from a point source as a function of the arrival direction to the Earth for* $\bar{E} = 10^{20}$ *eV superposed with SUGAR coordinates of the arrivals of most energetic particles (*$\geq 4 \times 10^{19}$ *eV according to Hillas E model; for details see 3.2).* $\bar{E}$ *is given as* $\bar{E} = E/(ZB_7)$*, where* E *is the energy of the particle,* Z *is its charge and* B_7 *is normalization factor, what is equal to one, when the field strength* B *is 7* μG*. It is commonly expected, that* B_7 *should be* ~ 0.3*. This original figure reveals with quite high probability, that model of magnetic Galactic wind as described in [47] is not completely valid, because several SUGAR events are in the "zero field", so in the field where the magnetic magnification is zero, and where any particle should be swept away.*

vironment. It consists of three basic parts. Each of them should be easily and independently modified, so the model is prepared for the simulation of the propagation of various different datasets in the various magnetic fields. First part of program prepares or processes the initial datasets[4], records the computed data and shows the results in the maps. The second part computes the Lorentz force in the given point and is responsible for the evaluation of motion equations. This second part is in each step asking for the appropriate magnetic field to the third part of program, which is simulating the modelled magnetic field.

Up to now, particle motions in only the two various magnetic fields were analyzed. The basic and detailed simulation was done for the conservative Galactic magnetic field model by [44], which was discussed above. The complete survey of results is given in the Appendix A. Here we will analyze only the most interesting

[4]Generally was used the regular grid distribution, simulated isotropic distribution and real data from several experiments — from the catalogue in the chapter 4.

results.

Three types of initial data were used — the points with threshold UHECR energy ($4\times10^{19}eV$) distributed on the regular grid, then the points once more with same energy distributed isotropically and finally the real data[5] from catalogues in chapter 4. This third type was distributed into four categories — EHECR data, data from AGASA experiment, data from SUGAR experiment and combination of all these three datasets. Each such type was considered as three variants of cosmic-ray particles with different charges. We propagate these particles through Galactic magnetic field as protons (proton number $Z = 1$), oxygen nuclei ($Z = 8$) and iron nuclei ($Z = 26$). All particles were traced back outside from the influence Galactic field, actually the total travelled distance of each particle was 40 kpc for these simulations. The resulting final distance from the Earth varies only slightly for protons — from 39.8 to 40 kpc, more significantly for oxygen nuclei — from 18 to 40 kpc, and very substantially for iron nuclei — from 1 kpc to 40 kpc.[6]. This single statement makes it clear that the influence of GMF onto protons is only gentle, but the iron nuclei are almost confined in the Galaxy.

We shall also try to analyze the above-discussed possibility, that UHECR particles originate as iron nuclei in the (center of) our Galaxy, so we change the model parameters and trace the particles to the distance 8.5 kpc from the Earth, independently on the total distance travelled. The results from this special model are also shown in Appendix A.

The program results were displayed not only in maps, but were also written in tables, which are available by the author and which were further analysed. Some basic and further discussed results are shown in maps directly below:

[5]The arrival direction (b, l) and energy E was used for each detected particle.

[6]So the captions above the resulting maps are just rough simplifications.

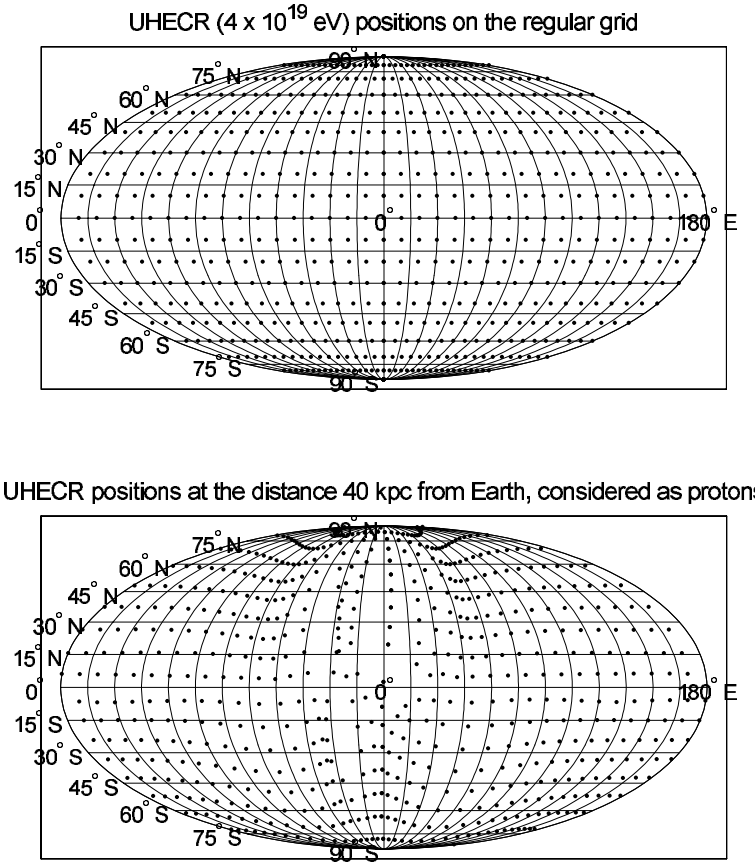

Figure 6.3: *Initial and final position of protons. On the upper part of the figure particles are regularly distributed on the* $10° \times 10°$ *grid, so the propagation of 703 particles were simulated. The angular shifts of individual particles are ranging from 0.2° to* $20°$.

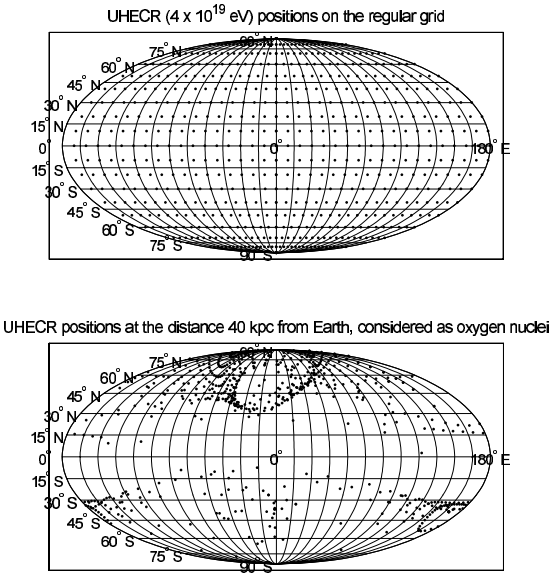

Figure 6.4: *Initial and final position of oxygen nuclei. On the upper part of the figure particles are regularly distributed on the* $10° \times 10°$ *grid, so the propagation of 703 particles were simulated. The angular shifts of individual particles are ranging from 1° to* $170°$.

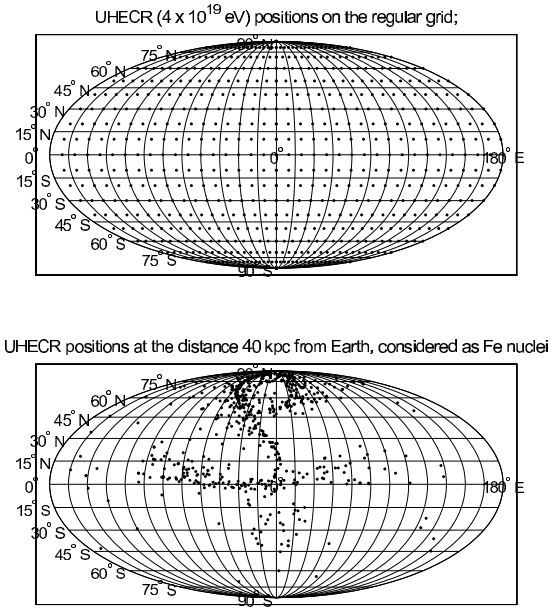

Figure 6.5: *Initial and final position of iron nuclei. On the upper part of the figure particles are regularly distributed on the* $10° \times 10°$ *grid, so the propagation of 703 particles were simulated. The angular shifts of individual particles are ranging from 1° to* $165°$.

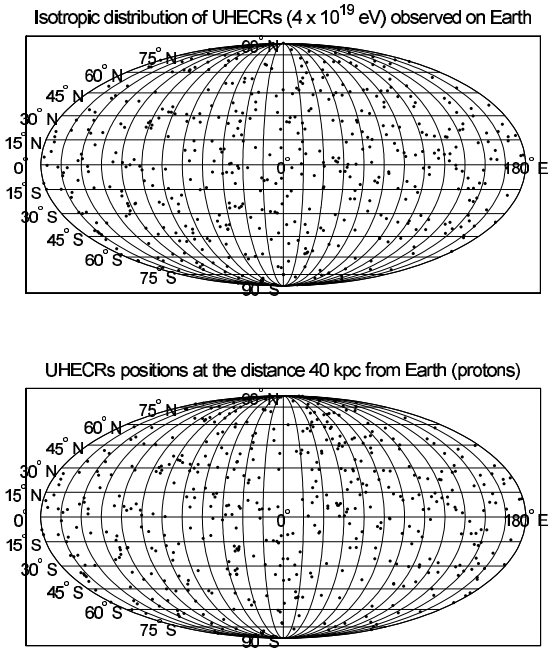

Figure 6.6: *Initial and final position of protons. On the upper part of the figure the isotropic distribution of 500 particles was simulated. The angular shifts of individual particles are ranging from 0.2° to* 22°.

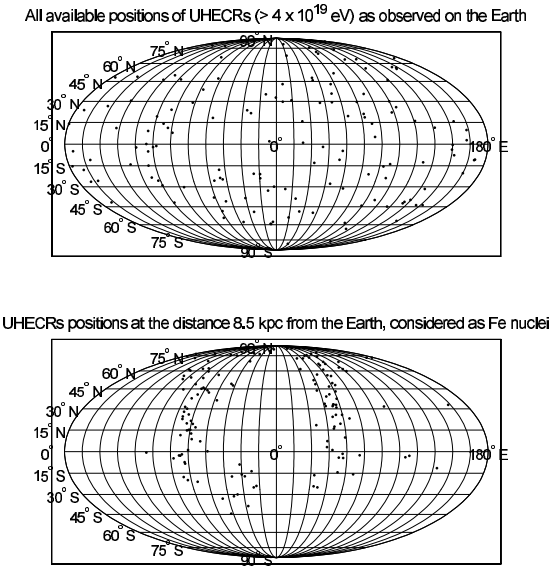

Figure 6.7: *Initial and final position of iron nuclei. On the upper part of the figure the original arrival directions of 145 UHECRs are shown. Particles were propagated to the distance 8.5 kpc from the Earth. The angular shifts of individual particles are ranging from 2° to* 150°.

We are able to say that the given deflection ranges are in the good agreement with previous models ([89] and [71]) of propagation of UHECRs through the Galactic magnetic field. So we also can formulate the following conclusions:

- The global structure of GMF is still unknown, but we can surely claim that its influence is non-negligible even also for protons and essential for Fe nuclei.
- The simulations of particles with higher charges (oxygen and iron nuclei) are transforming the isotropic distribution to structures, which show some regularities. The actual forms of these regular structures are rather unprecise, because of unprecise model of GMF, but their existence seems to be quite sure and is independent on the specific parameters of given model.[7]
- GMF is very important also for protons, because it is able to affect the small-angle clustering (as can be seen on Fig. 6.6, some initial small cluster were transformed into other ones). Small-angle clustering is today lively discussed and it is one of key features in discrimination between some theories of sources.
- The possibility that the UHECRs originate in the Galaxy (e.g. near the young neutron stars in the form of iron nuclei) is surely not excluded (see Fig. 6.7). Furthermore, these UHECRs should originate only in several point sources in our Galaxy, what is supported also by the existence of regular structures after propagation in the GMF.

This last information should also be combined (and should be used for further support of the theory of Galactic origin of UHECRs) with the asbove mentioned fact, that also relatively strong ($\sim$ 1 mG) fields exist in the form of filaments near Galactic center. In such a field Larmor radius is only about 4 pc. We also tried to model such a field and to observe its influence on iron nuclei.

In our first rough model we use the data[8] from [13]. Our model field has only a component which is perpendicular to the Galactic plane, what is in quite good accordance with observations. We expect, that the field is almost constant inside the cylinder with the length of 300 pc and with a diameter of 10 pc. Outside of this cylinder the field is exponentially decaying. The appropriate equation in cylindrical coordinates (r, Θ, z) is:

$$B_z(r,z) = 10^{-3}\frac{1-0.1z_a}{300\ \mathrm{pc}}\frac{1-0.1r_a}{10\ \mathrm{pc}}e^{\frac{-(|z|-300\ \mathrm{pc})}{z_b}}e^{\frac{-(|r|-10\ \mathrm{pc})}{r_b}}, \qquad (6.9)$$

[7] Of course, this is not excluding the possibility that also the initial directions before entering into the Galaxy are isotropic. The statement is true only in one way — the observed isotropic distribution doesn't necessarily require the initial isotropic distribution for oxygen and iron nuclei.

[8] Field strength, length and diameter of the filament.

where $z_a = z$ and $z_b \to \infty$ for $|z| < 300$ pc or $z_a = z_b = 300$ pc for $z \geq 300$ pc, and where $r_a = r$ and $r_b \to \infty$ for $r < 10$ pc or $r_a = r_b = 10$ pc for $r \geq 10$ pc.

Results of this model are shown on Figure 6.8. It was found that the particles which are not travelling in the narrow cone along the axis of the jet (filament), are strongly confined by this field. Such particles are spiralling perpendicularly to the vector $\vec{B}$ of the field and could not escape this field for a time many orders longer than is the chracteristic time of the propagation of CR through the distance of similar size. So, we simulated only the particles within discussed narrow cone and also these were quite finely isotropized by this field. In combination with regular GMF such a field is surely available to isotropize cosmic rays from the initial point source[9].

Observed system of such filaments will have important influence also on the other type of charged cosmic ray particles (as oxygen nuclei or protons). This is maybe the main direction of the author's future endeavour on this field.

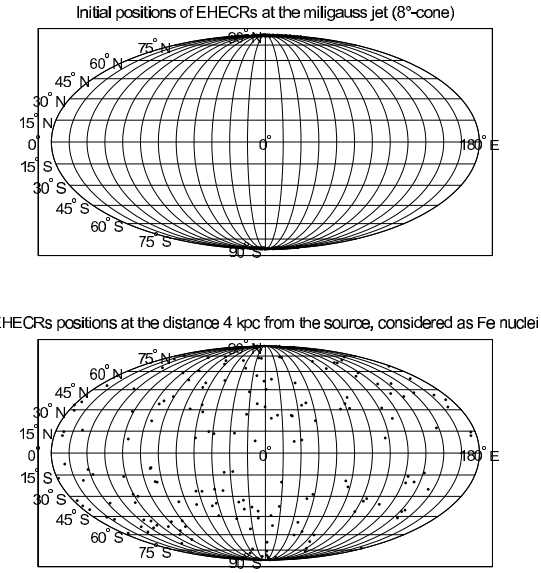

Figure 6.8: *Initial and final position of iron nuclei. On the upper part of the figure 200 particles collimated in the narrow cone (with apex angle* 8°*) are shown. Particles were propagated to the distance 4 kpc from the filament center. The angular shifts of individual particles ar ranging from* 1° *to* 80°*.*

[9] Only one source in extreme case is also possible.

Chapter 7

Conclusions

The basics of the whole physics of cosmic rays with ultra-high energies are given in this work. The detection methods and both existing and proposed detectors are discussed, unique and up to date catalogue of EHECR and UHECR events are compiled. The survey of possible generation mechanisms of UHECRs and the survey of interactions during propagation are included into the thesis, too as well as the discusssion of observed UHECR spatial distribution.

The importance of magnetic fields is stressed, the actual state of our knowledge in this branch is reviewed. In this consequence, the a new program for modelling of various magnetic fields was constructed.

Some new results (see section 6.2.3) were obtained from the author's model of the Galactic magnetic field and from a simple model of the magnetic filament perpendicular to the Galactic plane. The most important conclusions from this modelling are that Galactic origin of UHECRs (iron nuclei) is possible (and probable) and that the Galactic magnetic field influences also the small-angle clustering of cosmic ray protons.

Author is very grateful that he had a chance to work on such fascinating and rapidly developing theme. He hopes that he will be able to enlarge and analyze this subject at full length in his further work.

Appendix A

Results of Computer Modelling

Table A.1: Complete table of properties of model results. *Fig. No.* is the number of the appropriate figure, N is the number of simulated particles in the given setup. *Data source* are divided into three types — simulated regular grid ($10° \times 10°$) distribution, simulated isotropic distribution and measured data from real detectors. EHECRs is for the particles $E > 10^{20} eV$, AGASA is for the data from the Akeno Giant Air Shower Array, SUGAR for the data from the Sydney University Giant ARray and UHECRs for the combined data from these three real datasets. Last figure is simulating the propagation of iron nuclei in the strong ~ 1 mG magnetic field near the Galactic center, the initial positions were inside of a cone with apex angle 8° (see section 6.2.3 for further discussion). *Travelled distance* is for the total travelled distance of all particles, *Final distance* shows the range of final distances of particles from the Earth, *Angular shift* shows the range for the angular shift of positions of propagated particles.

Fig. No.	N	Data source	Particle type	Travelled distance	Final distance	Angular shift	Note
1	703	regular grid	protons	40 kpc	39.7 – 40 kpc	$0.2° - 20°$	
2	703	regular grid	oxygen	40 kpc	11 – 40 kpc	$0.3° - 155°$	
3	703	regular grid	iron	40 kpc	1.5 – 40 kpc	$1° - 176°$	
4	500	isotropic	protons	40 kpc	39.8 – 40 kpc	$0.3° - 20°$	
5	500	isotropic	oxygen	40 kpc	18 – 40 kpc	$2° - 170°$	
6	500	isotropic	iron	40 kpc	1 – 40 kpc	$1° - 165°$	
7	23	EHECRs	protons	40 kpc	40 kpc	$0.6° - 3.8°$	
8	23	EHECRs	oxygen	40 kpc	39.4 – 40 kpc	$5° - 32°$	
9	23	EHECRs	iron	40 kpc	18 – 40 kpc	$9° - 108°$	
10	58	AGASA	protons	40 kpc	39.9 – 40 kpc	$1° - 13°$	
11	58	AGASA	oxygen	40 kpc	35.5 – 40 kpc	$2° - 95°$	
12	58	AGASA	iron	40 kpc	8 – 40 kpc	$3° - 138°$	
13	80	SUGAR	protons	40 kpc	40 kpc	$0.5° - 13°$	
14	80	SUGAR	oxygen	40 kpc	26 – 40 kpc	$2° - 170°$	
15	80	SUGAR	iron	40 kpc	3 – 40 kpc	$4° - 160°$	
16	145	UHECRs	protons	40 kpc	39.9 – 40 kpc	$0.5° - 13°$	
17	145	UHECRs	oxygen	40 kpc	26 – 40 kpc	$2° - 170°$	
18	145	UHECRs	iron	40 kpc	3 – 40 kpc	$3° - 160°$	
19	145	UHECRs	iron	?	8.5 kpc	$2° - 150°$	special
20	200	8°-cone	iron	?	4 kpc	$1° - 80°$	special

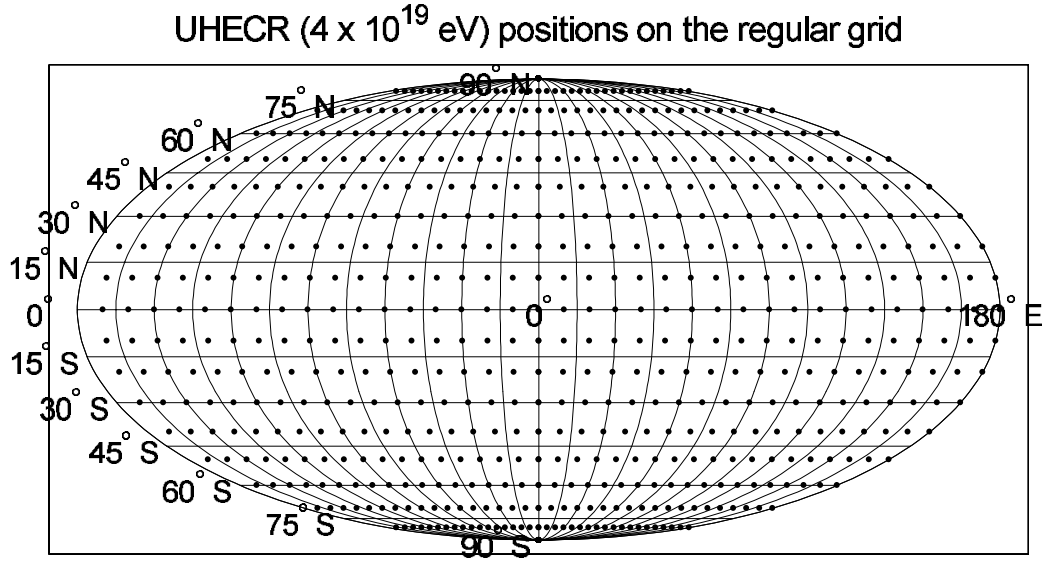
UHECR (4 x 10^19 eV) positions on the regular grid
90° N
75° N
60° N
45° N
30° N
15° N
0°
15° S
30° S
45° S
60° S
75° S
90° S
0°
180° E

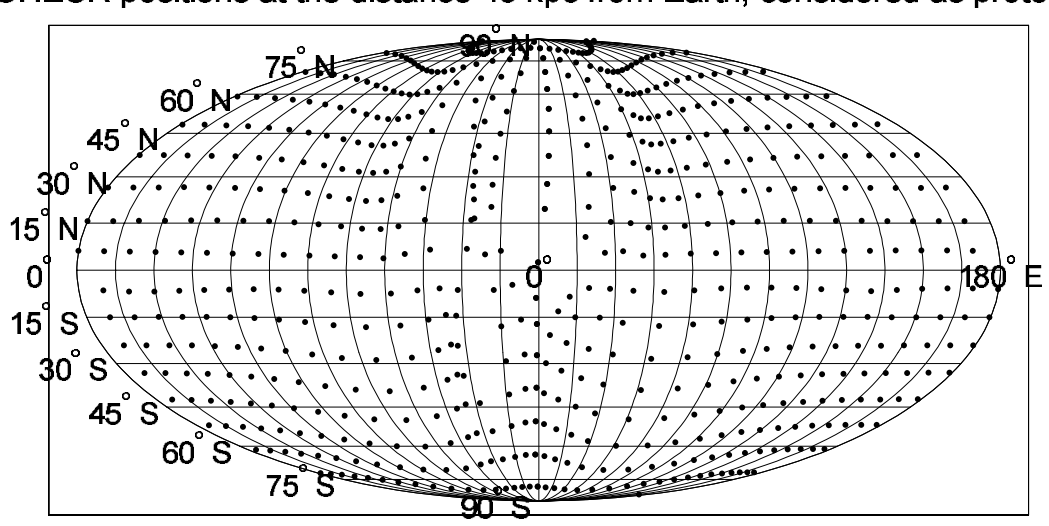
UHECR positions at the distance 40 kpc from Earth, considered as protons
90° N
75° N
60° N
45° N
30° N
15° N
0°
15° S
30° S
45° S
60° S
75° S
90° S
0°
180° E

Figure A.1:

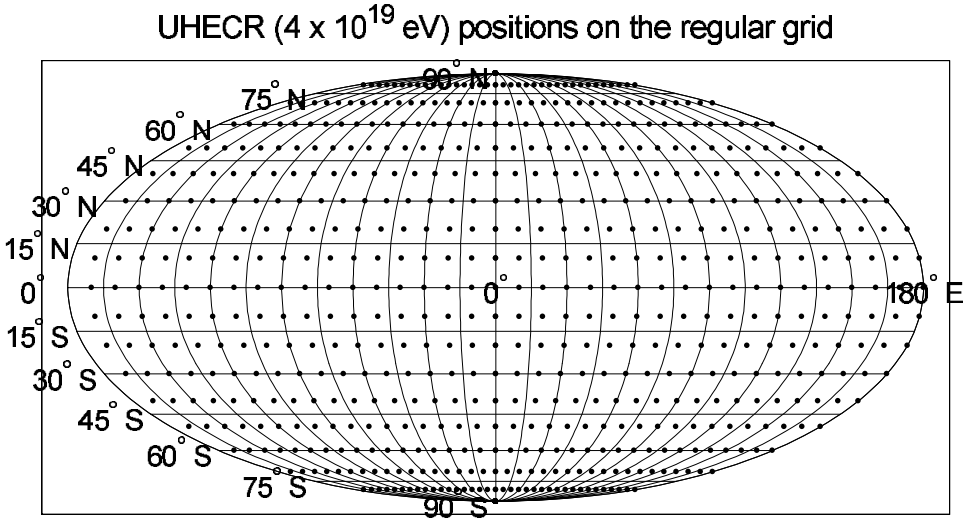
UHECR (4 x 10^19 eV) positions on the regular grid
90° N
75° N
60° N
45° N
30° N
15° N
0°
15° S
30° S
45° S
60° S
75° S
90° S
0°
180° E

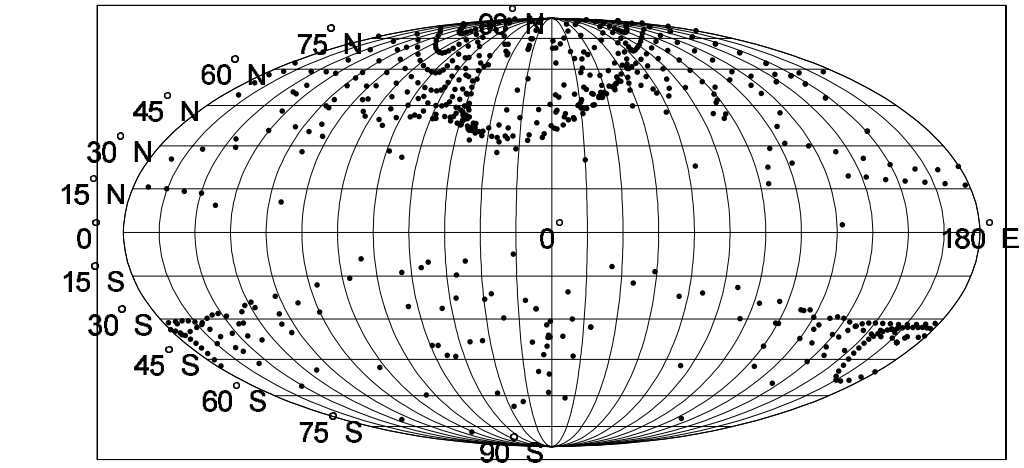
UHECR positions at the distance 40 kpc from Earth, considered as oxygen nuclei
90° N
75° N
60° N
45° N
30° N
15° N
0°
15° S
30° S
45° S
60° S
75° S
90° S
0°
180° E

Figure A.2:

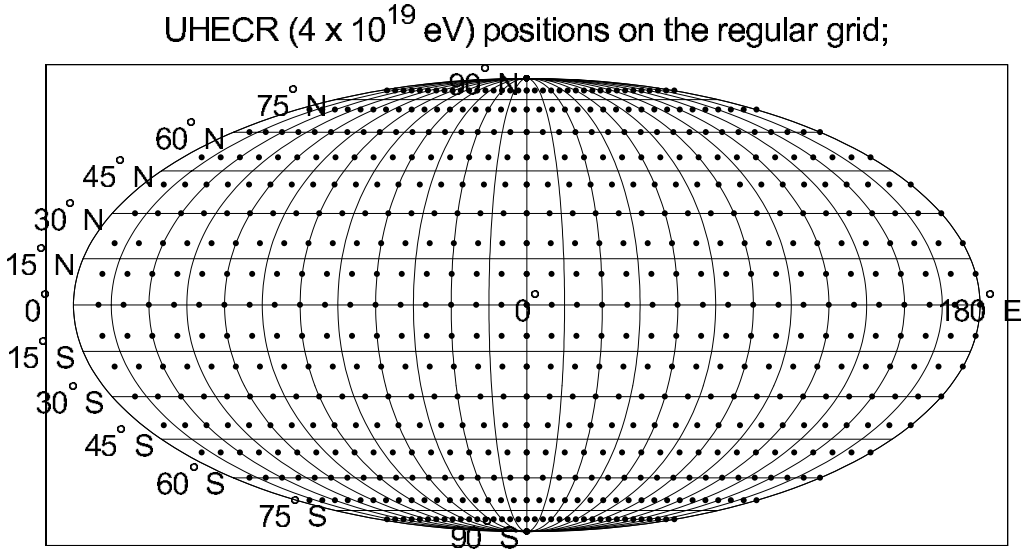
UHECR (4 x 10^19 eV) positions on the regular grid;
90° N
75° N
60° N
45° N
30° N
15° N
0°
15° S
30° S
45° S
60° S
75° S
90° S
0°
180° E

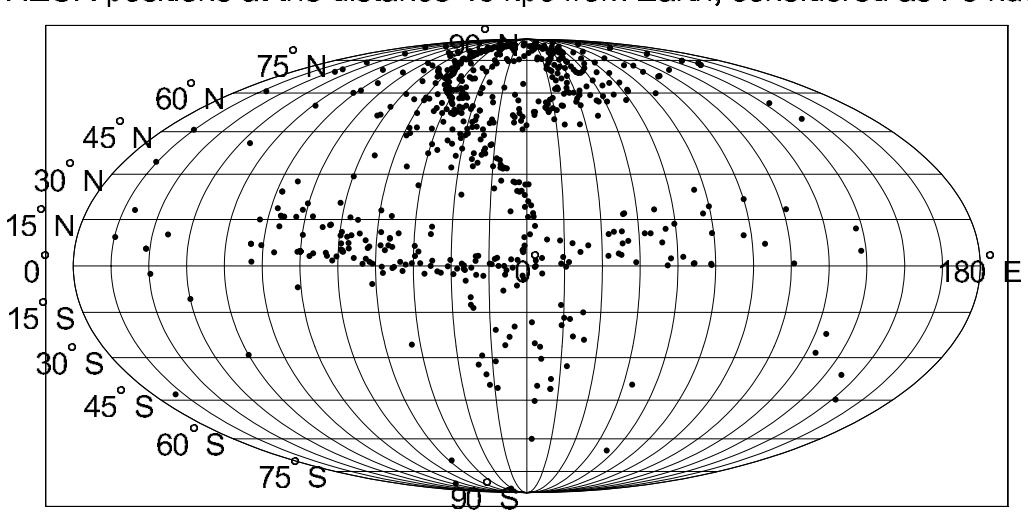
UHECR positions at the distance 40 kpc from Earth, considered as Fe nuclei
90° N
75° N
60° N
45° N
30° N
15° N
0°
15° S
30° S
45° S
60° S
75° S
90° S
0°
180° E

Figure A.3:

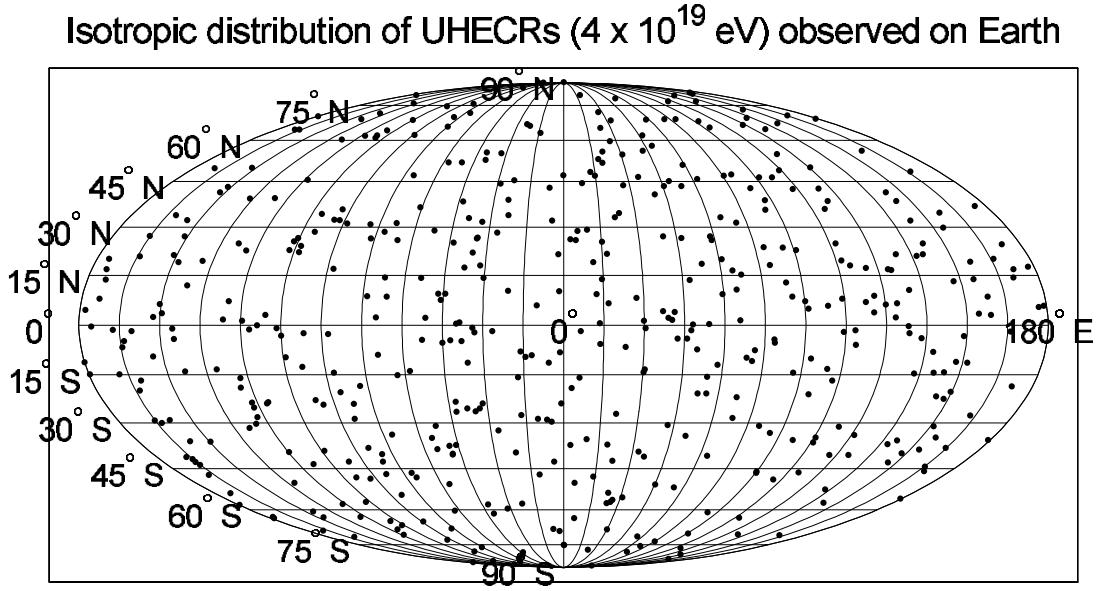
Isotropic distribution of UHECRs (4 x 10^19 eV) observed on Earth
90° N
75° N
60° N
45° N
30° N
15° N
0°
15° S
30° S
45° S
60° S
75° S
90° S
0°
180° E

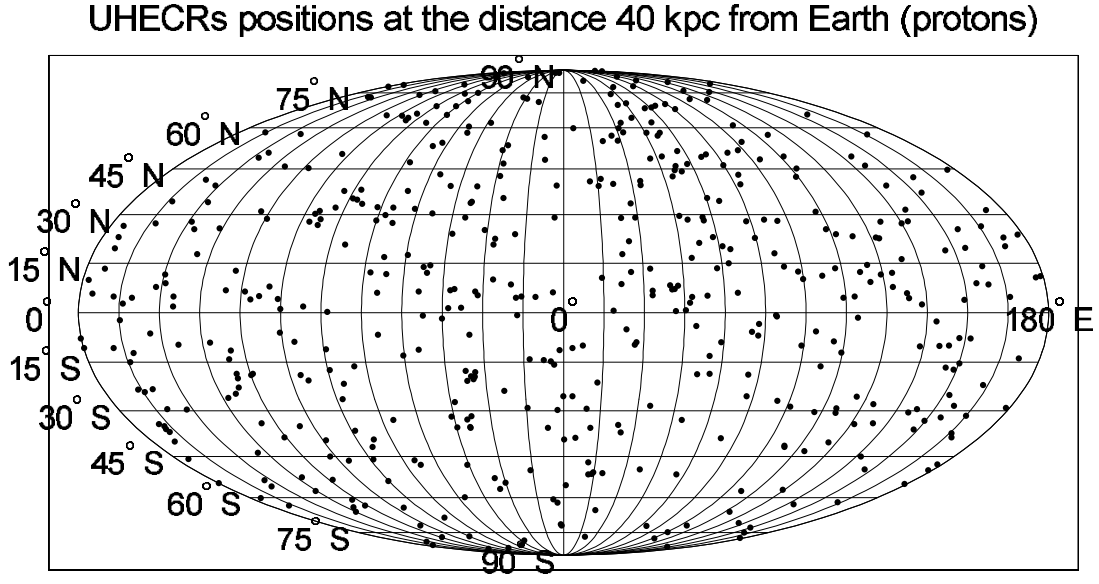
UHECRs positions at the distance 40 kpc from Earth (protons)
90° N
75° N
60° N
45° N
30° N
15° N
0°
15° S
30° S
45° S
60° S
75° S
90° S
0°
180° E

Figure A.4:

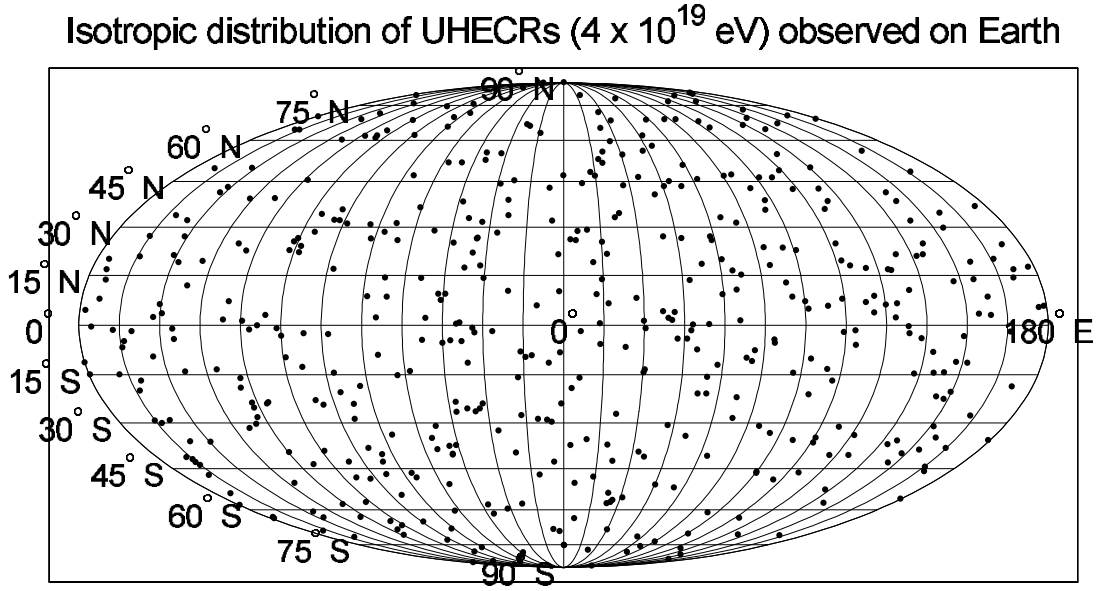
Isotropic distribution of UHECRs (4 x 10^19 eV) observed on Earth
90° N
75° N
60° N
45° N
30° N
15° N
0°
15° S
30° S
45° S
60° S
75° S
90° S
0°
180° E

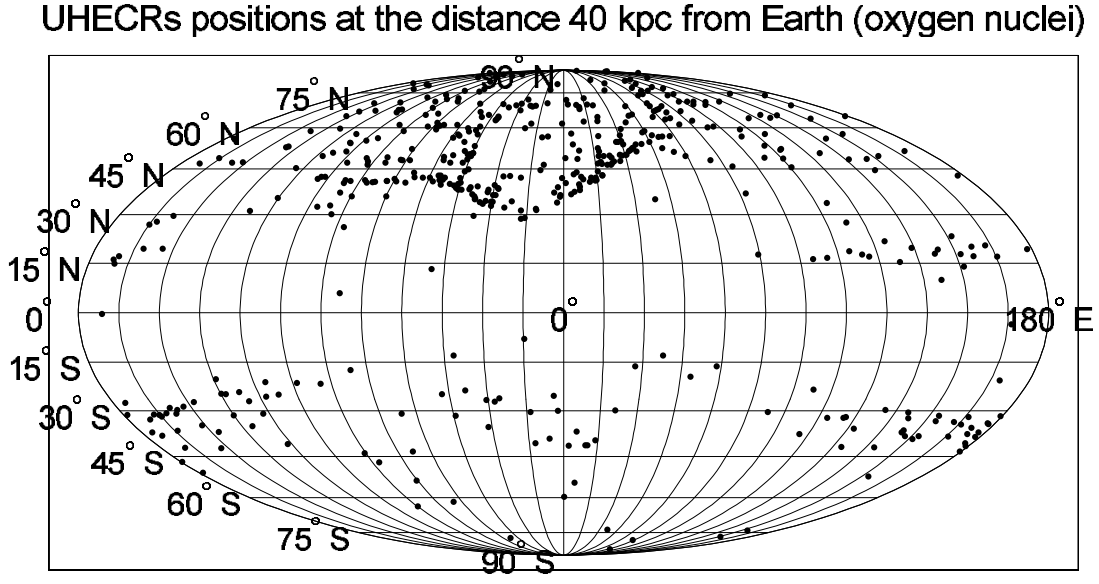
UHECRs positions at the distance 40 kpc from Earth (oxygen nuclei)
90° N
75° N
60° N
45° N
30° N
15° N
0°
15° S
30° S
45° S
60° S
75° S
90° S
0°
180° E

Figure A.5:

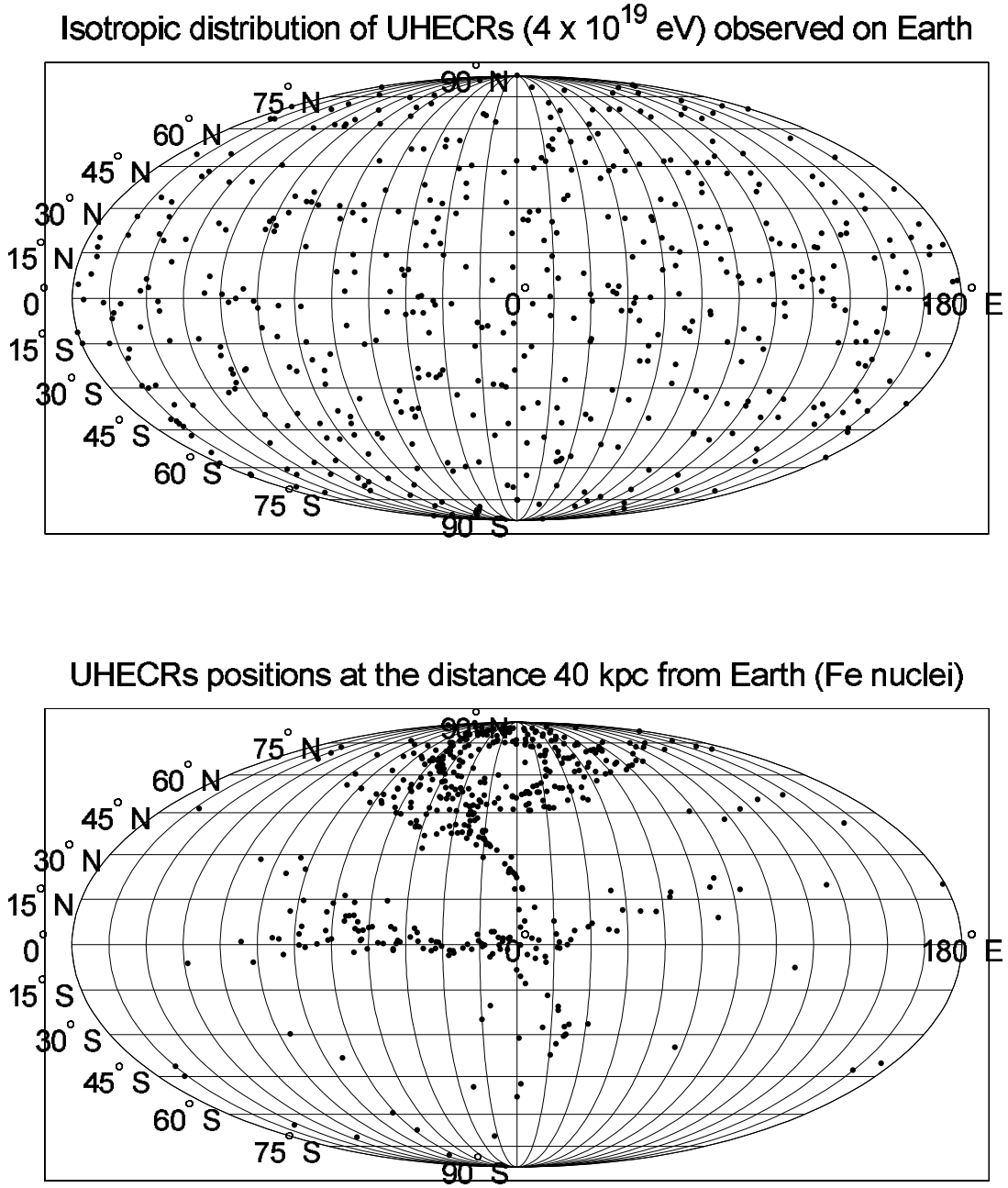
Isotropic distribution of UHECRs (4 x 10^19 eV) observed on Earth
90° N
75° N
60° N
45° N
30° N
15° N
0°
15° S
30° S
45° S
60° S
75° S
90° S
0°
180° E
UHECRs positions at the distance 40 kpc from Earth (Fe nuclei)
75° N
60° N
45° N
30° N
15° N
0°
15° S
30° S
45° S
60° S
75° S
90° S
0°
180° E

Figure A.6:

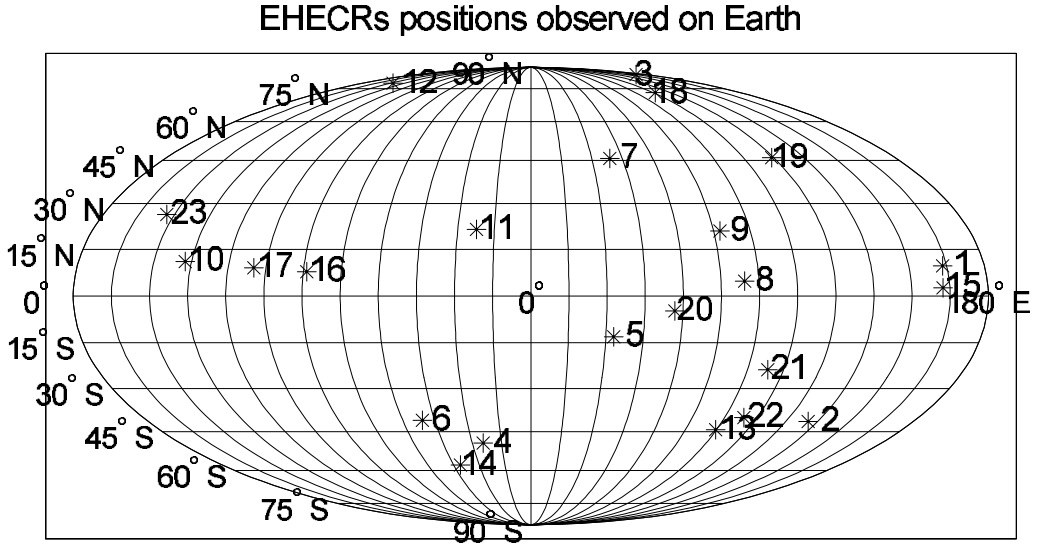
EHECRs positions observed on Earth
90° N
75° N
60° N
45° N
30° N
15° N
0°
15° S
30° S
45° S
60° S
75° S
90° S
180° E
12
3
18
7
19
23
11
9
10
17
16
1
15
8
0°
20
5
21
6
22
2
13
4
14

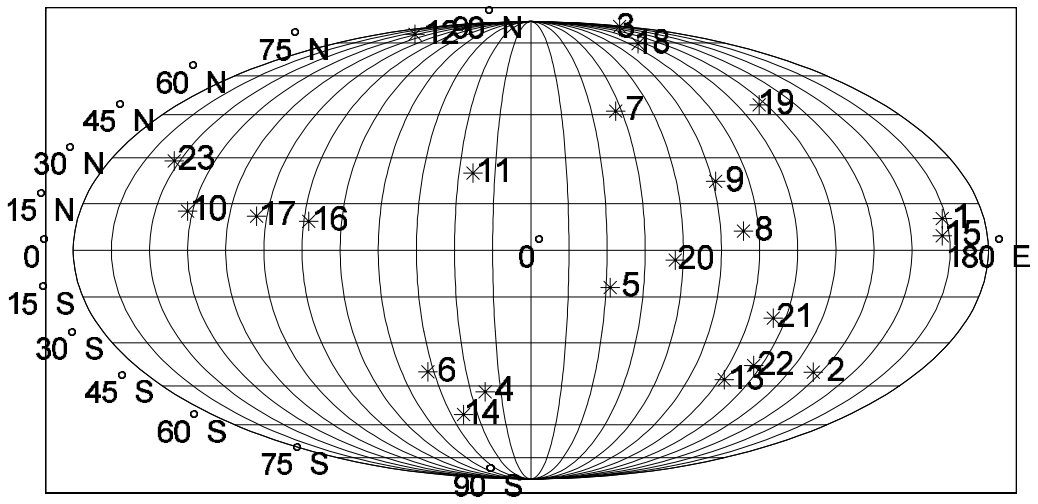
EHECRs positions at the distance 40 kpc from Earth, considered as protons
90° N
75° N
60° N
45° N
30° N
15° N
0°
15° S
30° S
45° S
60° S
75° S
90° S
180° E
12
3
18
7
19
23
11
9
10
17
16
1
15
8
0°
20
5
21
6
22
2
13
4
14

Figure A.7:

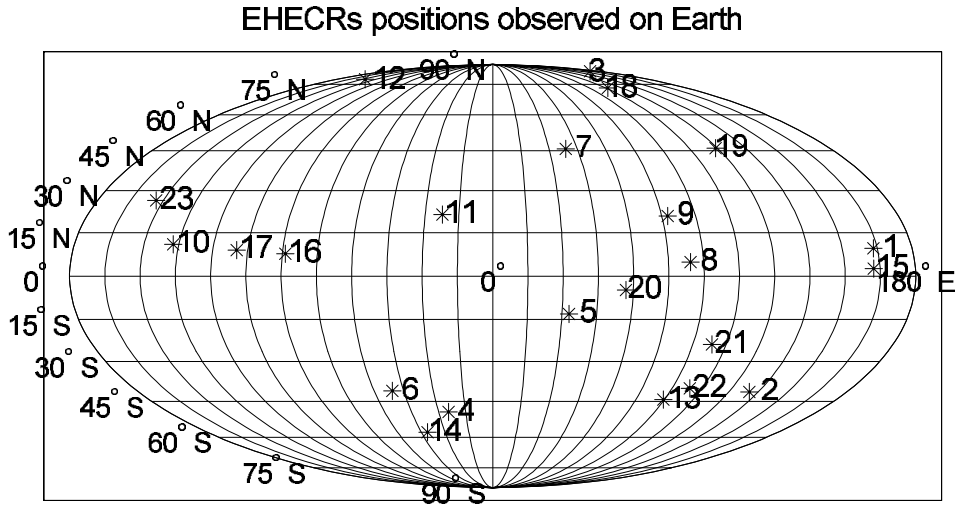
EHECRs positions observed on Earth
90° N
75° N
60° N
45° N
30° N
15° N
0°
15° S
30° S
45° S
60° S
75° S
90° S
0°
180° E
12
3
18
19
7
23
11
9
10
17
16
1
15
8
20
5
21
6
22
2
13
4
14

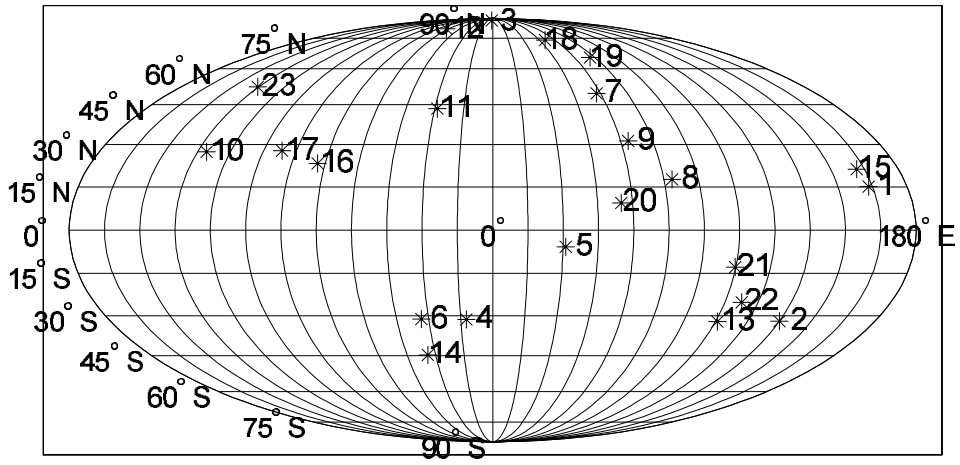
EHECRs positions at the distance 40 kpc from Earth, considered as oxygen nuclei
90° N
75° N
60° N
45° N
30° N
15° N
0°
15° S
30° S
45° S
60° S
75° S
90° S
0°
180° E
12
3
18
19
23
7
11
9
10
17
16
15
1
8
20
5
21
22
6
4
13
2
14

Figure A.8:

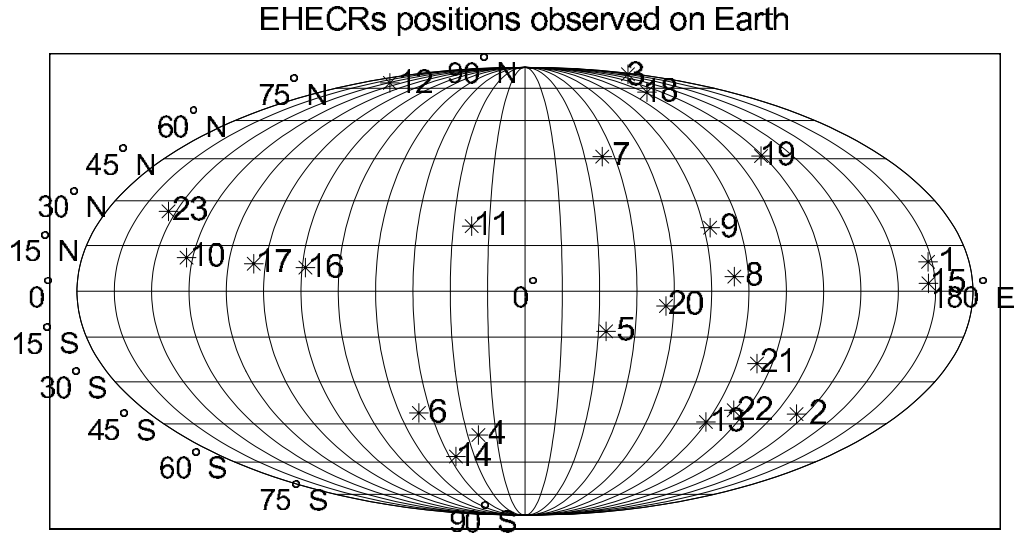
EHECRs positions observed on Earth
90° N
75° N
60° N
45° N
30° N
15° N
0°
15° S
30° S
45° S
60° S
75° S
90° S
180° E
12
3
18
7
19
23
11
9
10
17
16
1
15
8
0°
20
5
21
6
4
14
13
22
2

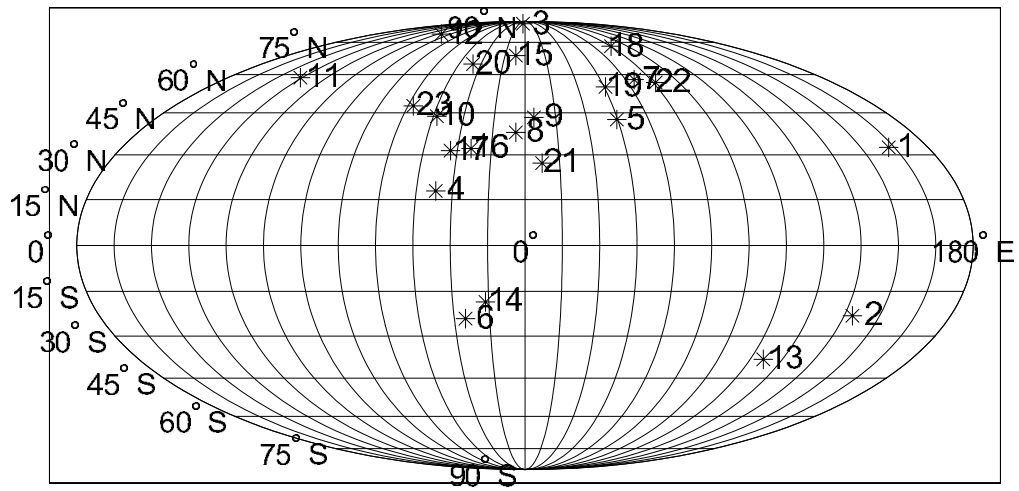
EHECRs positions at the distance 40 kpc from Earth, considered as Fe nuclei
90° N
75° N
60° N
45° N
30° N
15° N
0°
15° S
30° S
45° S
60° S
75° S
90° S
180° E
12
3
18
15
20
11
19
7
22
23
10
9
5
8
1
17
16
21
4
0°
14
6
2
13

Figure A.9:

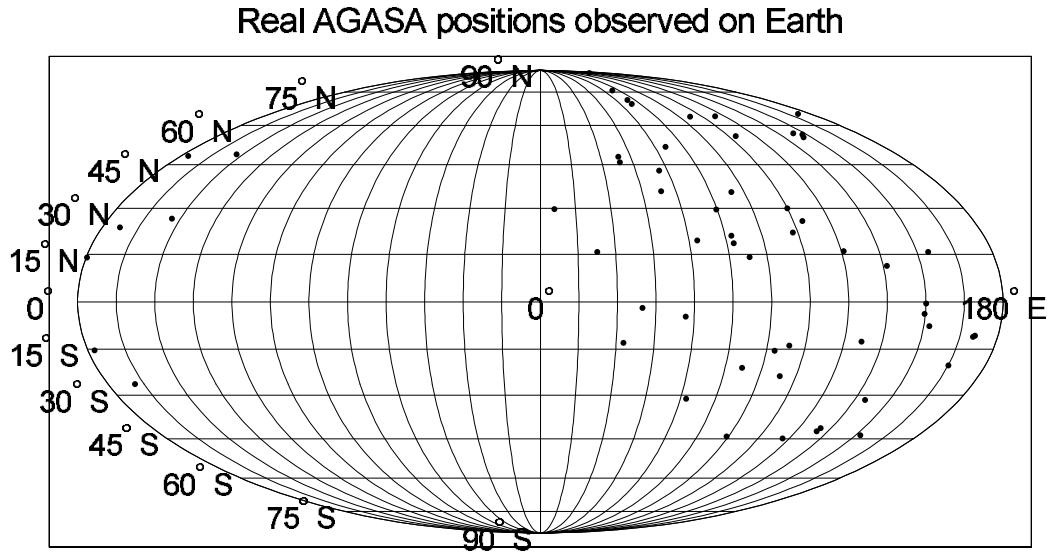
Real AGASA positions observed on Earth
90° N
75° N
60° N
45° N
30° N
15° N
0°
15° S
30° S
45° S
60° S
75° S
90° S
0°
180° E

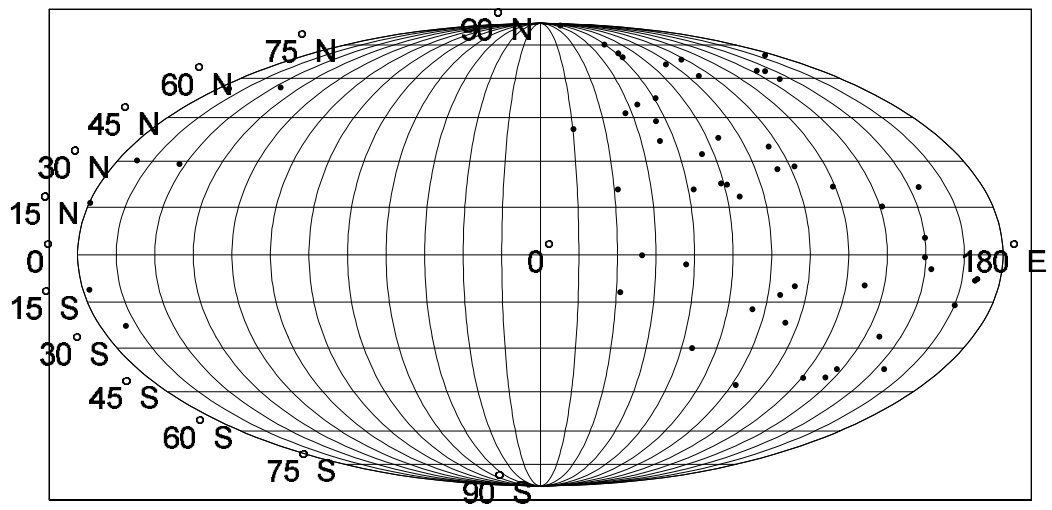
AGASA positions at the distance 40 kpc from Earth, considered as protons
90° N
75° N
60° N
45° N
30° N
15° N
0°
15° S
30° S
45° S
60° S
75° S
90° S
0°
180° E

Figure A.10:

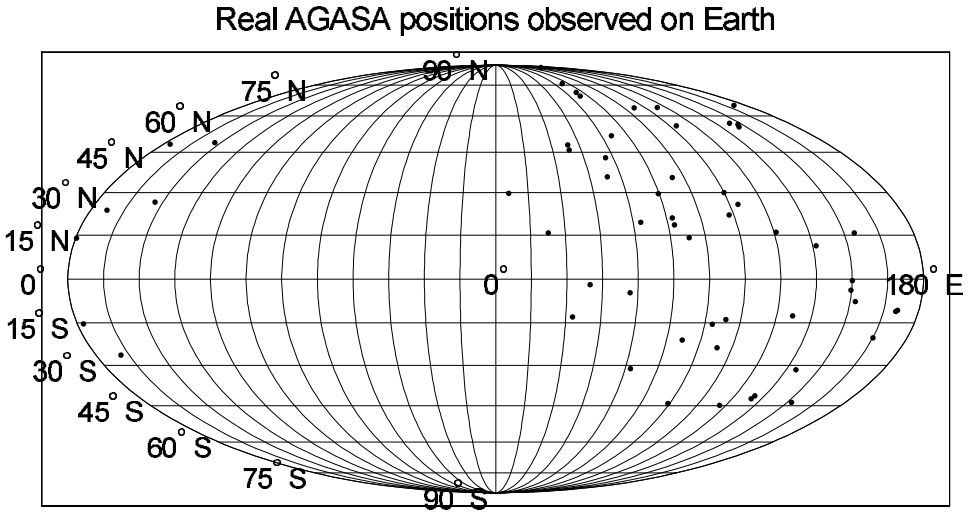
Real AGASA positions observed on Earth
90° N
75° N
60° N
45° N
30° N
15° N
0°
15° S
30° S
45° S
60° S
75° S
90° S
0°
180° E

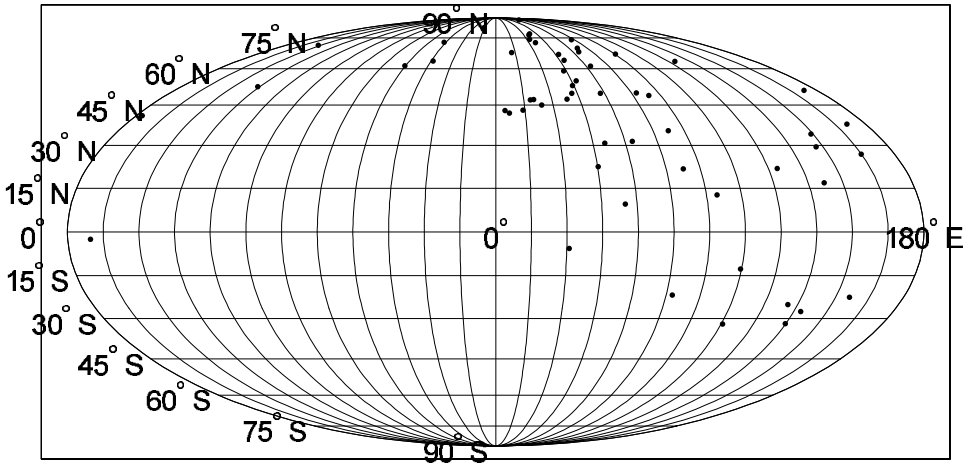
AGASA positions at the distance 40 kpc from Earth, considered as oxygen nuclei
90° N
75° N
60° N
45° N
30° N
15° N
0°
15° S
30° S
45° S
60° S
75° S
90° S
0°
180° E

Figure A.11:

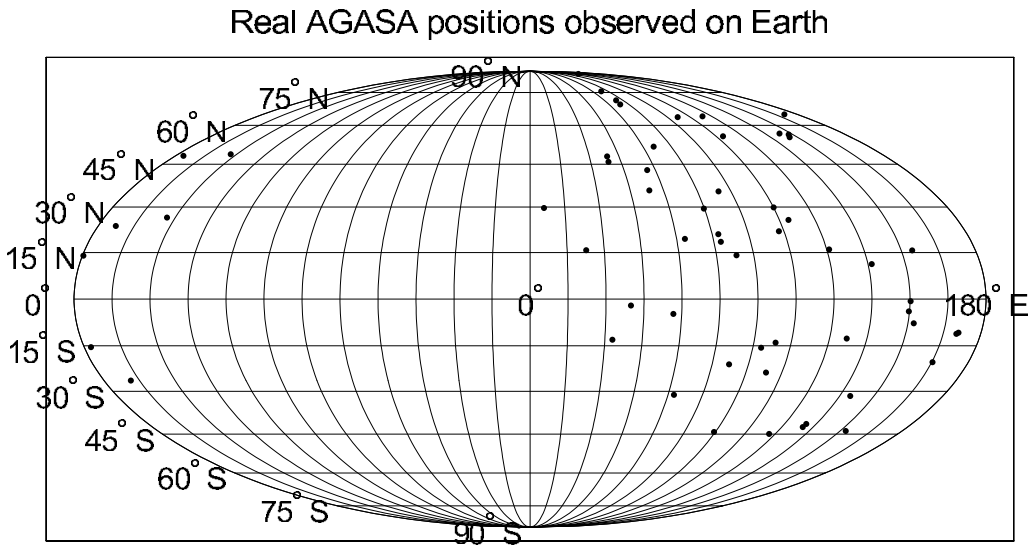
Real AGASA positions observed on Earth
90° N
75° N
60° N
45° N
30° N
15° N
0°
15° S
30° S
45° S
60° S
75° S
90° S
0°
180° E

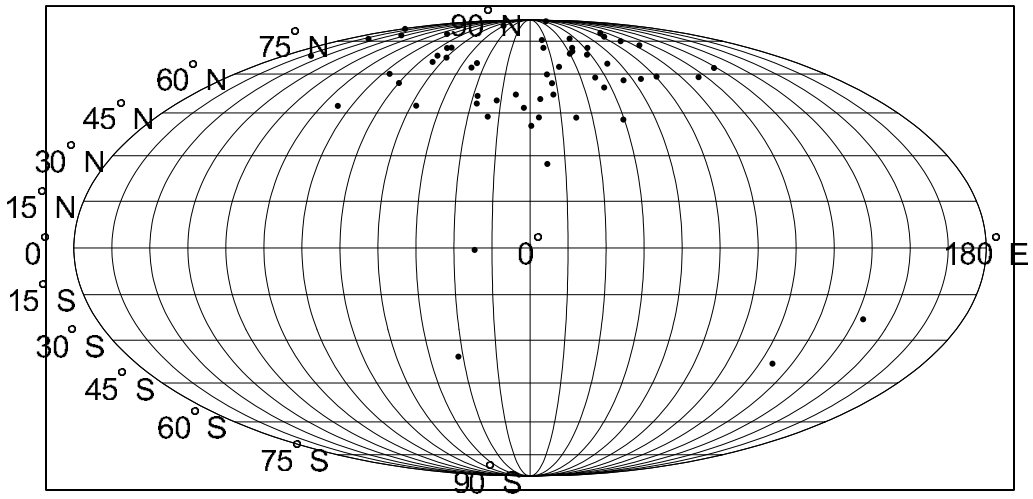
AGASA positions at the distance 40 kpc from Earth, considered as Fe nuclei
90° N
75° N
60° N
45° N
30° N
15° N
0°
15° S
30° S
45° S
60° S
75° S
90° S
0°
180° E

Figure A.12:

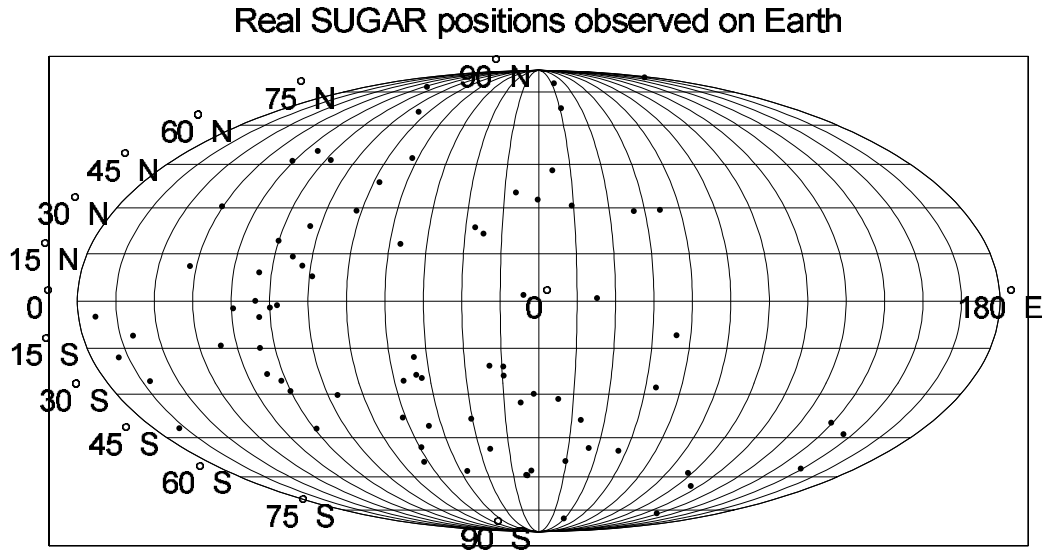
Real SUGAR positions observed on Earth
90° N
75° N
60° N
45° N
30° N
15° N
0°
15° S
30° S
45° S
60° S
75° S
90° S
0°
180° E

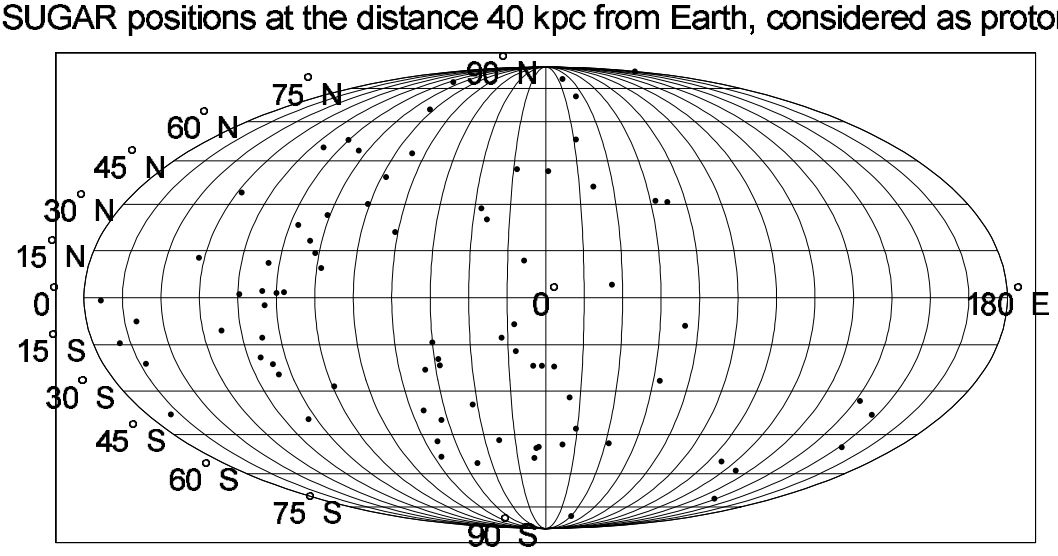
SUGAR positions at the distance 40 kpc from Earth, considered as protons
90° N
75° N
60° N
45° N
30° N
15° N
0°
15° S
30° S
45° S
60° S
75° S
90° S
0°
180° E

Figure A.13:

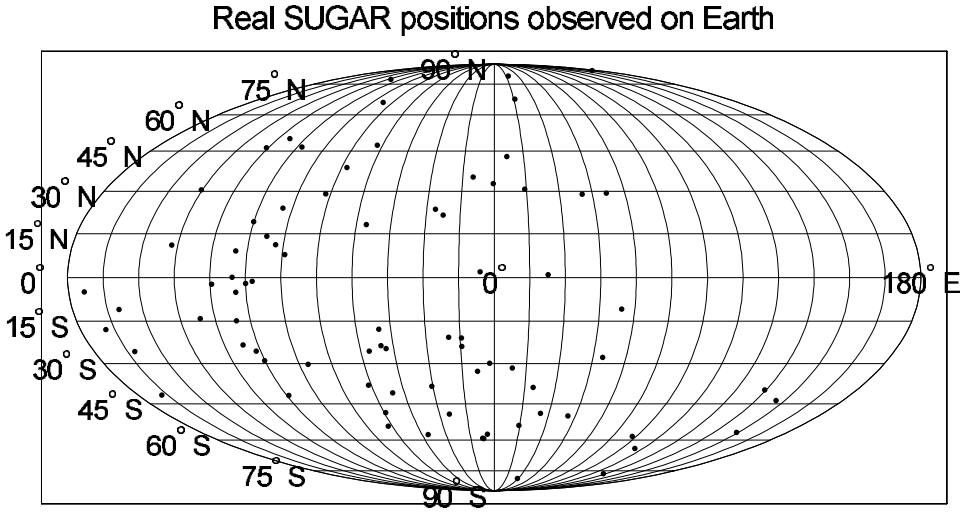
Real SUGAR positions observed on Earth
90° N
75° N
60° N
45° N
30° N
15° N
0°
15° S
30° S
45° S
60° S
75° S
90° S
0°
180° E

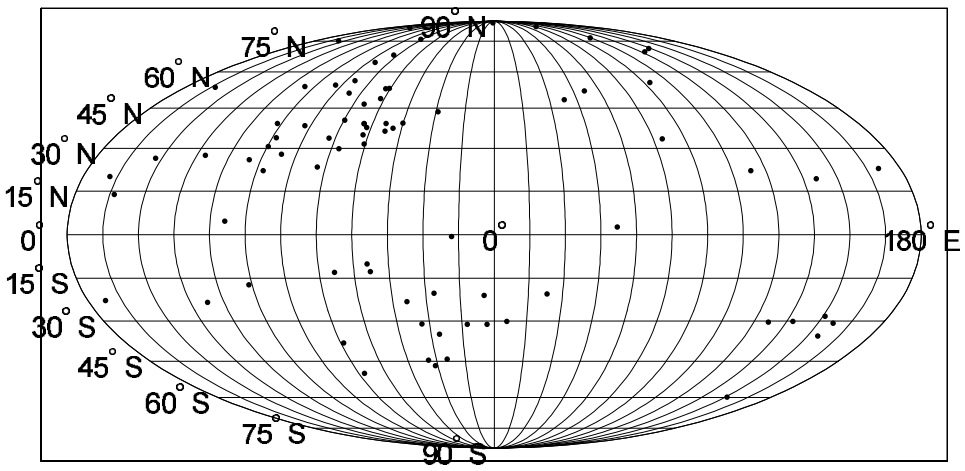
SUGAR positions at the distance 40 kpc from Earth, considered as oxygen nuclei
90° N
75° N
60° N
45° N
30° N
15° N
0°
15° S
30° S
45° S
60° S
75° S
90° S
0°
180° E

Figure A.14:

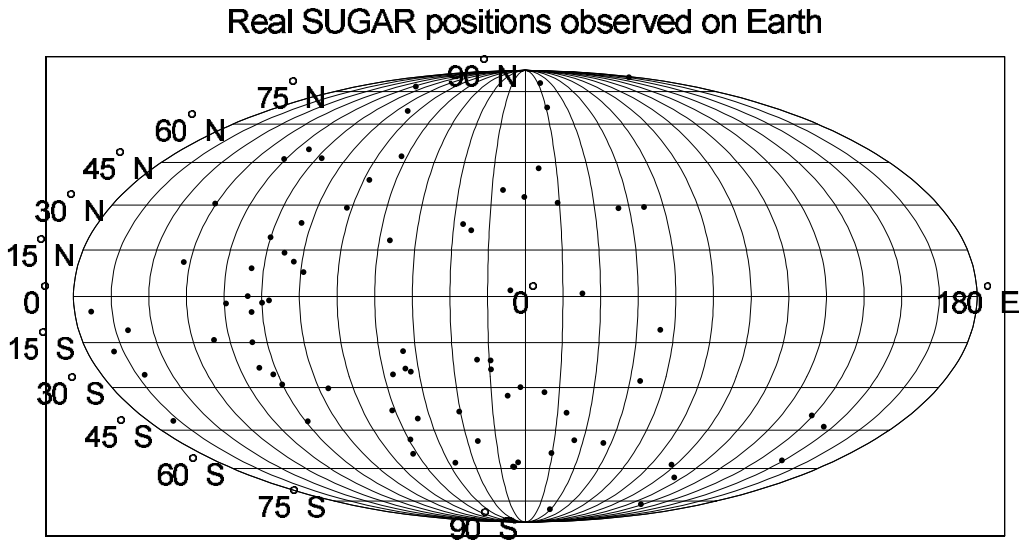
Real SUGAR positions observed on Earth
90° N
75° N
60° N
45° N
30° N
15° N
0°
15° S
30° S
45° S
60° S
75° S
90° S
0°
180° E

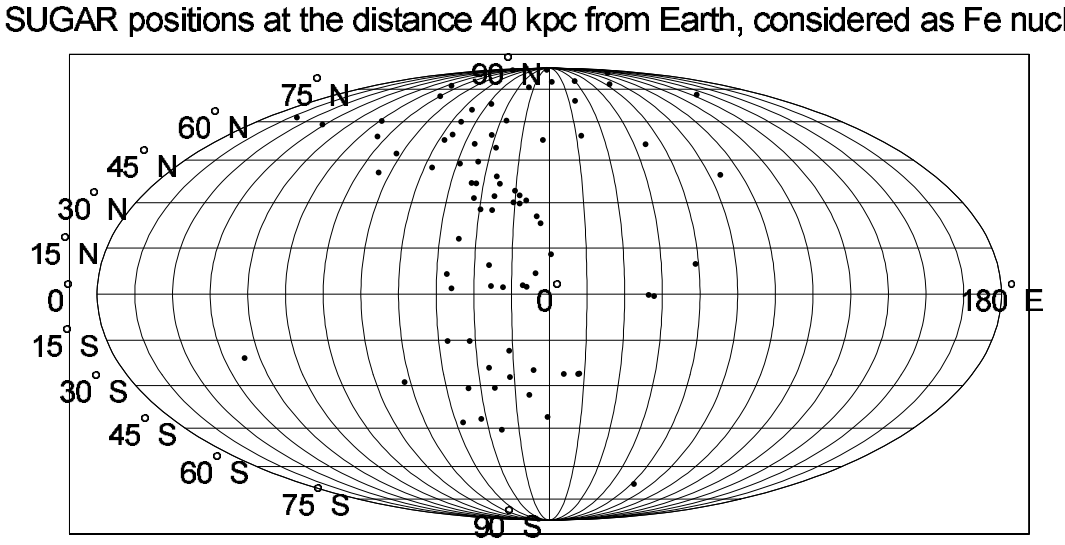
SUGAR positions at the distance 40 kpc from Earth, considered as Fe nuclei
90° N
75° N
60° N
45° N
30° N
15° N
0°
15° S
30° S
45° S
60° S
75° S
90° S
0°
180° E

Figure A.15:

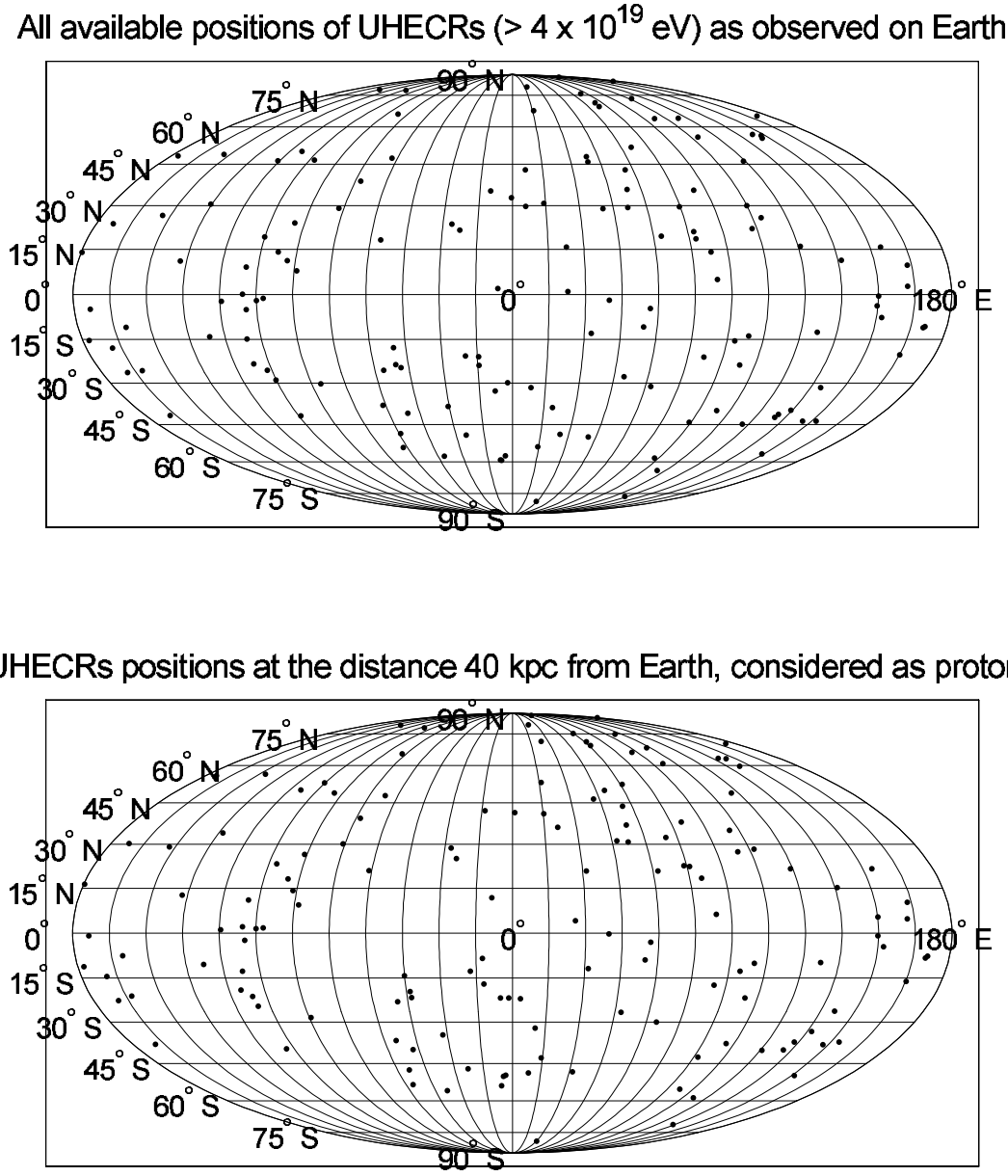
All available positions of UHECRs (> 4 x 10^19 eV) as observed on Earth
90° N
75° N
60° N
45° N
30° N
15° N
0°
15° S
30° S
45° S
60° S
75° S
90° S
0°
180° E
UHECRs positions at the distance 40 kpc from Earth, considered as protons
90° N
75° N
60° N
45° N
30° N
15° N
0°
15° S
30° S
45° S
60° S
75° S
90° S
0°
180° E

Figure A.16:

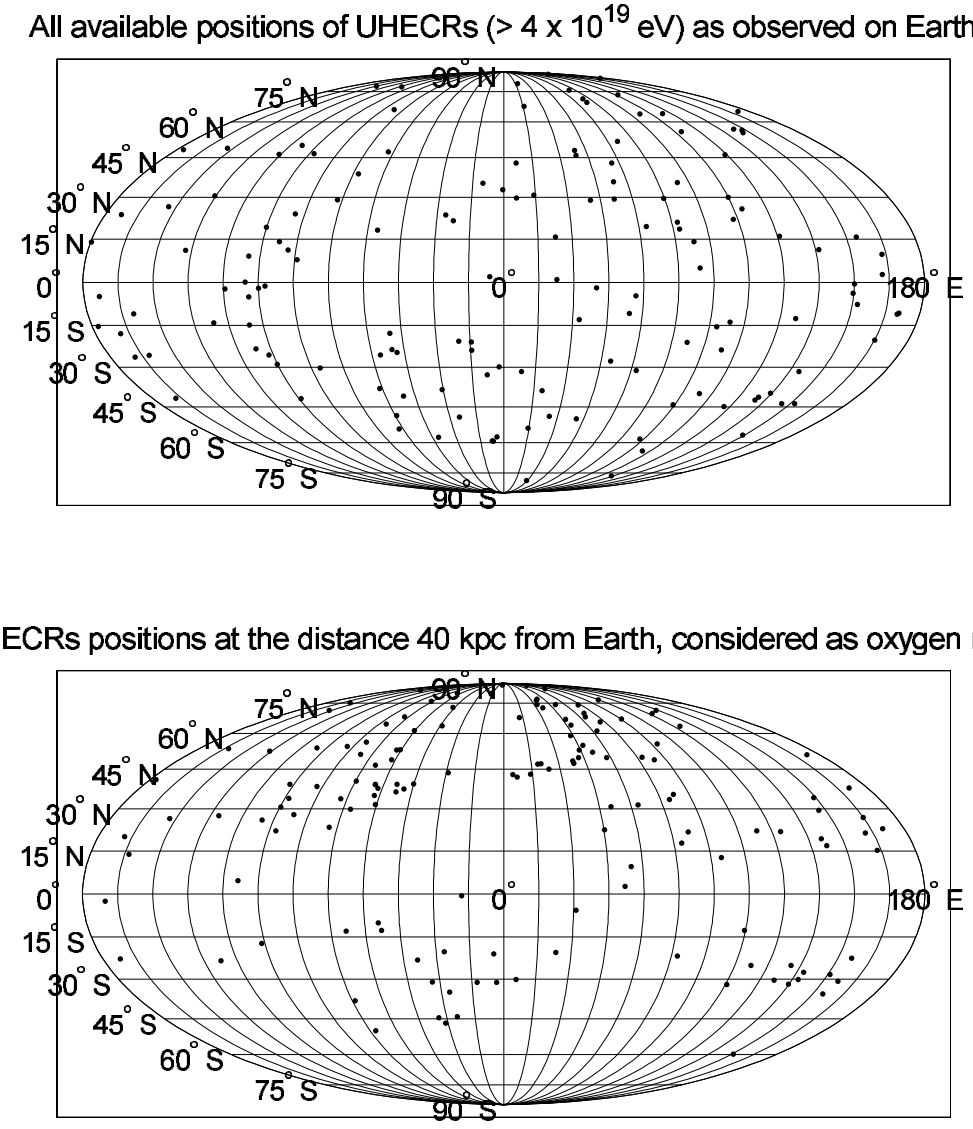
All available positions of UHECRs (> 4 x 10^19 eV) as observed on Earth
90° N
75° N
60° N
45° N
30° N
15° N
0°
15° S
30° S
45° S
60° S
75° S
90° S
0°
180° E
UHECRs positions at the distance 40 kpc from Earth, considered as oxygen nuclei
90° N
75° N
60° N
45° N
30° N
15° N
0°
15° S
30° S
45° S
60° S
75° S
90° S
0°
180° E

Figure A.17:

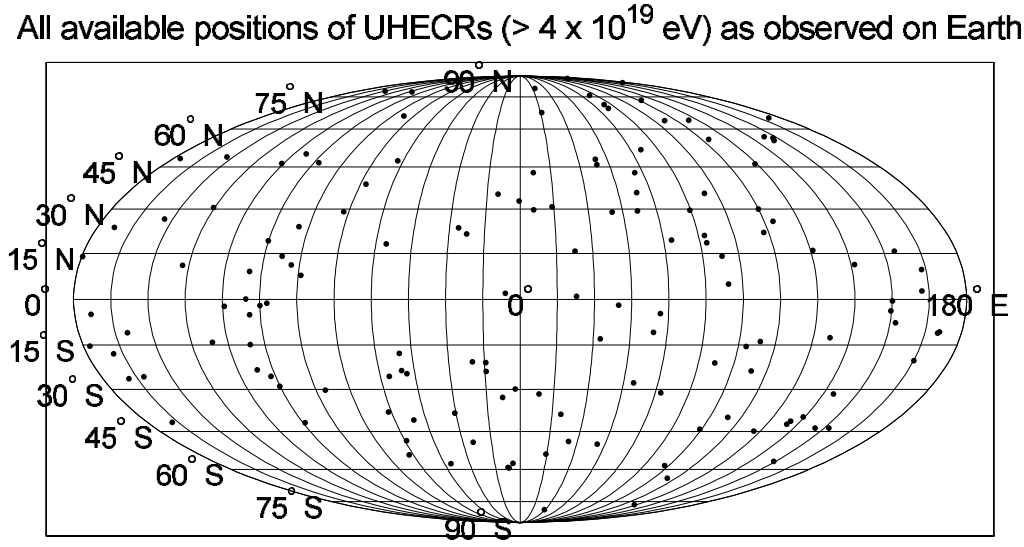
All available positions of UHECRs (> 4 x 10^19 eV) as observed on Earth
90° N
75° N
60° N
45° N
30° N
15° N
0°
15° S
30° S
45° S
60° S
75° S
90° S
0°
180° E

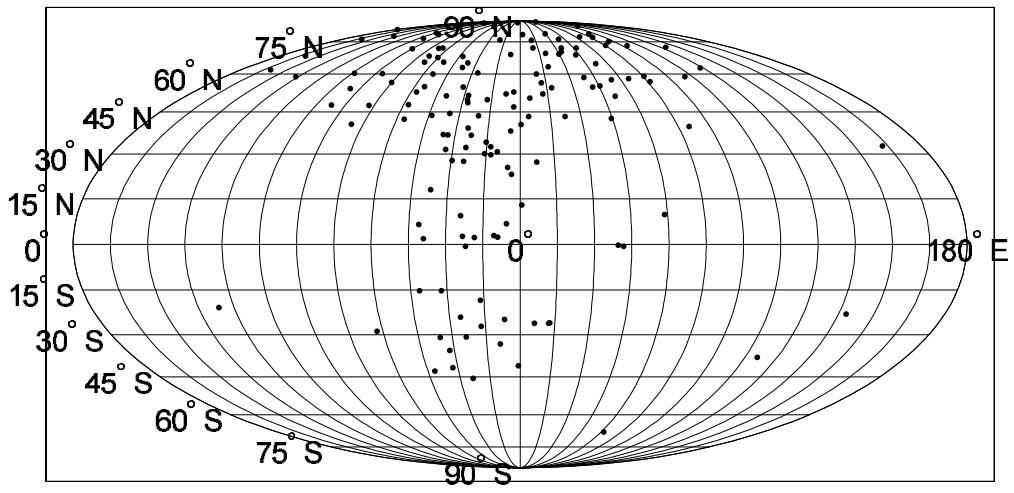
UHECRs positions at the distance 40 kpc from Earth, considered as Fe nuclei
90° N
75° N
60° N
45° N
30° N
15° N
0°
15° S
30° S
45° S
60° S
75° S
90° S
0°
180° E

Figure A.18:

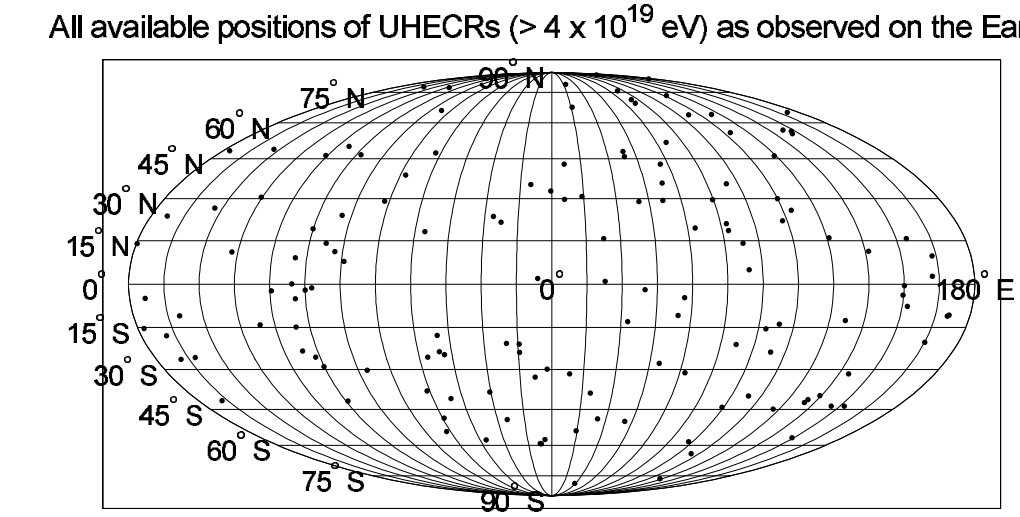
All available positions of UHECRs (> 4 x 10^19 eV) as observed on the Earth
90° N
75° N
60° N
45° N
30° N
15° N
0°
15° S
30° S
45° S
60° S
75° S
90° S
0°
180° E

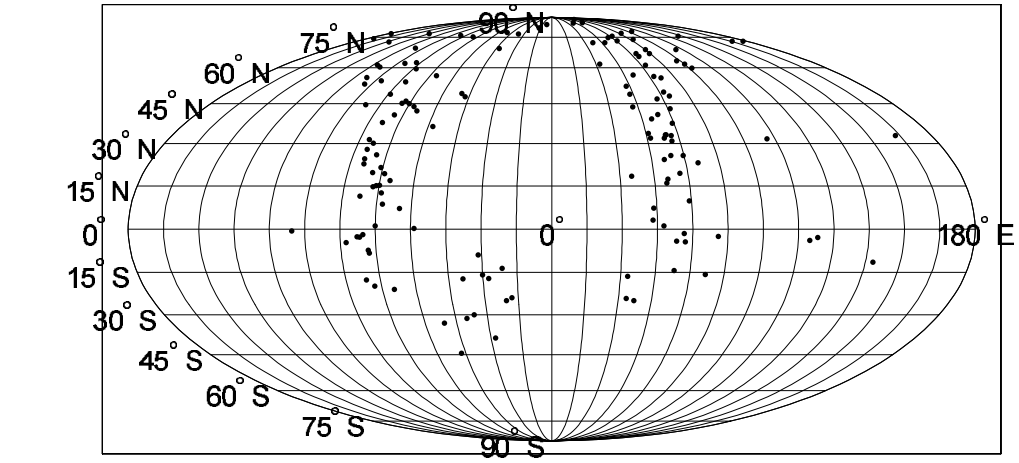
UHECRs positions at the distance 8.5 kpc from the Earth, considered as Fe nuclei
90° N
75° N
60° N
45° N
30° N
15° N
0°
15° S
30° S
45° S
60° S
75° S
90° S
0°
180° E

Figure A.19:

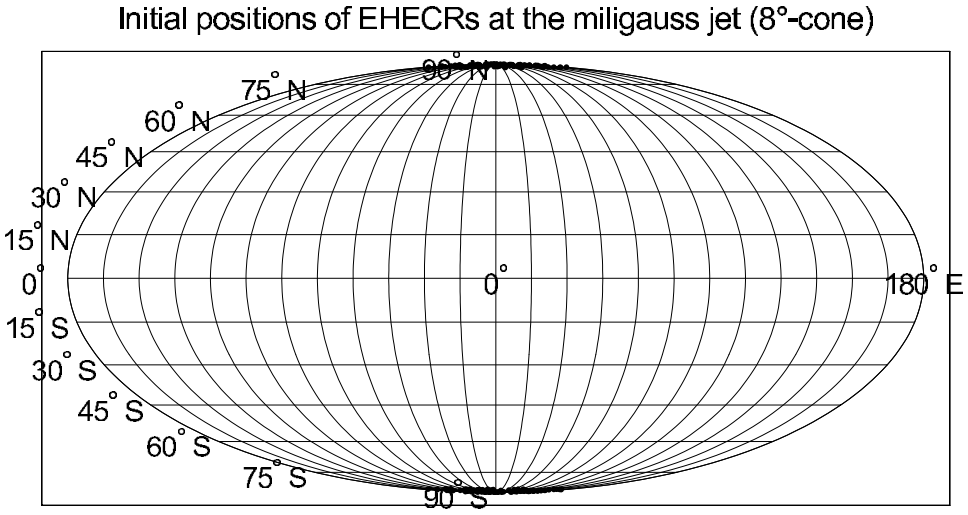
Initial positions of EHECRs at the miligauss jet (8°-cone)
90° N
75° N
60° N
45° N
30° N
15° N
0°
15° S
30° S
45° S
60° S
75° S
90° S
0°
180° E

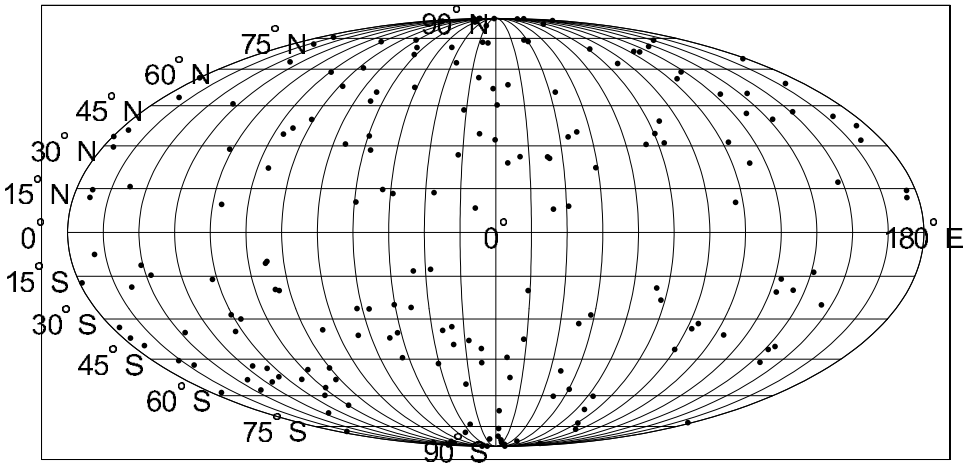
EHECRs positions at the distance 4 kpc from the source, considered as Fe nuclei
90° N
75° N
60° N
45° N
30° N
15° N
0°
15° S
30° S
45° S
60° S
75° S
90° S
0°
180° E

Figure A.20:

Bibliography

[1] Abu-Zayyad T. et al., 2000, Phys. Rev. Lett. 84, 4276

[2] Afanasiev B.N. et al., 1993, in Nagano M. (ed.) Proceedings of the Tokyo Workshop on Techniques for the Study of the Extremely High Energy Cosmic Rays, 35

[3] Aharonian F.A., Cronin J.W., 1994, Phys. Rev. D 50, 1892

[4] Ahn E.-J., Medina-Tanco G., Biermann P., Stanev T., 1999, Preprint astro-ph/9911123

[5] Auger P., Maze R., 1938, C. R. Acad. Sci. Ser. B 207, 228

[6] Auger P., 1945, What are Cosmic Rays?, University of Chicago Press

[7] The Auger Collaboration, 1997, The Pierre Auger Observatory Design Report, Fermilab

[8] The Auger Project Official Website, 2001, http://www.auger.org/admin

[9] Axford W.I. et al., 1977, in Proceedings of the 15th International Cosmic Ray Conference, Plovdiv, Vol. 11, 132

[10] Baltrusaitis R. M., Cady R. et al., 1985, Nucl. Instrum. Methods Phys. Res. A 240, 410

[11] Bassi P., Clark G., Rossi B., 1953, Phys. Rev. 92, 441

[12] Beck R., Brandenburg A., Moss D., Shukurov A., Sokoloff D., 1995, NORDITA preprint 95/67 A

[13] Beck R., 2000, Preprint astro-ph/0012402

[14] Berezinsky V.S., Grigoreva S.I., 1988, A&A 199, 1

[15] Berezinsky V.S., Preprint hep-ph/9802351

[16] Bertou X., Boratav M., Selvon-Letessier A., 2000, Preprint astro-ph/0001516

[17] Bhattacharjee P., Sigl G., 2000, Phys. Rep. 327, 110

[18] Billoir P., Letessier-Selvon A., 2000, Preprint astro-ph/0001427

[19] Bird D.J. et al., 1994, ApJ 424, 491

[20] Bird D.J. et al., 1995, ApJ 441, 144

[21] Blasi P., Epstein R.I., Olinto A.V., 2000, ApJ 533, L123

[22] Blumenthal G.R., 1970, Phys. Rev. D 1, 1596

[23] Boháčová M., 1999, Diploma Thesis, Charles University Prague

[24] Boldt E., Ghosh P., 1999, Mon. Not. R. Astron. Soc. 307, 491

[25] Capdevielle J.N. et al., 1992, Kernforschungzentrum Karlsruhe preprint KfK 4998

[26] Catalogue of Highest Energy Cosmic Rays, 1980, World Data Center for Cosmic Rays, Institute of Physical and Chemical Research, Itabashi, Tokyo, Japan

[27] Coleman S., Glashow S.L., 1999, Phys. Rev. D 59, 116008

[28] Compton A.H., 1933, Phys. Rev. 43, 387

[29] Cowsik R., Rajalakshmi G., Sreekantan B.V., 1999, in: Nagano M. (ed.) Proceedings of the 26th International Cosmic Ray Conference, Salt Lake City, HE 5.3.09

[30] Cronin J.W., 1992, Nucl. Phys. B. (Proc. Suppl.) 28B, 213

[31] Cronin J.W., 1999, Rev. Mod. Phys. 71, S165

[32] Dar A., 2000, Preprint astro-ph/0006013

[33] De Marzo C.N., 1998, in: Krizmanic J.F., Ormes J.F., Streitmatter R.E. (eds.) Proceesdings of Workshop on Observing Giant Cosmic Ray Air Showers from $> 10^{20}$ eV Particles from Space, AIP Conf. Proc. No. 433, 87

[34] Elbert J.W., Sommers P., 1995, ApJ 441, 151

[35] Ellis J., 2000, Preprint astro-ph/0010474

[36] Elstner D., Meinel R., Beck R., 1992, A&A Suppl. Ser. 94, 587

[37] Enge H. A., 1966, Introduction to nuclear physics, Addison-Wesley Publishing Co.

[38] Farrar G.R., 1996, Phys. Rev. Lett. 76, 4111

[39] Farrar G.R., Piran T., 1999, Preprint New York University 99-XX

[40] Fermi E., 1949, Phys. Rev. 75, 1169

[41] Gaisser T.K., 2000, Preprint astro-ph/0011525

[42] Greisen K., 1956, in: Wilson J.G. (ed.) Progress in Cosmic Ray Physics III, 3

[43] Greisen K., 1966, Phys. Rev. Lett. 16, 748

[44] Han J.L., Qiao G.J., 1994, A&A, 288, 759

[45] Han J.L., Manchester R.N., Qiao G.J., 1999, Mon. Not. R. Astron. Soc. 306, 371

[46] Hara T., Kawaguchi S., Mikamo S., Nagano M., Suga K., Tanahashi G., Uchino K., Akiyama H., 1970, Acta Phys. Acad. Sci. Hung. 29, Suppl. 3, 361

[47] Harari D., Mollerach S., Roulet E., 2000, Preprint astro-ph/0010068 v2

[48] Hayashida N. et al., 2000, Preprint astro-ph/0008102

[49] Hess V., 1912, Physik. Zeitschr. 13, 1084

[50] Hill C.T., Schramm D.N., 1985, Phys. Rev. D 31, 564

[51] Hillas A.M., 1968, Can. J. Phys. 46, S623

[52] Hillas A.M., 1970, Acta Phys. Acad. Sci. Hung. 29, Suppl. 3, 355

[53] Hillas A.M. et al., 1971, in Proceedings of the 12th International Cosmic Ray Conference, Hobart, Vol. 3, 1001

[54] Hillas A.M., 1985, in: Proceedings of the 19th International Cosmic Ray Conference, La Jolla, Vol. 1, 155

[55] Hiltner W.A., 1949, ApJ 109, 471

[56] Karakula S., Osborne J.L., Roberts E., Tkaczyk W., 1972, J. Phys. A 5, 904

[57] Kewley L.J., Clay R.W., Dawson B.R., 1996, Astropart. Phys. 5, 69

[58] Klages H.O. et al., 1997, Nucl. Phys. B (Proc. Suppl.) 52 B, 92

[59] Kronberg P.P., 1994, Rep. Prog. Phys. 57, 325

[60] Lawrence M.A., Reid R.J.O., Watson A.A., 1991, J. Phys. G 17, 733

[61] Lee A.A., Clay R.W., 1995, J. Phys G 21, 1743

[62] Lemaître G., Vallarta M.S., 1933, Phys. Rev. 43, 87

[63] Lemoine M., Sigl G., Olinto A.V., Schramm D., 1997, Preprint astro-ph/9704023

[64] Linsley J., 1963, Phys. Rev. Lett. 10, 146

[65] Linsley J., 1979, in Filed Committee Report, "Call for Projects and Ideas in High Energy Astrophysics for the 1980s", National Science Foundation, unpublished

[66] Linsley J., 1986, J. Phys. G 12, 51

[67] Linsley J., Scarsi L., 1962, Phys. Rev. 128, 2384

[68] Linsley J., Scarsi L., Rossi B., 1961, Phys. Rev. Lett. 6, 458

[69] Longair M.S., 1992, High Energy Astrophysics, Cambridge University Press

[70] Medina-Tanco G., 1998, ApJ Lett. 495, L79

[71] Medina-Tanco G., Gouveia Dal Pino E., Horvath J., 1998, ApJ 492, 200

[72] Millikan R.A., Cameron G.H., 1928, Phys. Rev. 32, 53

[73] Murthy P.V.R., Wolfendale A.V., 1993, Gamma-ray astronomy, Cambridge University Press

[74] Nagano M. et al., 1992, J. Phys. G 18, 423

[75] Nagano M., Watson A.A., 2000, Rev. Mod. Phys. 72, 689

[76] Nagano M. et al., 2000, Astropart. Phys. 13, 277

[77] Olinto A.V., 2000, Preprint astro-ph/0011106

[78] Penzias A.A., Wilson R.W., 1965, ApJ 205, 638

[79] Porter N.A., 1960, Nuovo Cimento 16, 958

[80] Pravdin M.I. et al., 1999, in: Nagano M. (ed.) Proceedings of the 26th International Cosmic Ray Conference, Salt Lake City, OG 1.3.14

[81] Protheroe J.R., 1998, Preprint of the University of Adelaide, Australia, ADP-AT-98-9

[82] Puget J.-L., Stecker F.W., Bredekamp J.H., 1976, ApJ 205, 638

[83] Rand R.J., Kulkarni S.R., 1989, ApJ 343, 760

[84] Ryu D., Kang. H., Biermann P.L., 1998, Preprint astro-ph/9803275

[85] Sakaki N. et al., 1997, in: Proceedings of the 25th International Cosmic Ray Conference, Durban, Vol. 5, 217

[86] Sciutto S.J., 1999, Preprint astro-ph/9905185

[87] Sommers P., Elbert J.W., 1995, ApJ 441, 151

[88] Stanev T., Biermann P., Lloyd-Evans J., Rachen J., Watson A.A., 1995, Phys. Rev. Lett. 75, 3056

[89] Stanev T., 1997, ApJ 479, 290

[90] Stecker F.W., Salamon M.H., 1999, ApJ 512, 521

[91] Stecker F.W., 2001, Preprint astro-ph/0101072 v2

[92] Streitmatter R.E., 1998, in: Krizmanic J.F., Ormes J.F., Streitmatter R.E. (eds.) Proceedings of Workshop on Observing Giant Cosmic Ray Air Showers from $> 10^{20}$ eV Particles from Space, AIP Conf. Proc. No. 433, 95

[93] Suga K., Chudakov A.E., 1962, in: Escobar I. (ed.) Proceedings of 5th Interamerican Seminar on Cosmic Rays, Laboratorio de Fisica Cosmic del Universidad Mayor de San Andres, La Paz, Bolivia, Vol. 2, p. XLIX

[94] Takahara F., 1996, in: Nagano M. (ed.) Proceedings of the International Symposium on Extremely High Energy Cosmic Rays: Astrophysics and Future Observations, Institute of Cosmic Ray Research, University of Tokyo, Tokyo, Japan, 61

[95] Takeda M et al., 1998, Phys. Rev. Lett. 81, 1163

[96] Takeda M. et al., 1999, ApJ 522, 225

[97] Takeda M. et al., 1999, in: Nagano M. (ed.) Proceedings of the 26th International Cosmic Ray Conference, Salt Lake City, Vol. 3, p. 252

[98] Telescope Array Design Report, 1998, Institute of Cosmic Ray Research, Univeristy of Tokyo, Tokyo, Japan

[99] Uchihori Y. et al., 1996, in: Nagano M. (ed.) Proceedings of the International Symposium on Extremely High Energy Cosmic Rays: Astrophysics and Future Observations, Institute of Cosmic Ray Research, University of Tokyo, Tokyo, Japan, 50

[100] Uchihori Y., Nagano M., Takeda M., Teshima M., Lloyd-Evans J., Watson A.A., 2000, Astropart. Phys. 13, 151

[101] Watson A.A., 1992, Nucl. Phys. B (Proc. Suppl.) 28, 3

[102] Waxman E., 1995, Phys. Rev. Lett. 75, 386

[103] Weiler T.J., 1999, Vanderbilt University Preprint VAND-TH-9-99

[104] Winn M.M., Ulrichs J., Peak L.S., McCusker C.B.A., Horton L., 1986, J. Phys. G 12, 653

[105] Wolfendale A.W., Wibig T., 1999, in: Nagano M. (ed.) Proceedings of the 26th International Cosmic Ray Conference, Salt Lake City, OG 1.3.01

[106] Yoshida S., Teshima M., 1993, Prog. Theor. Phys. 89, 833

[107] Yoshida S., Dai H., 1998, J. Phys. G 24, 905

[108] Zatsepin G.T., Kuzmin V.A., 1966, Zh. Eksp. Theor. Fiz. (Pisma Red.) 4, 114